

**Università degli Studi di Napoli “Federico II”**



**Dottorato in Tecnologie Innovative  
per Materiali, Sensori e Imaging**

**- 20° ciclo -**

**Advances in HTS mesoscopic junctions**

**Daniela Stornaiuolo**

Coordinatore:  
*Prof. Giancarlo Abbate*

anno accademico 2006 - 2007

## Contents

Introduction.....	1
Scope and outline of the thesis .....	2
1. General theory of HTS and Josephson junctions .....	4
1.1. High temperature superconductivity .....	4
1.1.1. YBCO crystalline structure .....	4
1.1.2. Doping mechanism.....	4
1.2. BCS theory .....	6
1.2.1. Symmetry of the wave function in high temperature superconductors.....	7
1.3. Theory of Josephson junctions .....	8
1.3.1. Derivation of the Josephson equations .....	8
1.3.2. Josephson junctions in a magnetic field .....	11
1.3.3. The RCSJ and tilt washboard models .....	12
2. Grain boundary Josephson junctions.....	16
2.1. Classification of grain boundary junctions.....	16
2.2. Grain boundary mechanisms.....	20
2.3. Effects of the d-wave symmetry of the order parameter in HTS junctions.....	22
2.3.1. Effects on the critical current density.....	22
2.3.2. Effects on the gap .....	24
2.3.3. d-wave induced $\pi$ -shifts .....	25
2.3.4. Effects of the 2 <sup>nd</sup> harmonic in the current-phase relation.....	31
2.4. Grain boundary junctions in superconducting electronic applications .....	34
3. Biepitaxial junctions experimental techniques: thin films deposition and characterization .....	37
3.1. Biepitaxial junctions' structure and fabrication procedure .....	37
3.2. Techniques for the structural characterization of thin films .....	40
3.2.1. X-Ray diffraction .....	41
3.2.2. Atomic force microscopy .....	43
3.2.3. Scanning electron microscopy .....	44
3.3. Hints on the theory of films growth .....	45
3.3.1. Nucleation and growth .....	46
3.3.2. Expitaxial thin films and structural defects.....	48
3.3.3. Epitaxial relations in our junctions' structure .....	50
3.4. Thin films realization .....	52
3.4.1. Evaporation .....	52
3.4.2. Magnetron sputtering .....	53
3.4.3. CeO <sub>2</sub> films deposited via RF magnetron sputtering.....	54
3.4.4. YBCO films deposited via inverted cylindrical magnetron sputtering ....	58
3.4.5. Pulsed laser deposition .....	61
4. Biepitaxial junctions experimental techniques: patterning .....	65
4.1. Mask making techniques: photolithography .....	65
4.2. Mask making techniques: electron beam lithography.....	68
4.2.1. Carbon deposition .....	69
4.2.2. Electron beam resist .....	70
4.2.3. Electron beam exposure .....	70
4.2.4. Mask transfer to the carbon layer .....	75
4.3. Ion milling .....	75
4.4. Results .....	77
4.4.1. Micrometric junctions .....	77

4.4.2.	Sub micrometric junctions .....	77
5.	Measurement system and techniques .....	79
5.1.	<sup>3</sup> He refrigerators description and operation .....	79
5.2.	Upgrading of the Heliox <sup>3</sup> He system.....	80
5.2.1.	Cold filters.....	83
5.3.	Measurement environment and strategy .....	85
6.	Biepitaxial junctions' transport properties .....	88
6.1.	Transport properties of LAO based junctions .....	88
6.2.	Transport properties of STO based junctions.....	90
6.2.1.	Improvements of junctions quality and stability .....	94
6.2.2.	GB transport mechanisms .....	94
6.3.	STO based sub-micrometric junctions .....	101
6.4.	Spectroscopy of tunnel-like junctions .....	106
6.4.1.	Overview of gap spectroscopy .....	108
6.4.2.	Gap spectroscopy using biepitaxial tunnel-like junctions.....	110
7.	Conclusions .....	113
8.	References .....	114

## Introduction

Many scientists recall the March 1987 meeting of the American Physical Society as the “Woodstock of Physics”. The nickname is due to the fervour of the meeting, featuring 50 speakers delivering their results until 3 a.m. to an excited crowd composed of fellow scientists and many journalists. The reason for such clamour was the discovery, one year before, of materials showing superconductivity to temperatures higher than the liquid nitrogen one. It was seen as an enormous step forward to the electronic application of superconductivity, making it possible to rely on relatively cheap liquid nitrogen cooling systems instead than on the expensive liquid helium ones. Moreover, in the excitement of those months, many scientists started to dream about room temperature superconductivity. Twenty years on, room temperature superconductivity is still a dream and many scientists point out that the promises of high temperature superconductors (HTS) electronic applications have largely not materialized. Probably, the expectations put on HTS were simply too high; soon scientists started to realize that the physics of HTS materials is in many aspects different from the one of conventional superconductors, sometimes more complex and multifaceted. Moreover, HTS are more difficult to grow in controllable structures and manipulate to fabricated electronic devices. They are sensitive to environmental conditions, and have to be suitably protected during the devices fabrication procedures and during the storage time in order not to damage their transport properties. However, during the years, the difficulties in handling HTS materials have been outgrown by the discoveries of unique effects taking place in them, effects that don’t have any counterpart in conventional superconductivity. Examples are second harmonic effects in the current-phase relation and spontaneous generation of flux in HTS based  $\pi$ -junctions. Today the interest in HTS devices is rising again. Important steps are being made in the direction of a better understanding of HTS physics and of the advantages these materials could bring when suitably implemented for electronic applications. In parallel with advances in the understanding of their physics, the technologies used for HTS devices have been refined, with the aim of obtaining stable and predictable properties. These two aspects are, indeed, closely interlinked. On one hand, a better understanding of the physics ruling HTS materials can guide the realization of efficient devices, helping to understand which aspects of the transport properties should be favoured with a suitable devices’ design. On the other, high quality devices help in the clarification of transport properties of HTS, emphasizing intrinsic effects despite extrinsic, spurious ones.

One of the most defining properties of HTSs is the four fold, *d*-wave symmetry of their order parameter. This feature, now well established thanks to many experiments, has no correspondence in conventional superconductivity. It can be exploited in a number of ways, giving the possibility to create devices with novel properties and functionalities. For example, the *d*-wave order parameter undergoes a phase shift of  $\pi$  passing from one lobe to the other (i.e. each  $90^\circ$ ). By realizing devices in which two successive lobes are coupled, as for examples a ring interrupted by two junctions with the suitable geometry, one can obtain a so called “frustrated geometry”, resulting in the spontaneous generation of half a flux quantum. This quiet, noiseless source of magnetic flux could found application in a number of fields, could for example provide a quiet bias for the operation of a qubit (from which the name “quiet qubit”), substituting the external bias, possible source of noise; or simplify and improve the design and properties of other superconducting devices.

The realization of such proposals has for long time been hindered by the complex structure of HTS and low quality of HTS devices, when compared with conventional superconductors based ones. Nevertheless, recently, the possibility to actually measure macroscopic quantum effects in HTS devices has been assessed with the measurement of

macroscopic quantum tunnelling (MQT) and energy level quantization in an HTS Josephson junctions.

The possibility to realize the applications of HTS devices we mentioned, and also many others, is based on:

- the understanding of HTS materials physics
- the understanding of how this physics comes into play when complex devices are realized
- the possibility to rely on stable devices with predictable properties

The physics behind HTS junctions operation has still, indeed, many obscure points; mainly due to the problems in obtaining clean structures, where extrinsic, in particular microstructural aspects, do not mask the fundamental ones. A possible way to clarify this issue is, therefore, to improve the fabrication technique and, also, to use a design that is less sensitive to disorder. During the last few years, the developments in nanoscale technology and fabrication procedures have made it possible their application also to HTS materials. The advantages in using such technologies in this field are many and of great relevance. The reduction in size of HTS junctions brings to the realization of cleaner structures, where impurities could have less influence on the transport behaviour. Some studies have also pointed out that reducing the size of HTS devices could bring the reduction of detrimental effects for quantum applications, such as decoherence. On a broader scale, the reduced dimensions could make new transport regimes accessible and also bring to light novel effects. From a more technological point of view, the application of nanofabrication methods to HTS materials will help in defining protocols for the manipulation of sensitive materials, as HTS are, thus representing a valuable source for developing knowledge in the nanotechnology industry. Today, the studies on sub-micrometric HTS junctions are growing, but no statistic is yet available to experimentally prove and confirm the advantages of the use of nanotechnology in this field.

## ***Scope and outline of the thesis***

The main aims of this work are a better understanding of HTS Josephson junctions behaviour through better quality devices and especially through the first generation of biepitaxial “nano-structures”. Biepitaxial junctions were invented in 1991 and then developed in an off-axis structure at the University of Naples in the late 90ties. Their flexibility and the transport regimes they allowed to reach made them suitable for both basic studies and application to superconducting electronics. The high quality it is possible to reach with the off-axis biepitaxial technique is testified also by the macroscopic quantum experiments recently carried out using these junctions. A particularly important feature is the lower barrier transmissivity, when compared with other HTS Josephson junctions’ structures. This is a key feature for preserving the directionality of the transport, thus making it possible to fully exploit the  $d$ -wave effects, as described in the last paragraph of this work. The biepitaxial structure is, at the moment, one of the most promising candidate for the application of HTS to superconducting electronic. Further steps in this direction could be made thanks to the advantages obtained when reducing the junctions’ size, as mentioned above. This could bring an added value to the biepitaxial structures, combining the high quality of the off-axis junctions’ barrier, the flexibility of the biepitaxial design and the possibility to get new insight in the physics of HTS materials given by the nanotechnology.

Great attention in this dissertation is paid to the innovative technological aspects of the realization of both micrometric and sub-micrometric HTS biepitaxial junctions, and also to the equipment used to characterize the realized devices.

- The first two chapters are dedicated to the general theory of Josephson junctions and HTS materials and devices, in order to provide a background for the following. In the first chapter, HTS materials will be introduced, pointing out the differences with conventional superconductors of relevance for the arguments developed in the following parts. The general phenomenology of the Josephson effect will also be outlined. The second chapter contains a review of the main properties of HTS junctions. The various techniques to realize this type of device will be described, and a detailed analysis of their main properties will be given. A brief review of the proposed mechanisms ruling the transport in these structures will be given, along with a detailed description of the effects induced by the  $d$ -wave symmetry of the order parameter. In this chapter we will discuss also the possible tools that can be used to determine the higher or lower quality of HTS junctions, as concerns the junctions' microstructure, the possibility to tune the properties in accordance with specific applications requirements and the possibility to preserve the  $d$ -wave induced effects. One of these tools is the junctions' magnetic pattern, from the study of which it is possible to obtain a number of fundamental information on the junctions' structure.
- From chapter 3 to chapter 5 the experimental techniques involved in the realization and characterization of the biepitaxial junctions will be described. Chapter three covers the issues related to thin films deposition and characterization. During the optimization of the junctions, great care has been given to the refinement of the thin films quality. The films were realized using two different deposition techniques, and systematic investigations were carried out using x-ray diffraction, atomic force microscopy and scanning electron microscopy in order to investigate both the composition and the structure of the films. Chapter 4 is dedicated to the patterning procedures used to define the junctions geometry and dimensions. This step is probably the most delicate one, due to the sensitivity of HTS materials to the environment conditions. The patterning can be divided in two phases: the realization of a protective mask and the removal of the material outside the mask. The dimensions of the mask, hence the techniques used to realize it, will therefore define the dimension of the resulting structures. During this work both micrometric and sub-micrometric junctions were realized using photolithography and electron-beam lithography respectively. It is important to stress that the biepitaxial technique is a rather complex one; therefore the realization of sub-micrometric structures is a technologically challenging problem.  
In the fifth chapter we will describe the measurement techniques used to characterize the devices. The advances in the device's quality achieved during these years go indeed in parallel with a fine-tuning of the measurement equipments and techniques. We will therefore describe the improvements that have been realized in order to make high quality, low noise measurements.
- The transport characterization of the junctions realized during this work is described in the sixth chapter. We will firstly describe the properties of the micrometric junctions, which are among the best HTS junctions reported in the literature and the most significant to isolate intrinsic  $d$ -wave induced effects. Mesoscopic behaviour will be discussed in natural, self-protected nano-channels along with the performances of sub-micron junctions. We will show how the reduced size of the junctions helps in obtaining a better control of the structure and brings clearly to light effects of interest for electronic applications.

## **1. General theory of HTS and Josephson junctions**

In this chapter, we will briefly introduce  $\text{YBa}_2\text{Cu}_3\text{O}_{6+x}$  (YBCO), the material used in this work and the most widely HTS studied in the world. We will outline the basic features of this material, from the structural and the electrical points of view and the differences between HTS and conventional superconductors. Then, we will outline the basics of the Josephson effect ruling the behaviour of the devices realized and studied during this work. The role of the specific properties of HTS in the phenomenology of the Josephson effect will be discussed in chapter 2 .

### **1.1. High temperature superconductivity**

The first high temperature superconductor to be discovered, in 1986 [1], was a La-doped barium cuprate compound, with a critical temperature ( $T_C$ ) of 30K. It was a step forward from the previous record of 23K detained from a conventional superconductor based on niobium and germanium. After this first discovery, in a few years the research for compounds with higher and higher critical temperature flourished. A few months later it was shown that a related compound,  $\text{YBa}_2\text{Cu}_3\text{O}_{6+x}$  (YBCO), had a  $T_C$  of 92K. Several other materials have been discovered since then; the record at ambient pressure is held by a thallium-doped mercuric-cuprate with  $T_C=138\text{K}$ .

#### **1.1.1. YBCO crystalline structure**

The structure of YBCO is rather complex, if compared with low temperature superconductors, that are plain metals and alloys; it is composed of three stacked perovskitic cells, at the centre of the middle cell there is an yttrium atom, the other two cells contain one barium atom each (Figure 1.1). The yttrium atom is surrounded by two Cu-O planes, while on the top and the bottom of the cell there are Cu-O chains. The superconducting transport takes place in the Cu-O planes, while the Cu-O chains act as a charge reservoir. Therefore, YBCO as well as the other HTS cuprates is mostly two dimensional in the transport properties. In the following chapters of this thesis, when dealing with the transport properties of HTS devices, we will often refer just to the Cu-O planes. When illustrating the junctions structure, as an example, it is of common use to represent just the Cu-O planes.

In all cuprates superconductors, superconductivity is achieved through an appropriate doping. In the case of YBCO, the doping species is the oxygen, resulting in the formula:  $\text{YBa}_2\text{Cu}_3\text{O}_{6+x}$  with  $x>0.4$  (see Figure 1.1d).

#### **1.1.2. Doping mechanism**

YBCO thin films are realized through processes taking place at high temperatures and in presence of oxygen (a detailed review of the deposition processes used during this work can be found in chapter 3). In these conditions, the compound is tetragonal with equal length of the in plane lattice parameters ( $a=b$ ), and the oxygen positions Ob1 and Ob2 in Figure 1.1 are empty. This structure is not superconducting. In order to move along the x axis of the phase diagram of Figure 1.1d, thus to obtain a superconducting behaviour, a doping procedure is carried out with an annealing at high temperature and in high oxygen pressure soon after the deposition of the film. As the oxygen content increases, additional atoms occupy Ob1 and Ob2 sites randomly up to a critical doping ( $x=0.4$ ) for which a tetragonal-orthorhombic phase transition occurs. For higher doping oxygen in Ob1 and Ob2 sites becomes partially ordered. Finally for  $x = 1$  (maximum oxygen content), all Ob1 sites become occupied and all Ob2 empty [2]. Through the doping,

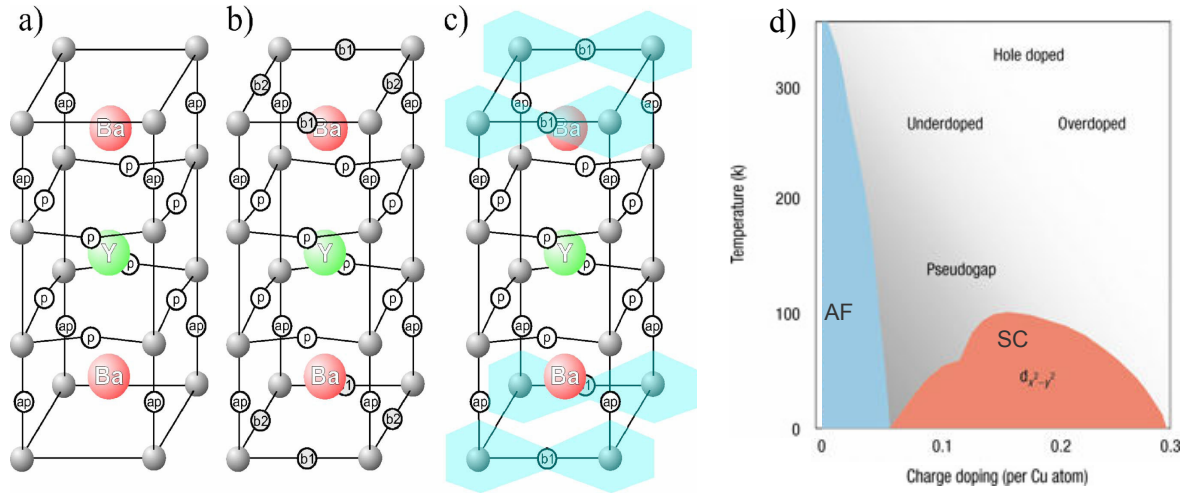


Figure 1.1 Crystal structure of  $\text{YBa}_2\text{Cu}_3\text{O}_{6+x}$ . Gray and open circles are copper and oxygen atoms, respectively. The effect on oxygen doping is shown: (a)  $x=0$ : Ob1 and Ob2 sites are empty; (b)  $x$  from 0 to 1: Ob1 and Ob2 sites occupied in random or ordered manner, depending on actual value of  $x$ ; (c)  $x=1$ : oxygen is ordered forming chains: all Ob1 sites are occupied and Ob2 sites are empty. In d) the phase diagram of YBCO is shown.

therefore,  $\text{CuO}$  chains running in the  $b$  direction with O vacancies on the chains are formed. The resulting symmetry is orthorhombic with  $b$  slightly larger than  $a$  (Figure 1.1c).

The  $\text{CuO}_2$  planes are made of  $\text{Cu}^{2+}$  and  $\text{O}^{2-}$  ions, resulting in a net charge of -2 units for unit cell. Nevertheless, the total structure must of course be electrically neutral. When the system is doped, the vacancies in the  $\text{CuO}$  chains are used to compensate for the excess negative charge in the  $\text{CuO}_2$  planes: vacancies in the  $\text{CuO}$  chains are transferred to the planes, with a corresponding change in the carrier density available. The carriers are sharply localized in the planes, for this reason YBCO and all the other cuprate superconductors have extremely anisotropic properties in both the normal and the superconductive states, with poor conduction in the  $c$  direction [3].

The superconducting YBCO composition is not stoichiometric. Therefore, this material is very reactive and tends to exchange oxygen with the atmosphere. This is the origin of the well known aging problem of YBCO and of all the other cuprate superconductors. The ease with which YBCO loses oxygen becomes even a bigger hurdle when dealing with device fabrication. When exposed to air, YBCO tends to react with  $\text{H}_2\text{O}$  and  $\text{CO}_2$  to form hydroxides and carbonates [4, 5]. This corroded surface layer has been shown to grow slowly on  $c$ -axis oriented films exposed to air at room temperature but, at elevated temperatures or during exposure to water (as devices fabrication procedures often require resist curing at high temperature and the use of water-based developers) irreversible corrosion is expected to be strongly enhanced. Another source of damage is the ion milling procedure; many consider this fabrication step the most “dangerous” one for the mechanical damage caused by the ion bombing on the structures’ edges and the heating caused by the interaction with energetic ions. The ions energy is indeed high compared with the binding energy of the chain oxygen atoms. Another possible origin for oxygen loss may stem from chemical reactions between the film and the resist or developer. During this work, we tried to improve our devices’ fabrication procedure in order to establish a reliable process that could minimize the damage to the superconductive film structure and produce devices with a longer lifetime. This goal is important not only for HTS based devices but for all the cases when sensitive materials are to be manipulated for the realization of electronic devices.



## 1.2. BCS theory

Before dealing with superconducting properties of HTS materials, we will briefly outline the principles of the theory of conventional superconductors. With the term conventional we indicate low temperature superconductors, metals and alloys, and  $\text{MgB}_2$  an interesting compound whose superconductivity was discovered in 2001, with  $T_c = 39\text{K}$  and BCS behaviour.

The discovery of superconductivity dates back to 1911, but we have to wait more than 40 years for the first microscopic theory of conventional superconductivity, published in 1957 by Bardeen, Cooper and Schrieffer [6] and known as BCS theory. In superconductors the transport electrons form a condensate and their behaviour can be described by a single wave function that is, therefore, macroscopic. The condensation of the electrons is accomplished through the interaction of the electron themselves with the lattice: below a temperature known as critical temperature, an electron travelling induces a deformation in the lattice which, in turn, is seen as a weak attractive force by a second electron with opposite momentum and spin. Through this deformation, called phonon, the two electrons are coupled in a Cooper pair. Since the electrons of the Cooper pairs have opposite momentum due to the Pauli exclusion principle, all pairs act as bosons, therefore it is possible for the pairs to condensate in the same quantum state. In a phenomenological description of the superconducting state, Ginzburg and Landau introduced the concept of superconducting order parameter [7] to describe the macroscopic properties of a superfluid condensate. The position dependent order parameter  $\Psi(\mathbf{r}) = |\Psi(\mathbf{r})|e^{i\phi(\mathbf{r})}$  is characterized by the phase  $\phi(\mathbf{r})$  and modulus  $|\Psi(\mathbf{r})|$ . The quantity  $|\Psi(\mathbf{r})|^2$  is a measure of the local density of Cooper pairs, and the distance over which  $\Psi(\mathbf{r})$  can vary without energy increase is called coherence length  $\xi$ . The coherence length can be seen also as the radius of the orbital state of the pair and is temperature and material dependent; in conventional superconductors  $\xi$  can reach hundreds of nanometres. It should be noted that the separation between electrons in a Cooper pair for a conventional superconductor is large enough that millions of other pairs have their centres of mass positioned between them, therefore the pairs should not be considered as isolated, but entangled with millions of other pairs.

The BCS theory introduces also an energy gap  $\Delta(T)$  between the BCS ground state and the first excited state. It is the minimum energy required to create a single particle (quasiparticle) excitation from the superconducting ground state. This energy gap inhibits the creation of excitations in the superconducting state and dominates the low temperature electrical transport and optical properties of superconductors. The energy gap is most clearly demonstrated and measured by tunnelling measurements into superconductor-insulator-normal metal ( $S-I-N$ ) junctions; they exhibit a conductance peak at voltage  $V = \Delta/e$  [8]. Gor'kov [9] linked the Ginzburg-Landau theory and the BCS theory showing that the order parameter is proportional to the energy gap. In momentum space, the two parameters are linked through the following relation:  $\Psi(\mathbf{k}) = \Delta_k / 2E_k$  where  $E_k$  is the quasiparticle excitation energy [10].

The wave functions corresponding to the Cooper pairs in BCS superconductors are spatially symmetric like the sphere of the atomic  $s$ -orbital, reflecting the symmetry of the underlying crystal lattice. The pairing mechanism in a conventional superconductor is thus called  $s$ -wave.

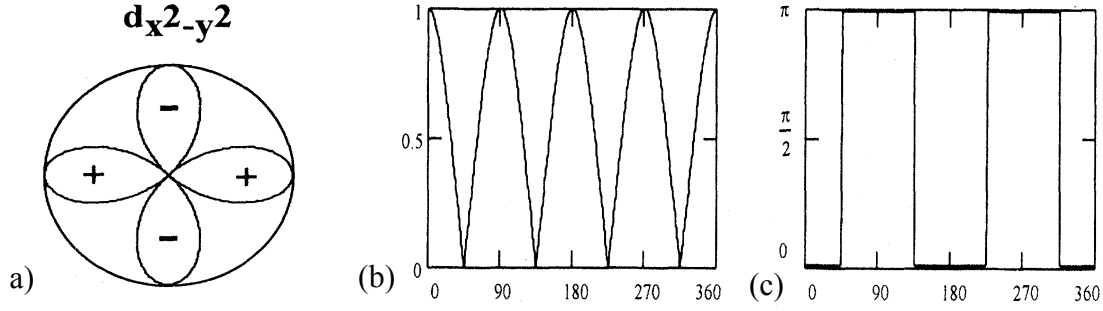


Figure 1.2 D-wave pairing symmetry: (a) plot in  $k$ -space; (b) the magnitude  $|\Delta|$  and (c) the phase  $\phi$  plotted as functions of direction in the  $\text{CuO}_2$  planes

### 1.2.1. Symmetry of the wave function in high temperature superconductors

Soon after the discovery of HTS superconductors, it was recognized that these materials do not behave as ordinary BCS superconductors. The transition temperature appeared too high to be explained with a phonon-coupling mechanism and there was also extensive evidence that the energy gap is not fully formed. Other mechanisms that could create a pairing interaction sufficiently strong to yield superconductivity at these elevated temperatures have been investigated since the beginning, but at the present, no definitive answer has been found.

A striking difference with conventional superconductors is the symmetry of the wave function. All cuprate superconductors have a tetragonal or orthorhombic crystalline structures, therefore the ratio between the lattice constants  $c$  and  $a$  is high. This anisotropy reflects in the transport properties of HTS, such as the superconducting coherence length and the room-temperature ratio of out-of plane to in-plane resistivities. Indeed, the results of band-structure calculations for various cuprates all show energy bands predominantly derived from the  $\text{CuO}_2$  planes, with no significant dispersion in the  $c$ -axis direction [10].

The pairing symmetry should reflect the symmetry of the underlying Cu-O square/rectangular lattices. This restricts the range to, basically, three symmetries ( $s$ ,  $d$  and  $p$  wave, in analogy to the atomic orbitals). Most pairing symmetry tests yielded convincing evidence for a predominant  $d_{x^2-y^2}$ -wave order parameter [8, 10, 11, ]. In the case of YBCO, the fact that the unit cell has an orthorhombic symmetry, with the  $b$  axis slightly longer than the  $a$  one, could induce a mixed pair state, with the addition of a real  $s$ -wave component to the predominant  $d_{x^2-y^2}$ -wave order parameter, as demonstrated by Kirtley et al. [12].

The properties of the devices considered in this work are influenced mainly by the  $d_{x^2-y^2}$ -wave symmetry, therefore, in the following, we will overlook the eventual presence of the small  $s$ -wave component.

The energy gap (order parameter) of the  $d_{x^2-y^2}$  state has the following functional form in  $k$  space:

$$\Delta(k) = \Delta_0 [\cos(k_x a) - \cos(k_y a)]$$

where  $\Delta_0$  is the maximum gap value and  $a$  the in plane lattice constant. The gap is strongly anisotropic, with nodes along the (110) directions in  $k$  space and a sign change between the lobes in the  $k_x$  and  $k_y$  directions. Physically, lobes of different sign indicate a relative phase of  $\pi$  in the superconducting condensate wave function for Cooper pairs with orthogonal relative momentum. In Figure 1.2 this symmetry is plotted, along with the magnitude and phase as a

function of angle in k-space.

In the following Table 1-1 two fundamental lengths, the London penetration depth  $\lambda^1$  and the coherence length  $\xi$  of YBCO are compared with the ones of a conventional superconductor.

Nb		YBCO	
$\lambda(\text{nm})$	39	$\lambda_{\parallel}$	150
		$\lambda_{\perp}$	1600
$\xi(\text{nm})$	80	$\xi_{\parallel}$	1.2
		$\xi_{\perp}$	0.3

Table 1-1 London penetration depth and coherence length of Nb, a conventional superconductor, and YBCO. In this last case, the parallel and perpendicular directions refer to the  $a$ - $b$  plane of the unit cell.

### 1.3. Theory of Josephson junctions

The Josephson effect was predicted by Brian Josephson in 1962 [13], originally for two superconductors connected through an insulating layer (tunnel junctions). He had learnt of the tunnelling experiments of Giaver involving superconducting junctions [14], but at that time the probability that the two electrons forming a Cooper pair could tunnel simultaneously through the barrier was considered very small, so that any effect might be unobservable. Josephson, instead, starting from the assumption of the presence of a phase difference between the superconducting electrodes, calculated that the zero voltage supercurrent flowing through the barrier would have the same order of magnitude of the quasiparticle current. He also predicted that if the junction is biased with a voltage  $V$ , the phase difference would evolve in time.

Many experimental confirmations followed Josephson's theoretical work; now the Josephson effect is well studied and represents an important tool for the study of superconductivity and for superconductors' applications.

As mentioned, the theory of the Josephson effect was originally developed for tunnel junctions [13, 15]. Nevertheless, it is valid whenever two superconductors are connected via a region of suppressed superconductivity (for instance, weak link) [16]. It is a very general phenomena. In the following paragraph, we will briefly illustrate the main concepts of Josephson effect along with its typical phenomenology.

#### 1.3.1. Derivation of the Josephson equations

The derivation method we are going to describe is only one of the possible ways to derive the Josephson equations (in some cases, it is possible to derive these equations directly from the microscopic theory). The Feynman method stresses the weak coupling nature of the Josephson current: we have Josephson effect as long as the macroscopic wave functions of the two electrodes overlap in the barrier region. It is important to stress the fundamental role played by the barrier: its characteristics (as for example the higher or lower transmissivity) will determine how much the wave functions can penetrate it, thus the properties of the junction. Barriers can be realized using insulating materials (S-I-S junctions) and also normal metals

---

<sup>1</sup> The London penetration depth  $\lambda$  expresses the fundamental properties of superconductors to screen magnetic fields: an applied field will penetrate into a superconductor only the sort distance expressed by  $\lambda$ .

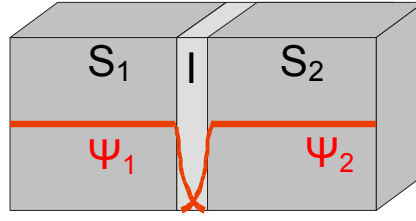


Figure 1.3 Sketch of an S-I-S Josephson junction with order parameter profiles

(S-N-S junctions) or a superconductor with a lower critical temperature (S-S'-S junctions).

Suppose that we have two superconductors separated by a thin insulating layer, as in Figure 1.3 with the two wave functions  $\Psi_1$  and  $\Psi_2$  weakly coupled with a strength  $K$ . Hence, we can write two equations for the amplitudes on each side of the insulator [15]:

$$\begin{aligned} i\hbar \frac{\partial \Psi_1}{\partial t} &= E_1 \Psi_1 + K \Psi_2 \\ i\hbar \frac{\partial \Psi_2}{\partial t} &= E_2 \Psi_2 + K \Psi_1 \end{aligned}$$

If we consider a d.c. potential  $V$  across the junction, the potential  $E_1$  and  $E_2$  are shifted by an amount  $eV$ , and consequently:  $E_1 - E_2 = 2eV$ . We can choose the zero energy halfway between the values  $E_1$  and  $E_2$ :

$$\begin{aligned} i\hbar \frac{\partial \Psi_1}{\partial t} &= -eV \Psi_1 + K \Psi_2 \\ i\hbar \frac{\partial \Psi_2}{\partial t} &= eV \Psi_2 + K \Psi_1 \end{aligned}$$

we can substitute for  $\Psi_1$  and  $\Psi_2$  their expressions:

$$\Psi_1 = \rho_1^{1/2} e^{i\varphi_1} \quad \Psi_2 = \rho_2^{1/2} e^{i\varphi_2}$$

Separating the real and imaginary terms in each equation we get:

$$\begin{aligned} \frac{\partial \rho_2}{\partial t} &= \frac{2}{\hbar} K \sqrt{\rho_2 \rho_1} \sin \varphi \\ \frac{\partial \rho_1}{\partial t} &= -\frac{2}{\hbar} K \sqrt{\rho_2 \rho_1} \sin \varphi \end{aligned} \tag{1.1}$$

$$\begin{aligned} \frac{\partial \varphi_2}{\partial t} &= \frac{K}{\hbar} \sqrt{\frac{\rho_2}{\rho_1}} \cos \varphi + \frac{eV}{\hbar} \\ \frac{\partial \varphi_1}{\partial t} &= \frac{K}{\hbar} \sqrt{\frac{\rho_2}{\rho_1}} \cos \varphi - \frac{eV}{\hbar} \end{aligned} \tag{1.2}$$

where  $\varphi = \varphi_2 - \varphi_1$ . The pair current density  $J$  is given by:

$$J \equiv \frac{\partial \rho_2}{\partial t} = -\frac{\partial \rho_1}{\partial t}$$

therefore, from equations (1.1) one obtains:

$$J = J_1 \sin \varphi \quad (1.3)$$

where  $J_1 = 2K / \hbar \rho$  and  $\rho_1 = \rho_2 = \rho$  is assumed constant. Equation (1.3) can be written also, in terms of current, as:

$$I = I_C \sin \varphi$$

From the two equations (1.2) it follows:

$$\frac{\partial \varphi}{\partial t} = \frac{2eV}{\hbar} \quad (1.4)$$

Equations (1.3) and (1.4) are known as Josephson equations in d.c. and a.c. respectively. At zero voltage, equation (1.4) gives a phase difference between the electrodes that is constant, not necessarily zero; therefore a finite current density can flow through the barrier. This is the essence of the d.c. Josephson effect. If we apply a constant voltage  $V \neq 0$ , it follows from equation (1.4) that the phase varies in time, therefore an alternating current appears, with frequency  $\omega = 2\pi\nu = 2eV / \hbar$  (a.c. Josephson effect).

Equation (1.3) is just the simplest form that the first Josephson equation can take. In the case of HTS, the symmetry of the order parameter modifies this equation and the current-phase relation. As is sketched in Figure 1.2c, the phase of HTS order parameter undergoes a shift of  $\pi$  every 90 degrees, inducing a change in the sign of the supercurrent:

$$I_s = I_C \sin(\varphi + \pi) = -I_C \sin \varphi \quad (1.5)$$

Junction exhibiting such behaviour are called “ $\pi$  junctions”. This is one of the distinguishing effects of HTS devices and is fundamental for their applications. We will dedicate section 2.3 to a detailed analysis of it.

It is also possible to derive a more general form of the first Josephson equation from more general assumptions. This derivation will allow us to highlight some features of the Josephson current of great relevance in the case of HTS junctions [16, 17].

There are some general properties that must be valid for all the theoretical models attempting to describe the Josephson effect:

- A change of  $2\pi$  in the phase of the junction should not imply any change in the physical state of the system nor in the current across the junction. Therefore, the current-phase relation (CPR) should be periodic of  $2\pi$ :

$$I_s(\varphi + 2\pi) = I_s(\varphi)$$

- Supercurrent can flow only when there is a gradient on the order parameter phase. As a result, the curve  $I_s(\varphi)$  intersects the horizontal axis at  $\varphi = \pi n$ :

$$I_s(\pi n) = 0$$

- Opposite currents are equivalent, therefore the function  $I_s(\varphi)$  is symmetrical with respect to the origin

$$I_s(\varphi) = -I_s(-\varphi)$$

This condition is not valid in junctions where the time-reversal symmetry is broken (TRSB). Recently, it was suggested that TRSB can occur spontaneously in d-wave junctions [18]; nevertheless, no clear experimental proof is available at the moment.

From the points listed above, it can be derived that the supercurrent can always be expanded in Fourier series:

$$I_s(\varphi) = \sum_{n \geq 1} I_n \sin(n\varphi) \quad (1.6)$$

equation (1.6) is identical to (1.3) when the terms of order higher than one are negligible, as happens in classical tunnel-like junctions. In HTS devices, on the other hands, higher order components can be significantly enhanced for particular configurations, due to the *d*-wave symmetry of the order parameter. The importance such effects for the application of HTS junctions will be described in section 2.3.4.

### 1.3.2. Josephson junctions in a magnetic field

One of the essential aspects of the Josephson effect is the occurrence of diffraction and interference of supercurrents when the junction is immersed in an externally applied magnetic field. The magnetic behaviour of the critical current is a powerful tool for the study of Josephson effect and can be seen as a “fingerprint” of the junction itself. By studying this behaviour, it is possible to get a deep insight on the junction’s structure, on the quality and properties of the barrier, on the current distribution in the junction and on the effects of the *d*-wave order parameters. In this paragraph, we will illustrate the main phenomenology of this effect, leaving a detailed description of the influence of the *d*-wave symmetry of the order parameter to section 2.3.3.

Josephson junctions can be classified in “short” or “long” depending on the ratio between the width  $w$  of the junction and the Josephson penetration depth

$$\lambda_J = \sqrt{\frac{\Phi_0}{2\pi J_c(2\lambda + d)}}$$

where  $d$  is the thickness of the barrier,  $J_c$  the critical current density,  $\lambda$  the London penetration depth and  $\Phi_0$  is the magnetic flux quantum. The Josephson penetration depth is the length the magnetic field can penetrate inside the junction before being screened by the Josephson current. Since  $\lambda_J$  depends on the critical current, it can vary in a wide range, even for the same junctions’ structure, depending both on the quality of the barrier, the presence of impurity, the quality of the film etc. If  $w > \lambda_J$  the junction is called “long”: in the magnetic behaviour of the junction, the screening current have to be taken into account. On the other hand, if  $w \ll \lambda_J$ , the magnetic field will penetrate uniformly into the junction, and it will be called “short”. In the case of sort junctions, an external field  $H_y$  applied in the plane of the junction (see Figure 1.4a) induces a linear spatial variation of the phase. From the Josephson equations (1.3) and (1.4) the following relation for the total current in the junction can be calculated (for

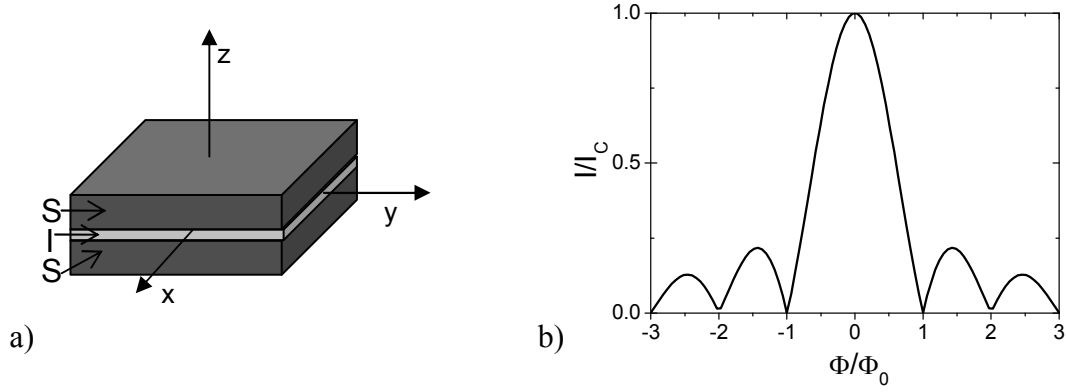


Figure 1.4 Sketch of a rectangular junction (a) and the calculated modulation of the critical current in magnetic field (b)

a detailed derivation see Ref.15):

$$I = \iint dx dy J_1(x, y) \sin\left(\frac{2\pi d}{\Phi_0} H_y x + \varphi_0\right) \quad (1.7)$$

where the integral is calculated over the junction area and the critical current density is assumed to be spatial dependent, in order to account for nonuniformity effects in the barrier. In the simplest case of a rectangular junction with uniform current distribution, the modulation of the critical current operated by the magnetic field will be described by the formula:

$$I_c(\Phi) = I_{c0} \frac{|\sin(\pi\Phi/\Phi_0)|}{|\pi\Phi/\Phi_0|} \quad (1.8)$$

which is the formula of a Fraunhofer pattern, the same that is obtained for a beam of light passing through a rectangular slit. This pattern is shown in Figure 1.4.

The behaviour described by equation (1.8) is the simplest one; it will be found only in junctions with a perfectly uniform barrier. As we will show in the following chapter, in the case of HTS the interplay of the d-wave symmetry of the order parameter and the microstructure of grain boundaries give rise to more complex effects.

### 1.3.3. The RCSJ and tilt washboard models

Josephson junctions can be modelled using the “resistively shunted junction model”, which allows a general classification of weak links. We can draw an equivalent circuit for the junction (Figure 1.5) including a nonlinear Josephson element in parallel with a resistor  $R$ , representing the junction’s normal resistance, and a capacitor  $C$ , representing the geometrical capacitance [15, 19]:

$$I = I_c \sin \varphi + V/R + C dV/dt \quad (1.9)$$

A wide variety of current-voltage (I-V) characteristics can be modelled using the appropriate choice of parameters. We can pass from the tunnel-like behaviour, for high values of the capacitance, showing hysteretic behaviour, to a regime where capacitance is almost

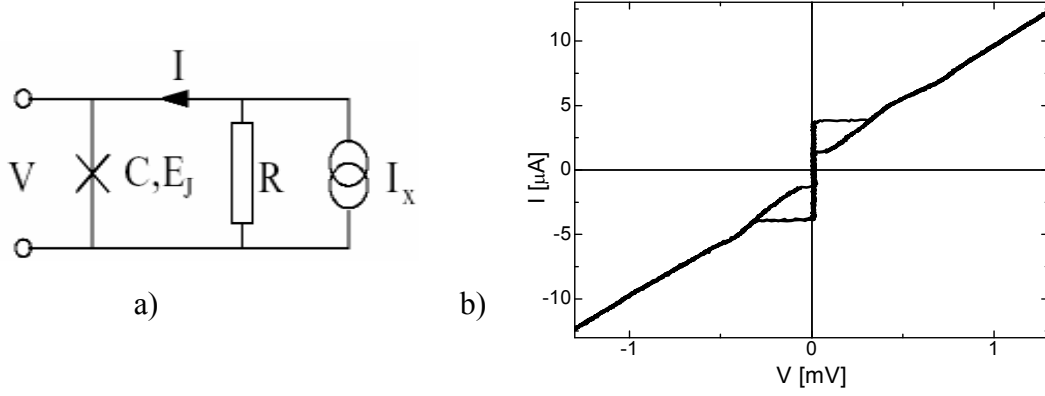


Figure 1.5 (a) Sketch of the RCSJ circuit used to model many aspects of Josephson junctions' phenomenology; (b) an hysteretic I-V characteristic, measured at  $T=0.3\text{K}$ , of a biepitaxial junction fabricated during this work. The junction has a width of  $0.8\mu\text{m}$  and misorientation angle  $\theta=75^\circ$ , critical current density  $J_C=2.5\times 10^3\text{A/cm}^2$ , normal state resistance  $R_N=110\Omega$ . The hysteresis is  $\sim 68\%$ .

zero and no hysteresis is present. HTS junctions generally present a phenomenology consistent with negligible or low capacitance barriers. Biepitaxial junctions are one of the few examples of HTS junctions that can show, in the proper barrier configuration, a significant capacitance, thanks probably to their particular microstructure (as we will show in the next chapter). An example is shown in Figure 1.5b for a junction realized during this work.

Setting  $V = (\hbar\partial\phi)/(2e\partial t)$  from the second Josephson equation(1.4), we obtain:

$$I = \frac{\Phi_0}{2\pi} C \frac{\partial^2 \phi}{\partial t^2} + \frac{\Phi_0}{2\pi} \frac{1}{R} \frac{\partial \phi}{\partial t} + I_C \sin \phi$$

This can be expressed as:

$$\left(\frac{\Phi_0}{2\pi}\right)^2 C \frac{\partial^2 \phi}{\partial t^2} + \left(\frac{\Phi_0}{2\pi}\right)^2 \frac{1}{R} \frac{\partial \phi}{\partial t} + \frac{\partial}{\partial \phi} U = 0 \quad (1.10)$$

where

$$U = -\Phi_0 / (2\pi) (I_C \cos(\phi) - I\phi) \quad (1.11)$$

Equation (1.10) describes the motion of a ball moving in a “tilted washboard” potential  $U$  (see Figure 1.6). The term involving  $C$  represents the mass of the particle, the  $I/R$  term represents the damping of the motion, and the average “tilt” of the washboard is proportional to  $-I$ . For values of  $I < I_C$ , the particle is confined to one of the potential wells and the average voltage across the junction is zero (points A and B in Figure 1.6). An increase of current  $I$  will have the effect of tilting the washboard potential. When the current exceeds  $I_C$ , the particle rolls down the washboard, the junction switches to the resistive state and a voltage appears across it (point C in Figure 1.6). However, a finite voltage can be generated even before  $I_C$  is reached due either to a classical effect involving thermal fluctuations driving the fictitious particle out of its equilibrium position by climbing over the potential barrier, or to a quantum one. In this second case, the fictitious particle of coordinate  $\phi$  overcomes the potential barrier tunnelling through it. This effect is called macroscopic quantum tunnelling (MQT) and is indicated with an arrow in Figure 1.6. The MQT effect is one of the macroscopic quantum effects of greatest interest for the study of fundamental physics of superconducting devices. It has been deeply



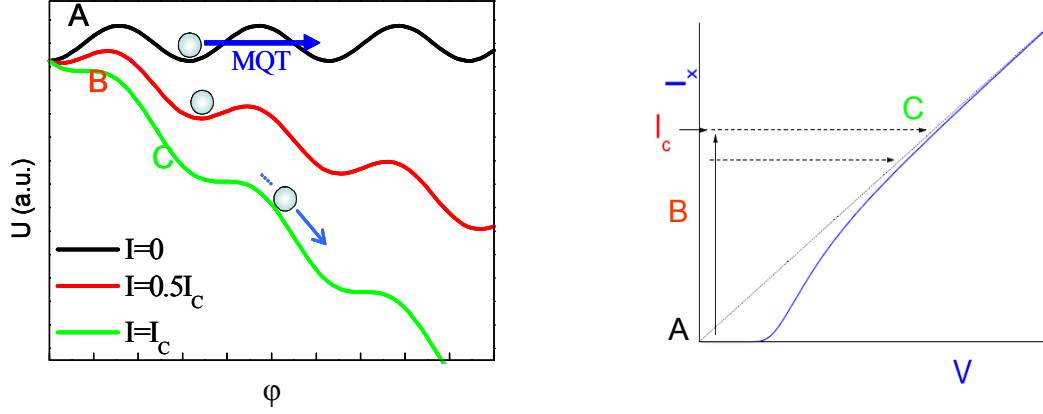


Figure 1.6 Plot of the washboard potential and dynamic of the phase “particle”.

studied theoretically and proved experimentally in Josephson junctions realized with conventional superconductors [20]. Today, advances in nano and film deposition technologies allows a good control of this effect in such junctions, leading to proposals of Josephson junction systems as key structures for superconducting “qubits” [21]. In this framework, HTS junctions could offer the additional advantages of *d*-wave order parameter symmetry for a “quiet” qubit [22]. A demonstration of quantum phenomena in HTS systems could help to get novel insights into their nature and of the materials themselves. We will deal with important implications of such phenomenon in HTS systems in the next chapter.

The presence of a capacitance in the junction’s properties affects what happens after the switching. Given the Stewart-McCumber number [15]:

$$\beta_c = \frac{2e}{\hbar} R^2 C I_{c0}$$

if  $\beta_c \gg 1$ , the junction will switch from the superconducting state to a finite voltage  $V > 0$ . In this case, the junction will be hysteretic and heavily underdamped. On the contrary, if  $\beta_c \ll 1$  the junction is called overdamped (in this case the capacitance is very small).

Since HTS junctions have little or no capacitance, they belong to the overdamped category. Overdamped junctions are useful for such applications in which non hysteretic junctions are required, such as SQUIDs (superconducting quantum interference devices). On the other hand, there are many other applications in which the hysteresis is a positive feature; when, for example, the switching to the resistive state has to be clearly detected. An HTS junctions’ design allowing the realization of both overdamped and underdamped devices would be favourable for electronics applications. The biepitaxial design used during this work proved to be very flexible in this respect. In Figure 1.7 some examples of both underdamped and overdamped biepitaxial junctions are shown. The I-V characteristics of Figure 1.7a refer to MgO based biepitaxial junctions, the characteristics of Figure 1.7b to CeO<sub>2</sub> based ones.

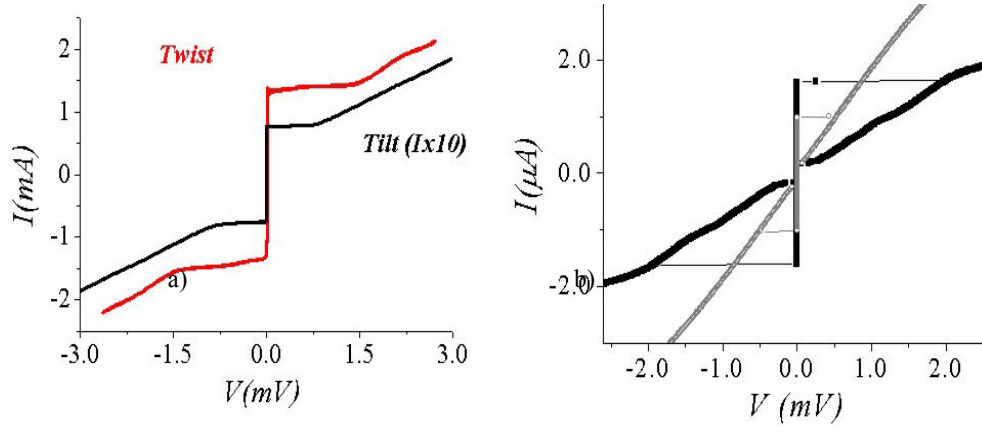


Figure 1.7  $I$ - $V$  characteristics of biepitaxial grain boundary YBCO Josephson junctions in the two limits of low capacitance (left) and high capacitance (right). Hysteretic behaviour is evident in the latter case. For each limit we show two different examples. Curves on the left (right) refer to MgO-(CeO<sub>2</sub>) based biepitaxial junctions in the tilt and twist limits, respectively.

## **2. Grain boundary Josephson junctions**

In the previous chapter, the basics of the Josephson effect were described. We pointed out that the effect manifests itself whenever the wave functions of the two superconducting electrodes, penetrating in the barrier, overlap. The simplest way to realize a weak coupling between the wave functions is the one sketched in Figure 1.3: to interpose an insulating layer between the two superconducting electrodes. When dealing with HTS, this technique is very hard to pursue, given the crystal structure, the short coherence length, the chemical complexity of these materials. An alternative approach was found in artificial grain boundaries (GBs). A GB is a plane where two crystal orientations come in contact. In order to accommodate the two different lattices, the formation of defects in the grain boundary plane is necessary [23]. The type and amount of defects depend greatly on the misorientation angle of the two lattices, among them there are dislocations, changes in the stoichiometry, intergranular phases, microcracks. The GB is therefore a highly disordered zone. It has been found that, in HTS, grain boundaries with a misorientation angle greater than  $8^\circ$  act as a barrier, giving the possibility to weakly link the wave functions of the two superconductors. The most used way to controllably fabricate such grain boundaries will be described in the following paragraph. The characteristics of the barrier in these structures are, unfortunately, very difficult to predict, being influenced by a large number of parameters, many of which is not possible to control directly. The barrier properties of the GBs are, indeed, governed by the disorder, it would be desirable to be able to introduce the amount of disorder in a controllable way. While we can control the misorientation angle of the electrodes (in the next paragraph it will be shown how), we can only try to limit the presence of impurities, growing films of better quality on the appropriate substrates, as an example. The unpredictability of GBs properties is one of the factors that has hindered, until now, the development of large scale applications of HTS junctions, where a high degree of reproducibility is needed.

Another, important factor for the limited development of these devices has been the lack in understanding of their working mechanisms (the two problems are probably connected: if we can understand the behaviour of GBs we could probably realize more reliable devices). It is still not clear the nature of the GB barrier and what is the mechanism ruling the transport across it.

A third key feature in the study of HTS GBs is the interplay between the asymmetry of the HTS order parameter and the morphology of the GBs. As will be shown later in this chapter, this interplay has a fundamental role in determining the peculiar properties of HTS Josephson junctions.

In this chapter, we will briefly review the most used GBs structures (limiting our attention to the types of junctions more promising for electronic applications) and the mechanisms which have been proposed to rule the transport in GBs. Since the peculiar symmetry of the order parameter is a key feature in HTS devices applications, great part of the chapter will be dedicated to the effects of this symmetry on GBs transport, in order to highlight which aspects of GBs' phenomenology are required for electronic applications. All this will enter in the discussion of the experimental data that will be presented in chapter 6.

### **2.1. Classification of grain boundary junctions**

Grain boundaries are described using two parameters:

- The misorientation angle  $\theta$  between the crystallographic directions of the two electrodes;
- The type of rotation of the axes: tilt around the  $c$  axis, tilt around the  $a$  or  $b$  axis or

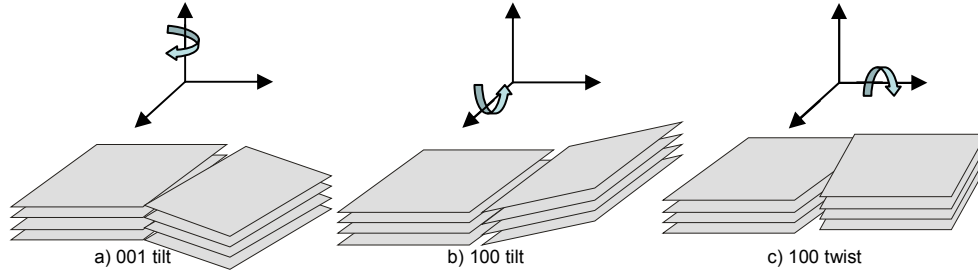


Figure 2.1 Different configurations of GBs: (a) tilt around the  $c$  axis, (b) tilt around the  $a$  axis, (c) twist around the  $b$  axis

twist along the junction interface.

In Figure 2.1 the three type of rotations are sketched.

The misorientation angle and the type of rotation have great influence on the GB transport properties. In the case of twist rotation, the planes are nominally in contact only through an array of points, whereas in the tilt case the contact regions are lines. In Figure 2.2, a collection of transport data of different types of junctions is presented [19, 24]. Striped ovals refer to the twist case, black bars to the tilt one. In general, the increase of the misorientation angle brings an exponential decrease of the critical current density. This behaviour can be explained with the fact that, in order to accommodate two crystal lattice with a high misorientation angle, it is necessary to create more defects. Therefore, the nominal thickness of the GB barrier grows.

There are different ways to obtain GBs with controlled orientations, leading to Josephson junctions with different properties. We will describe the most important ones in order to be able to compare the junctions realized during this work with the state of the art in the field.

### ***Bicrystal junctions***

The bicrystal technique is the most direct way to create a controlled GB. It is based on the use of a substrate created joining two single crystals with different orientations. The HTS film will follow, during the growth, the relative orientations of the two parts of the substrate, therefore a GB will be reproduced in correspondence of the joining line in the substrate (Figure 2.3a). Commercially available bicrystal substrates of many compounds, including  $\text{SrTiO}_3$ ,  $\text{MgO}$ , yttria-stabilized zirconia, and  $\text{LaAlO}_3$  have been used for the realization of HTS junctions [19].

As concerns the GB orientations, the (001) tilt configuration is the most used. Recently, also bicrystal junctions having a  $45^\circ$  (001) tilt and an additional (100) tilt have been realized; they show interesting features for the study of fundamental aspects of high temperature superconductivity [25].

The diffusion of bicrystal technique is due also to its simplicity and extendibility to all HTS compounds and deposition methods. Compared to the other techniques, the bicrystal is the one requiring less patterning steps and the only one in which the HTS film grows on a surface that has not been previously manipulated. Nevertheless, this technique has a huge shortcoming in the preset and fixed position of the grain boundary. This lack of flexibility leads to poor efficiency for circuit design.

### ***Step-edge junctions***

The step edge technique exploits the epitaxial growth in an alternative way. When YBCO finds a steep step in the substrate, it changes its growth in order to accommodate the change in the underlying lattice. By patterning a step with a suitable slope in the substrate, it

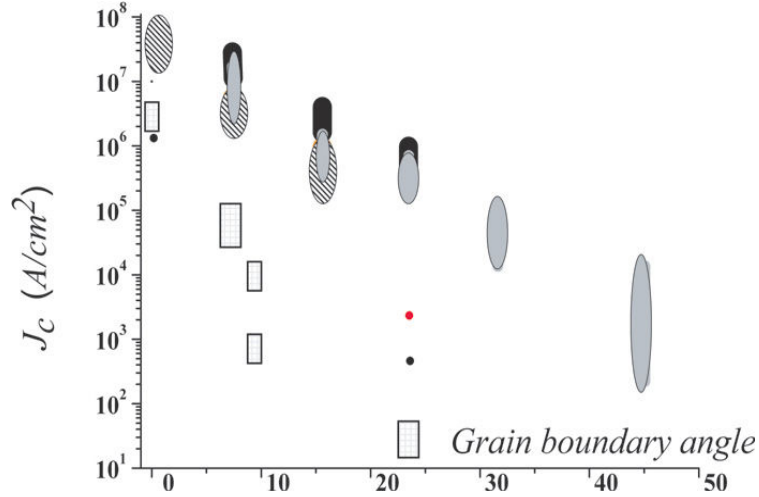


Figure 2.2 Critical current density versus misorientation angle for different types of junctions. The data refer all to YBCO junctions, except the open rectangles and the points, which correspond to  $\text{Nd}_{1.85}\text{Ce}_{0.15}\text{CuO}_{4-x}$  junctions and CBCO junctions respectively [19]

is possible to control this growth and obtain the nucleation of grain boundaries. Typically, two grain boundaries are nucleated at one substrate step, one at its bottom and one at its top. These grain

boundaries are connected in series (Figure 2.3b) [19, 24].

Since the steps are photolithographically defined, the junctions can be positioned anywhere on the substrate, therefore this technique is very flexible. The main disadvantage is that the properties of these junctions depend strongly on the step properties. Various detailed studies trying to correlate YBCO step-edge junction characteristics with their microstructure have been carried out. In terms of Josephson performances, the best junctions (with unfortunately poor reproducibility) are obtained on steep steps ( $\alpha > 60^\circ$ ).

### **Biepitaxial junctions**

The biepitaxial technique uses changes of the orientation of an HTS film grown on a structured template substrate. In the original technique, developed by Char and co-workers [26], an r-plane sapphire was partially covered by MgO, then a  $\text{SrTiO}_3/\text{YBCO}$  bilayer was grown on top. The MgO induced an in plane rotation of  $45^\circ$  in the  $\text{SrTiO}_3$ , therefore, a  $45^\circ$  [001] tilt grain boundary was created in the YBCO film.

More recently, the biepitaxial technique has been extended to novel configurations, in which one of the electrodes does not grow along the  $c$ -axis orientation [27, 28, 29]. In this configuration, an MgO or  $\text{CeO}_2$  seed layer is grown on a  $\text{SrTiO}_3$  (or  $\text{LaAlO}_3$ ) (110) substrate and patterned. Then, an YBCO film is deposited on the structured substrate, resulting in a (001) oriented growth on the seed layer and a (103) oriented growth on the substrate (Figure 2.3c). The relative orientation of the two electrodes, the (001) and the (103) one, can be changed at will with the patterning of the substrate, enabling the realization of  $45^\circ$  tilt junctions and  $45^\circ$  twist junctions and all the possible admixtures of them. When  $\text{CeO}_2$  is used, an additional  $45^\circ$  in plane rotation of the YBCO takes place. This feature has proved to be of extreme importance for taking advantage of the d-wave order parameter symmetry induced effects [28, 30, 31].

$\text{CeO}_2$  based biepitaxial junctions have been realized and studied in this work. Here, we will just mention the main advantages and disadvantages of these devices, postponing a deeper analysis of their structure and properties to the next chapters.

Among the main advantages of this kind of junctions there is the possibility to tune their

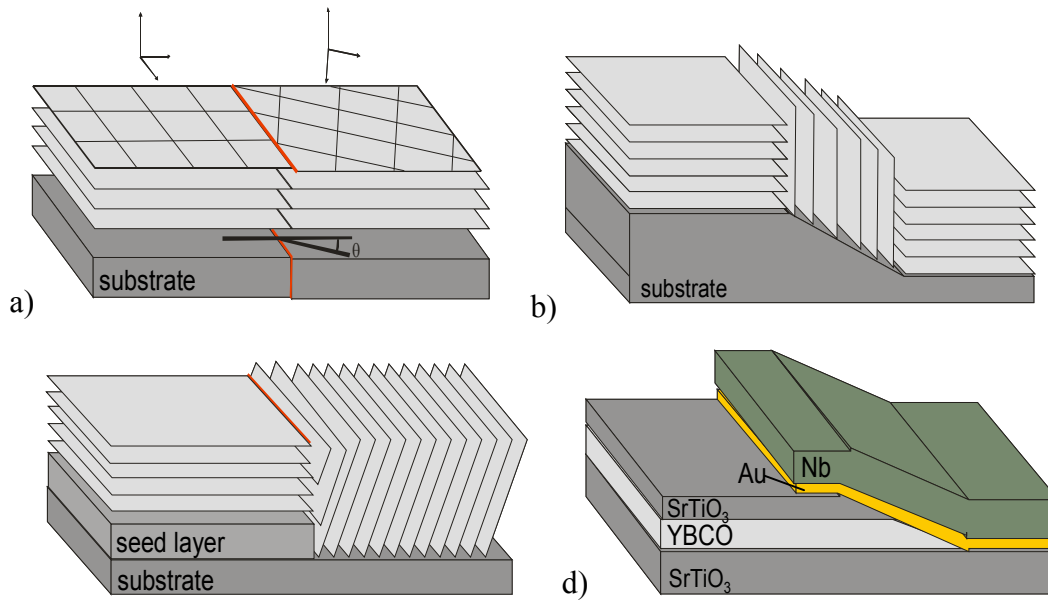


Figure 2.3 Sketch of HTS junctions main techniques; a) bicrystal, b) step edge, c) biepitaxial, d) junction with artificial barrier

properties in a wide range, in particular the critical current density and the normal state resistance, changing the relative angle of the two electrodes. Moreover, the junctions can be placed anywhere on the chip, a great plus for electronic design. Among the disadvantages there is a more complex fabrication procedure. When compared to bicrystal junctions, biepitaxial structures require one patterning step more, to define the seed layer geometry. Moreover, the deposition of the HTS film takes place on a processed substrate, rather than on a bare one, increasing the chances for imperfections and spurious phases growth. Indeed, biepitaxial junctions show, on average, a larger spread in the transport properties.

### ***Junctions with artificial barrier***

An alternative to grain boundary technique for HTS electronic is the ramp-type junctions developed in the University of Twente [32]. They employ a Nb counter-electrode, therefore are limited in the working temperature range, and an Au artificial barrier. In this technique, ramp edges are produced in [001] oriented, pulse laser deposited YBCO films using photolithography and Ar ion etching. The devices are returned to the deposition chamber, etched and cleaned, and then thin layers of YBCO and the Au barrier are deposited by pulsed laser deposition *in situ*. The junctions are completed with the Nb counter electrode (Figure 2.3d). This process eliminates a degraded layer of YBCO next to the Au, allowing the realization of a neat barrier. Moreover, by adjusting the Au-barrier thickness, the critical current density can be tuned over a wide range.

These junctions proved to have excellent characteristics and reproducibility; they are used for fundamental studies on YBCO properties and, thanks to their controllability, on *d*-wave induced effects on junctions' transport, as will be described in the next paragraphs.

### ***Summary of junctions' properties***

The techniques described until now have lead to junctions with remarkably different features. We can divide between structural properties and electrical ones.

From the structural point of view, an important aspect for the use of HTS junctions in

electronic application is the possibility to place the junctions anywhere on the chip, allowing an efficient design of the device. A great advantage is also the possibility to fabricate junctions with different properties on the same chip.

From the electrical point of view, junctions that allow the tuning of the transport properties in a wide range are favoured. This tuning can be achieved, as we mentioned, in different ways: changing the misorientation angle in the biepitaxial case, or the barrier width in the case of junctions with artificial barrier. Reliability is also another important point. The change in the structure of the junctions should lead to change in transport properties in a predictable way. The problem of GB junctions consists in the disordered nature of the GB barrier. On one hand, the disorder is the reason itself of GBs behaving as barriers; on the other, it can affect the junction's properties in an unpredictable way. The solution to this problem follows two complementary approaches: to try to get a better and better control on the GB barrier structure and to realize junctions in which the microscopic structure of the GB has less influence if compared to the intrinsic properties of HTS. During this work, we tried to pursue both ways: we improved the fabrication procedure of biepitaxial junctions and showed that these type of devices are, thanks to their particular design, very robust to disorder.

In order to be able to compare the results we obtained with the state of the art in this field, in Table 2-1 we report the values of  $I_C R_N$  and  $R_N A$  for various type of YBCO-based junctions. These data were extracted from Ref. [19] and [24] (see also Figure 6.8 in chapter 6). For applications of Josephson junctions the characteristic voltage  $I_C R_N$  is of great relevance, as it is proportional to the characteristic Josephson frequency of the junction and thereby provides an upper limit for its speed of operation. For most applications one wants the  $I_C R_N$  product to be as large as possible. The normal state interface resistivity  $R_N A$  gives information about the nature of the GB barrier.

	$I_C R_N$ (mV)	$R_N A$ ( $\Omega\text{cm}^2$ )
Bicrystal	0.1 - 2	$10^{-9} - 10^{-7}$
Biepitaxial	0.5 - 2	$10^{-7} - 10^{-5}$
Step-edge	0.6 - 1	$10^{-4} - 10^{-2}$
Au artificial barrier	0.24	$10^{-8} - 10^{-9}$

Table 2-1 Parameters of the most used type of YBCO junctions. The spread of the values is in some case due to the change in the misorientation angle of the GB.

## 2.2. Grain boundary mechanisms

To account for the transport properties of GBs, many mechanisms have been suggested. Grain boundaries are disordered regions in which, by definition, the lattice structure is modified. Therefore, a microscopic description of GB mechanisms has to be based on a quantitative model of pairing in the cuprates where spatially dependent parameters of the crystal lattice are included. At present, this model is missing and our understanding of the pairing mechanisms in the cuprates is incomplete; as a result any description of the superconducting properties of HTS grain boundaries must also be incomplete.

In this paragraph, the most significant mechanisms will be outlined. Probably, the transport properties of GBs result from the interplay of several of them, filtered by the barrier microstructure of each particular system. The distortion in the crystal lattice caused by the matching of the different orientations gives rise to stress fields. The electronic structure of the superconductor is therefore modified, the pairing interactions are suppressed, and quasiparticles are scattered [24]. The result is a lowering of the superconducting order parameter at the GB interface and a decrease in critical current density. With increasing

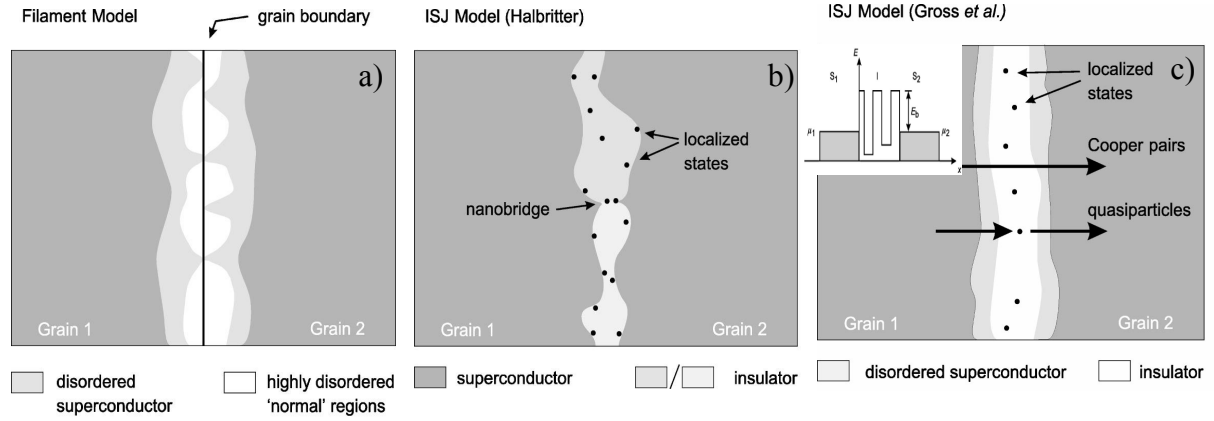


Figure 2.4 Sketches of the phenomenological models proposed for GBs transport. In the filament model proposed by Moeckly (a) superconducting filaments are embedded in a highly disordered normal matrix; (b) and (c) panels show the ISJ models proposed by Halbritter and Gross with localized states. In the inset the energy profiles corresponding to the Gross model are shown

misorientation, the width of the disordered layer at large-angle boundaries increases linearly; this behaviour has been recognized as one reason for the angular dependence of  $J_C$ .

The disorder at the GB interface could result also in changes of the superconductors' stoichiometry and formation of spurious phases. Most important, it could cause defects in the oxygen sublattice. If the oxygen concentration becomes low enough, the superconducting properties will be lost and the material will become locally insulating. As the oxygen concentration or the carrier density may be non uniform, grain boundaries may be highly inhomogeneous, with the creation of insulating regions alternating with superconducting filaments, as suggested by Moeckly et al. [33]. It has been shown that this filament model, which is illustrated in Figure 2.4a, consistently describes the resistance, capacitance and  $I_C R_N$  products of grain-boundary Josephson junctions.

In the intrinsically shunted junction (ISJ) models, proposed by Gross [34] (Figure 2.4c) and Halbritter [35] (Figure 2.4b), transport properties of the boundaries are described by assuming the presence of an insulating layer with oxygen defects or oxygen disorder, and including localized states. Quasiparticles are supposed to tunnel resonantly across this layer, predominantly via one localized state, while Cooper pairs are supposed to tunnel directly (see inset of Figure 2.4c). While this model could explain spatial inhomogeneities of  $J_C$  with variations of the barrier width, the result of several experiments are in disagreement with some other implications [24]. According to the ISJ model, the  $I_C R_N$  product of the grain boundaries is expected to show a universal scaling behaviour:  $I_C R_N \propto J_c^q$  with  $q=0.5 \pm 0.1$  [24, 34], which has been subject of debate. Furthermore, according to the model, grain-boundary properties are supposed to change substantially when changing the HTS material, due to the different oxygen kinetics and chemistry, which is clearly not the case.

A very likely hypothesis is that all these structural mechanisms contribute, with different weights, to define the transport phenomenology. Among the many factors contributing there are some related to the material used, as for example its peculiar structure, the growth mode and the tendency to grow spurious phases; and some related to the junction design, as for example the misorientation angle that could favour one mechanism more than the others. All these microstructure-related issues could mask the real transport mechanism in GB junctions, as well as intrinsic effects in HTS phenomenology. The future of HTS electronics, therefore, relies also on the possibility to realize devices in which the peculiar microstructure of the grain boundary plays a less and less important role in favour of intrinsic controlled effects of HTS.



## 2.3. Effects of the *d*-wave symmetry of the order parameter in HTS junctions

For a complete understanding of GB junctions' phenomenology it is important to include the effects of the symmetry of HTS order parameter and the interplay between this symmetry and the microstructure of the GB. In this paragraph, we will examine the main effects of such interplay. We will show how it is possible to isolate intrinsic *d*-wave effects, which is a neat qualitative check for the junctions and represents the first step for possible use of HTS for innovative applications.

### 2.3.1. Effects on the critical current density

An immediate effect of the oscillation of the *d*-wave order parameter symmetry magnitude (see Figure 1.2b) on HTS junctions' properties is the scaling of the critical current density with the misorientation angle of the junction. As can be seen from Figure 2.5, changing the misorientation angle in an HTS junction means to change the way the order parameters of the two electrodes see each other. This change reflects in the junctions properties: when two lobes of the order parameters face each other, a maximum values of the critical current density is expected, when the misorientation angle is such that the node are facing, no supercurrent should flow across the junctions. This behaviour is described in the Sigrist-Rice approach [36], where the Josephson current is proportional to the projection of the momentum-dependent energy gap onto the junction normals. The following relation is produced:

$$J_s = A_s \cos(2\theta_1) \cos(2\theta_2) \sin \phi \quad (2.1)$$

where  $\theta_1, \theta_2$  are the angles of the crystallographic axes with respect to the interface and  $A_s$  is a constant characteristic of the junction. In Figure 2.5b, equation (2.1) is plot, as an example, for an asymmetric bicrystalline configuration: assuming  $\theta_1 = 0$  and changing  $\theta_2$ .

It should be emphasized that, in the derivation of the Sigrist-Rice formula, it is assumed that the interface is uniform and smooth. Furthermore, only the tunnelling processes perpendicular to the junction interface are considered. In real GB junctions, due to the complexity of the structure, the electron wave vector normal to the junction interface can be significantly distorted by interface roughness, oxygen deficiency, strain etc. In other words, usually the nominal angle of the junctions is not preserved in the transport process, this last one takes place through a "cone" more than in a single direction. Indeed, early attempts to highlight the pairing symmetry of the cuprate superconductors from the dependence of the critical current from the junction angle relative to the cuprate crystalline axes were hindered by the uncontrolled nature of the junction interfaces.

However, recently, success in this area has been reported using biepitaxial junctions [28]. They were realized using  $\text{SrTiO}_3$  as a substrate and  $\text{CeO}_2$  as a seed layer. Patterning the seed layer via optical lithography, it was possible to realize, on the same chip, junctions with different reciprocal orientation of the two electrodes. We would like to stress that such a design is impossible to realize with bicrystal and the step-edge technique, as the misorientation angle is set by the substrate, in the first case, and by the ion milled step angle, in the second; therefore is fixed for all the junctions on the chip.

The critical current density was measured and compared with the Sigrist-Rice formula(2.1), adapted to our biepitaxial configuration:

$$J_c \approx \sin 2\theta (2 - \cos^2 \theta) (1 - 3 \sin^2 \theta) / (1 + \sin^2 \theta) \quad (2.2)$$

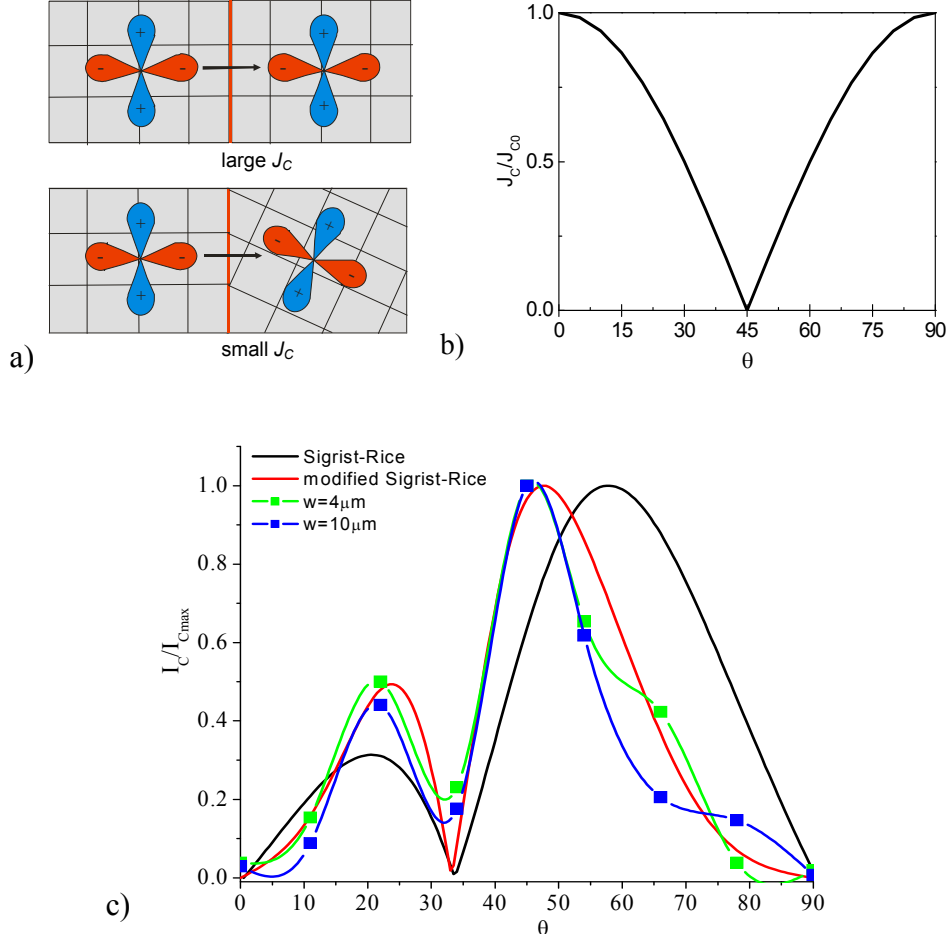


Figure 2.5 Illustration of the mechanism by which the critical current density of grain boundaries is reduced due to  $d$ -wave symmetry of the order parameter (a); critical current density vs. misorientation angle for a junction with  $d$ -wave electrodes, as follows from the Sigrist-Rice formula (b) and in the case of biepitaxial junctions (c). In (c) the critical current  $I_c$  vs. angle  $\theta$  for two sets of biepitaxial junctions ( $10\mu\text{m}$  and  $4\mu\text{m}$  wide) prepared on the same chip is shown as blue and green squares. Solid lines connecting experimental points are guides for the eye.  $I_c$  values are normalized to their maximum. Experimental data are compared with the original Sigrist-Rice formula and with a modified formula for slightly narrower lobes.

In Figure 2.5c the Sigrist-Rice theoretical behaviour is plotted as a solid line, the points represent the experimental data for two set of junctions of different width. The data show three minima at  $0^\circ$ ,  $35^\circ$  and  $90^\circ$ , as expected from the theory. Note that the minimum angle of  $35^\circ$  is different from  $45^\circ$  because of the compound angle formed by the crystalline axes in this type of grain boundary. These measurements were the first proof of an intrinsic  $d$ -wave effect in the phenomenology of single Josephson junctions (not inserted in any loop) independent of the interface details. The  $d$ -wave induced effects in these junctions are apparently very robust and the coherence related to the order parameter symmetry seems to be preserved on a scale larger than any interface impurity or defect characteristic length. This may be due to the junction configuration with low barrier transmission probabilities, which preserves the directionality of the Cooper pairs. The possibility to change, on the same chip, the interface orientation and to tune the  $d$ -wave induced effects is therefore a key advantage to select junctions with well-defined properties, independently of possible uncontrollable disorder along the GB.

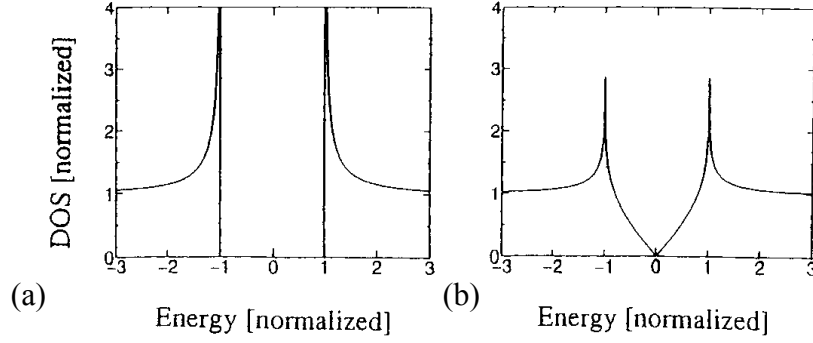


Figure 2.6 Density of states for (a) *s*-wave and (b) *d*-wave superconductors

### 2.3.2. Effects on the gap

As mentioned in section 1.2, the order parameter is proportional to the energy gap [9]. The energy gap is measured by tunnelling measurements, as Bardeen showed the equivalence between tunnelling conductance spectrum and the density of states in the low-temperature limit [37]. In conventional superconductors, tunnelling spectroscopy has been perhaps the most powerful tool used to investigate the electronic density of states near the Fermi level. The physics behind tunnelling spectroscopy is simple: in a Superconductor-Insulator-Normal metal junctions in thermodynamic equilibrium at zero degrees, the Fermi levels of the two electrodes are equal and no current flows through an external circuit connected between the metal and the superconductor. If an external positive voltage  $V$  is applied to the metal, electrons tunnel from the metal through the insulator to the unoccupied states of the superconductor. Therefore there will be a large peak in the tunnelling conductance as the bias voltage approaches the gap value,  $eV = \Delta$ . Conversely with negative bias, when  $eV = -\Delta$ , electrons will tunnel from the occupied states of the superconductor to the normal metal. In Superconductor-Insulating-Superconductor junctions there is a superconductor on both sides of the barrier and the tunnelling current starts to flow when  $eV = \Delta_1 + \Delta_2$  where  $\Delta_1$  and  $\Delta_2$  are the gaps of the two superconductors.

The proportionality between the conductance spectra and the density of states is described by the following formula:

$$\rho(E) = \frac{1}{2\pi} \int_0^{2\pi} d\theta \rho_{BCS}[E, \Delta(\theta)] \quad (2.3)$$

where

$$\rho_{BCS}[E, \Delta(\theta)] \equiv \text{Re} \left[ \frac{|E|}{\sqrt{E^2 - |\Delta(\theta)|^2}} \right]$$

In conventional superconductors, the pair potential has not orientational dependence ( $\Delta(\theta) = \Delta_0$ ) while in *d*-wave superconductors  $\Delta(\theta) = \Delta_0 \cos 2\theta$  (see Figure 1.2b). As a consequence, the conductance spectra will change following the orientation of the gap. Equation (2.3) is plotted in Figure 2.6 for a *s* and a *d*-wave superconductor. The gap structure for *s*-wave superconductors has a U-shaped flat bottom. On the other hand, that for the *d*-wave superconductors shows V-shaped structure reflecting the variation of the amplitude of the pair potential in *k*-space [38].

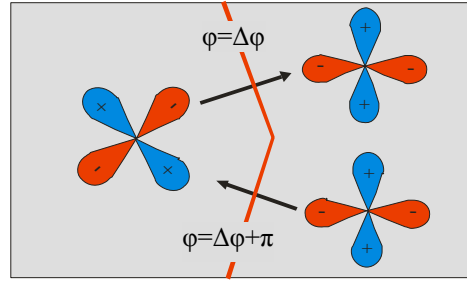


Figure 2.7 Due to the phase difference of adjacent lobes of the  $d$ -wave order parameter and grain-boundary faceting, the Josephson current flows across some facets in opposite directions

There are various experimental techniques to form tunnelling junctions; among them, scanning tunnelling microscopy has the ability to detect spatially resolved information, which means both geometrical data and spectroscopic data can be obtained through measurements on well defined surfaces. For the other methods, the applicability is limited by the ability to fabricate the barrier layer without causing damage to the samples. As mentioned at the beginning of this chapter, S-I-S junctions are very difficult to realize using HTS and, on the other hand, the transmissivity of GB barriers is usually too high to allow tunnelling experiments. This issue will be analyzed in more detail in section 6.4.2.

### 2.3.3. $d$ -wave induced $\pi$ -shifts

In the previous sections we illustrated the effects induced by the oscillation of the magnitude of the  $d$ -wave order parameter when changing the direction of the transport in the  $a$ - $b$  plane. Important effects are also induced by the oscillation of the phase of the order parameter. We briefly introduced such effects in section 1.3.1 with the equation (1.5) we report again below:

$$I_s = I_c \sin(\phi + \pi) = -I_c \sin \phi$$

In brief, the shift of  $\pi$  between two adjacent lobes of the order parameter induces a change in the sign of the critical current. In HTS junctions these shifts can occur for particular configurations of the grain boundary line, as sketched in Figure 2.7. The consequences of  $\pi$ -shifts in  $d$ -wave junctions are numerous and of great relevance for the understanding of HTS mechanisms and possible applications. In this paragraph, the main effects will be highlighted.

#### **Magnetic field dependence of the critical current for a $0$ - $\pi$ junction**

It has been discussed in section 1.3.2 that the magnetic field dependence of the critical current  $I_c(H)$  for a straight junction with a uniform critical current density resembles the Fraunhofer pattern described by equation (1.8). The  $I_c(H)$  dependence becomes more complicated for junctions containing  $\pi$ -shifts.

In the “short junction limit” ( $w \ll \lambda_j$ ), for equal length of the  $0$  and  $\pi$  sections of the junction, the critical current becomes [19]:

$$I_c(\Phi) = I_0 \frac{|\sin^2(\pi\Phi/2\Phi_0)|}{|\pi\Phi/2\Phi_0|} \quad (2.4)$$

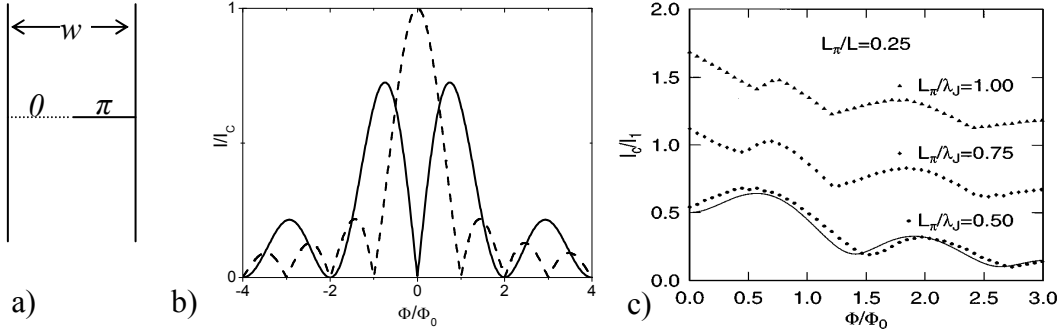


Figure 2.8 Sketch of a 0- $\pi$  junction (a); the junction critical current as a function of the magnetic field for: symmetric configuration in the short junction limit (b), an asymmetric configuration and three normalized junction length (c)

The critical current as function of applied field is plotted in Figure 2.8b with a solid line. For comparison, the Fraunhofer pattern from equation (1.8) is plotted with a dashed line in the same figure. The  $I_c(H)$  dependence for 0- $\pi$  junctions has zero critical current at zero applied field, in contrast with the Fraunhofer pattern which has a maximum. The maximum of the critical current in the 0- $\pi$  case is reached when the applied field is equal to  $1/2\Phi_0$ . Moreover, the modulation length is  $2\Phi_0$ .

In the opposite limit,  $w > \lambda_J$ , a 0- $\pi$  junction spontaneously generate a vortex at the intersection between the regions with 0 and  $\pi$  intrinsic phase shift. This vortex generates a total flux equal to  $\Phi_0/2$  threading through the junction. We will deal with the effects of such flux in the next section in more detail. Junctions with intermediate width  $w \approx \lambda_J$  spontaneously generate “semi fluxons” with total flux less than  $\Phi_0/2$ . A further variable is the length of the 0 and  $\pi$  sections of the junction. The magnetic field modulation of 0- $\pi$  junctions has been calculated by Kirtley et al [39] for a wide range of configurations. In Figure 2.8c the results of such calculations are shown for a junction where the length of the  $\pi$  region is 0.25 of the total length and for different ratios of the junction length to the Josephson penetration depth  $\lambda_J$ . The junction geometry assumed in [39] is slightly different from the grain boundary layout, however the results obtained are useful to underline the huge number of possible shapes of the modulation of the critical current with magnetic field in 0- $\pi$  junctions. From these considerations it emerges that the magnetic pattern is a fingerprint of the order parameter configuration, once the dimensions and the microstructure of the device are defined.

### **Spontaneous generation of flux in $\pi$ rings and junctions**

One of the most interesting effects associated with  $\pi$  shifts in d-wave junctions is that a superconducting ring containing an odd number of such shifts will (under certain conditions) spontaneously generate a magnetic field with half of the conventional flux quantization. This effect was, indeed, used to test the pairing symmetry of HTS superconductors in the famous experiment by Tsuei and Kirtley [10].

Consider a superconducting ring with a 0 or a  $\pi$  junction. The free energy of this system can be written as:

$$U(\Phi, \Phi_a) = \frac{\Phi_0^2}{2L} \left\{ \left( \frac{\Phi - \Phi_a}{\Phi_0} \right)^2 - \left( \frac{L|I_c|}{\pi\Phi_0} \cos \left( \frac{2\pi}{\Phi_0} \Phi + \gamma \right) \right) \right\} \quad (2.5)$$

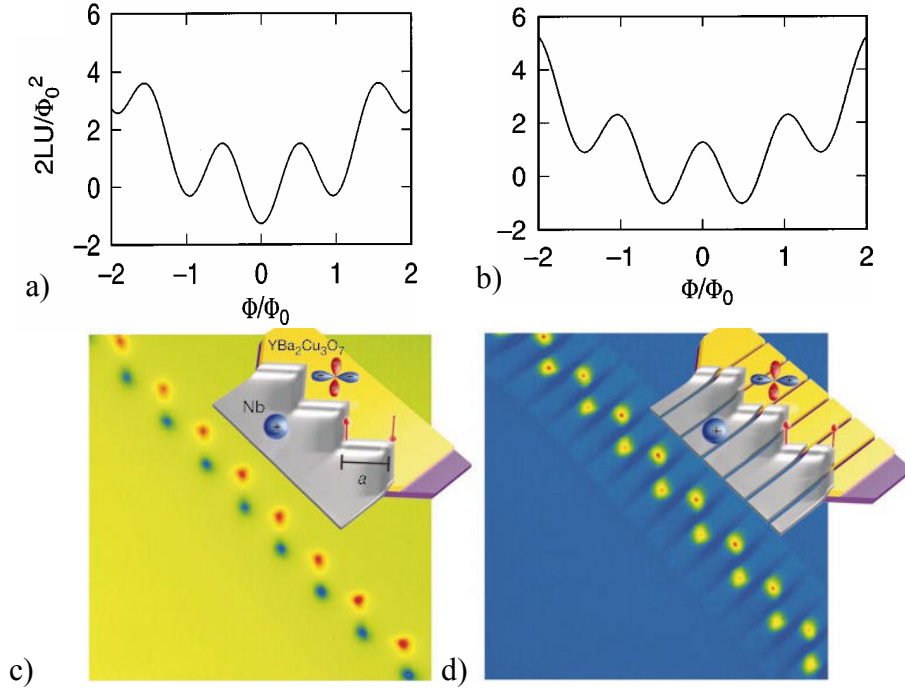


Figure 2.9 Spontaneous generation of flux due to the d-wave symmetry: free energy of a ring containing one 0 (a) and one  $\pi$  junction (b). Schematics and scanning SQUID microscope images of YBCO-Nb junctions (c): the  $\pi$  shift in the superconducting phase normal to the junction interface at each facet corner causes the spontaneous generation of half flux quantum vortex. The vortices order strongly antiferromagnetically when the junctions are connected (c) but only weakly for disconnected junctions (d).

where  $\Phi = \Phi_a + LI_S$  is the total magnetic flux threading the loop,  $L$  the self inductance and  $\gamma$  the phase shift equal to  $\pi$  in the presence of a  $\pi$  junction [10]. Plots of the free energy vs  $\Phi$  at  $\Phi_a=0$  are shown in Figure 2.9. The zero ring has a ladder of metastable states centred at the ground state  $\Phi=0$ , while the  $\pi$  ring has a ladder of states shifted by  $\Phi_0/2$ . Therefore, the ground state of the  $\pi$  ring will be doubly degenerate with  $\pm\Phi_0/2$  spontaneous magnetization. It is possible to demonstrate that this result holds for rings with an arbitrary number  $N$  of junctions, whenever there is an odd number of  $\pi$  shifts.

When the inner diameter of the superconducting  $\pi$  ring is reduced down to zero, the ring transforms into a corner junction, as the one sketched in Figure 2.7. In analogy to the ring, a spontaneous flux is generated. In an experiment by Hilgenkamp et al [40], such half quantum vortices in 0- $\pi$  junctions were imaged using scanning SQUID microscope. The junctions were realized using the artificial barrier technique described in section 2.1. The YBCO layer was patterned in order to obtain a zig-zag array of corner junctions, as sketched in the inset of Figure 2.9, and the length  $a$  of each facet was set in order to keep the junctions in the “long” limit:  $a > \lambda_J$ . In these conditions, the lowest-energy ground state of the system is expected to be characterized by the spontaneous generation of a half-integer flux quantum at each corner. This half-fluxon provides a further  $\pi$ -phase change between neighbouring facets, either adding or subtracting to the d-wave induced  $\pi$ -phase shift, depending on the half-flux-quantum polarity. In both cases, this leads to a lowering of the Josephson coupling energy across the barrier. In the scanning SQUID microscope image presented in Figure 2.9, a spontaneously induced magnetic flux is clearly seen at every corner of the zigzag structure. It is interesting to note that the fluxons are arranged in an antiferromagnetic fashion. When the corners are isolated by cutting the facets, the antiferromagnetic ordering becomes less strong (Figure 2.9d).

## ***Magnetic behaviour of faceted d-wave junctions***

In Figure 2.8b the magnetic modulations of the critical current for “ideal” 0 and  $\pi$  junctions were showed. For real junctions, the situation is more complicated. Most of the experimental critical current magnetic patterns show remarkable deviations from the ideal behaviour. In Figure 2.10 the magnetic patterns of two biepitaxial junctions studied during this work are showed. The junctions were realized on the same chip, the pattern on the left refers to a junction with a misorientation angle  $\theta=55^\circ$ , the one on the right to a junction with  $\theta=0^\circ$ . As it can be seen from Figure 2.5c, these two conditions correspond to the maximum and the minimum of the critical current. The first junction show a very regular Fraunhofer like pattern, the second pattern is characterized by the presence of two symmetric maxima at a finite field. This last one is a recurrent and distinctive feature of junctions with low  $J_C$ . These deviations from the ideal behaviour of grain boundaries have no analogies in conventional superconductors junctions and are referred to as anomalous patterns. The reason for such anomalies is to be found mainly in the interplay between the grain boundary real structure and the  $d$ -wave symmetry of the order parameter, as we will describe in this section.

The ideal behaviours showed in Figure 2.8b assume a perfectly uniform and straight barrier, therefore a grain boundary without imperfections. As we already highlight in section 2.2, grain boundaries are, on the contrary, disordered regions. The nucleation of dislocations, impurities and spurious phases is favoured. An additional complication comes from the growth mode of YBCO. It has been established that in YBCO, as well as in many other cuprates, the epitaxial growth takes place through the nucleation and growth of spiral like islands, eventually joining together to form a continuous film. As a consequence of being formed by a sequence of such islands, the grain boundary line cannot be perfectly straight, but it is characterized by meanders and facets whose length is in the order of 10-100nm. The facets orientations and lengths depend on many variables, such as the grain boundary configuration, the substrate quality, the conditions used for film deposition, and the presence of defects. Moreover, faceting, being the result of a 3D growth mode, takes place in all three dimensions. This feature has been observed for grain boundaries fabricated by all the usual techniques: bicrystals, biepitaxial and step edges. The interplay between the randomly oriented facets and the  $d$ -wave order parameter induce oscillations in the magnitude of the critical current density. Hilgenkamp et al [41] calculated the distribution of the critical current density for actual bicrystal junctions of various orientation, starting from the trace of the grain

boundary line extracted by transmission electron microscopy (TEM) studies; an example is shown in Figure 2.11a. It is clear that the critical current density is highly non uniform. Moreover, in some sections of the grain boundary line, the orientation of the facets is such that lobes of the order parameter with opposite sign face each other and  $\pi$  shifts occur (these section are marked with  $\pi$ ). As described in the previous section, the  $\pi$  phase shifts lead to spontaneous generated magnetic fluxes along the grain boundaries. Experiments to observe these spontaneous fields are challenging as the expected flux is smaller than a flux quantum  $\Phi_0$  and is presumed to fluctuate on a length scale as small as one micron; therefore a scanning SQUID microscope is needed. In Figure 2.11b and c we present the results of such measurement for a  $45^\circ$  asymmetric bicrystal junction [42] and for a  $\text{CeO}_2$  based biepitaxial structure [43] respectively. In both cases, the grain boundaries are marked by the presence of spontaneous magnetization. It is worth noting that the magnetization decreases when the ratio of the Josephson penetration depth  $\lambda_J$  to the facets spacing  $L_\pi$  becomes larger. This has been showed in Ref [43] by imaging samples realized with thinner YBCO films. The smaller critical current density of these films translates in a larger  $\lambda_J$ , therefore the ratio  $\lambda_J / L_\pi$  becomes large. In these conditions, no magnetization was revealed by scanning SQUID measurements. The threshold to observe spontaneous magnetization was found to be  $L_\pi \cong \lambda_J$ .



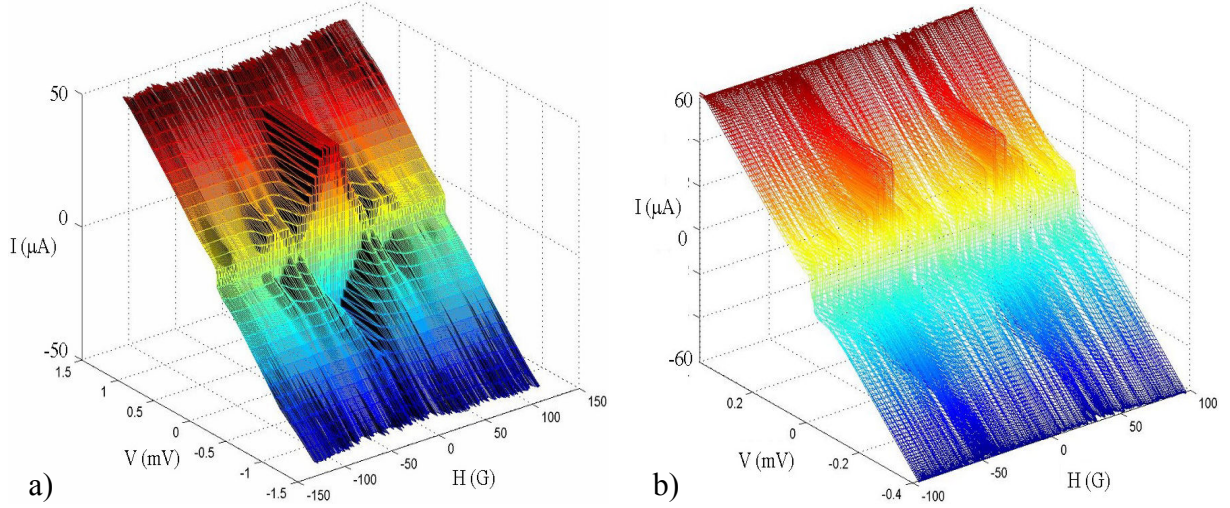


Figure 2.10 I–V curves as a function of the magnetic field are reported for a CeO<sub>2</sub>-based biepitaxial junction for different orientations of the barrier. Fraunhofer-like (a) and anomalous patterns (b) have been observed, corresponding to the maximum and the minimum in  $J_C(\theta)$ .

Additional insights in the role of faceting and the influence of the order parameter symmetry on the magnetic dependence of the critical current were obtained using, again, high quality YBCO and Nb based junctions with Au artificial barrier [44]. The zig zag geometry already shown in the insets of Figure 2.9c was used to simulate in a controllable way the faceting structure of grain boundaries. Up to 80 contacts were realized and, in analogy with grain boundary junctions, the individual elements of the array can be regarded as facets. All the facets were aligned along a  $[100]$  direction of the YBCO, and were designed to have identical (absolute) values of the critical current density  $J_C$ . The facets oriented along one direction are expected to exhibit an additional  $\pi$ -phase difference compared to those oriented in the other direction. Using this technique, it was possible to closely “reproduce” the most important features of anomalous magnetic patterns measured for GB junctions. Figure 2.12a presents the  $I_C(H)$  dependence for an array of eight facets of  $25\mu\text{m}$  width, placed in the zig zag geometry. Clearly, the maxima in the critical current are observed at a nonzero applied magnetic flux. The main features of the experimental pattern were reproduced using the following equation:

$$I_C(\Phi) = \left| \sum_{n=1}^N \left( \int_{(n-1)a}^{na} J_C h e^{in\pi} e^{-i\beta x} dx \right) \right| \quad (2.6)$$

where  $N$  is the number of facets with facet length  $a$ , and  $x$  is the coordinate of integration along the junction. The first exponent in this equation is related to the order parameter symmetry contribution to the phase difference along the junction, which varies between 0 and  $\pi$  every next facet. The term  $\beta x$  in the second exponent describes the phase difference at position  $x$  due to the applied magnetic flux, in the usual way. Assuming a constant  $J_C$  throughout the array, and a homogeneous distribution of magnetic flux, integration of equation (2.6) results in plot shown in Figure 2.12b. It can be seen that equation (2.6) reproduces the main features of the zig zag geometry. It is worth noting that this analysis does not take into account the effects of self generated flux we described in the previous section, as these effects become important as the facet length is comparable with the Josephson penetration depth.

In this section we reviewed the most important effects of the interplay between the  $d$ -



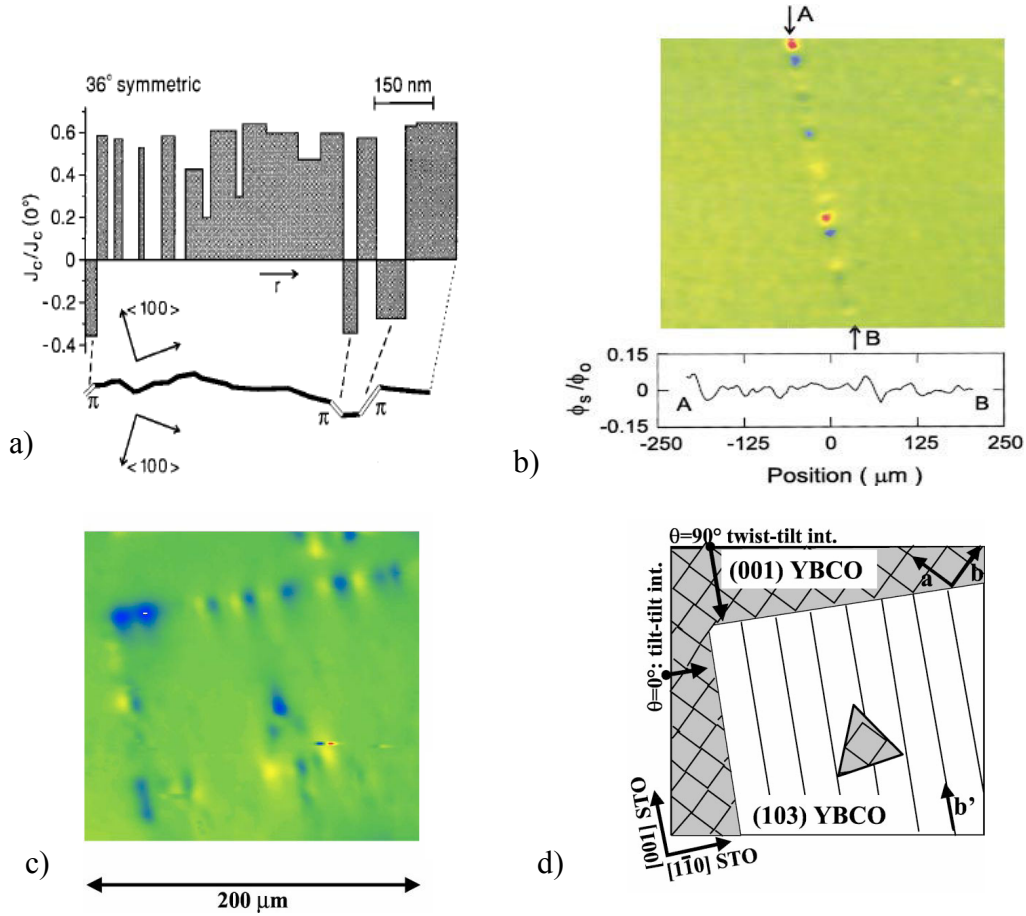


Figure 2.11 Spontaneous magnetization induced by grain boundary faceting in bicrystal and biepitaxial structures. In a) the trace of the faceted grain boundary line, extracted from a TEM image of a  $36^\circ$  symmetric bicrystal junction, is shown, together with the calculation of the critical current density for each facet. Note that some facets configurations leads to  $\pi$  shifts and negative critical current. Scanning SQUID analysis of faceted grain boundaries reveal the presence of spontaneous magnetization induced by such  $\pi$  shifts both for bicrystal (b) and for biepitaxial (c) junctions. In d) the sketch of the biepitaxial structure is shown.

wave symmetry of the order parameter and the irregular microstructure of grain boundaries. It was shown how this interplay is the reason for the anomalous magnetic pattern showed by most GB junctions configurations. The magnetic behaviour of grain boundary junctions is a powerful tool to investigate such effects. To summarize, we can say that the study of the  $I_c(H)$  pattern can give information about the uniformity of the barrier, the distribution of critical current density, the presence of facets and of  $\pi$  shifts in the phase of the order parameter, the spontaneous nucleation of magnetic flux at the facets corners. Therefore, it is used as one of the tools to determine the quality of a junction. The pattern shown in Figure 2.10a, for instance, is a rare example of Fraunhofer-like behaviour of GB junctions, indicating uniform barrier and critical current distribution. More often, GB junctions show an anomalous pattern, more similar to the one showed in Figure 2.10b. To be able to understand the reasons for such anomalous behaviour means that, now, it is possible to design devices where the spurious effects are limited.

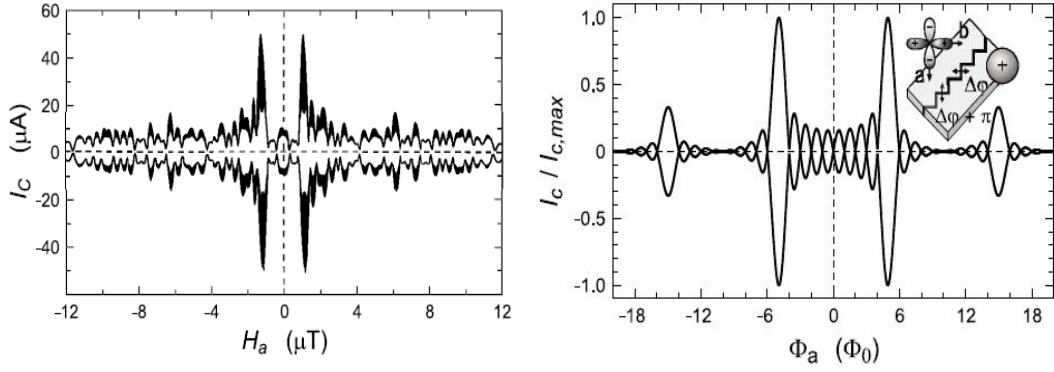


Figure 2.12 Current reported as a function of magnetic field for YBCO\_Au\_Nb zig zag junctions. (a) Experimental data for an array of 8 alternating 0 and  $\pi$  facets (25  $\mu\text{m}$  wide); (b) calculated magnetic flux dependence from an array of 10 facets

### 2.3.4. Effects of the 2<sup>nd</sup> harmonic in the current-phase relation

The  $d$ -wave symmetry of the order parameter can induce, in some junction configurations, effects of major importance in the current-phase relation (CPR). As we showed in section 1.3.1, the CPR of the junction can be expressed as the Fourier series expansion of equation (1.6). In this section, we will add to this equation the effects of the asymmetry of the order parameter.

Let us write again equation (1.6) considering the first and second order contributions:

$$I_s(\varphi) = I_1 \sin \varphi + I_2 \sin 2\varphi \quad (2.7)$$

In the previous section we remarked that, since the order parameter is bound to the crystal lattice, the supercurrent of a junction between two  $d$ -wave superconductors depends on the orientation of the  $d$ -wave electrodes with respect to their boundary. Let  $\theta_1$  and  $\theta_2$  denote the angle between the normal to the junction interface and the  $a$  axis in electrodes 1 and 2. The term  $I_1$  is strongly dependent from such angles. The symmetry of the problem dictates that [17, 19]

$$I_1 = I_C \cos 2\theta_1 \cos 2\theta_2 + I_S \sin 2\theta_1 \sin 2\theta_2 \quad (2.8)$$

The coefficients  $I_C$  and  $I_S$  are functions of the barrier strength and temperature. As follows from equations (2.7) and (2.8), the criterion for the observation of an anomalous  $I_S(\varphi)$ ,  $I_1=0$ , is realized, as an example, for an asymmetric  $45^\circ$  bicrystal junction, i.e., a junction with  $\theta_1 = 45^\circ$  and  $\theta_2 = 0$ . More generally, this condition is satisfied when the lobe of one of the electrode's order parameter face the node of the other. In this condition one expects double periodic  $I_s(\varphi)$  dependence. Extensive studies on the presence of 2<sup>nd</sup> harmonic in the CPR of  $45^\circ$  grain boundary junctions have been carried out by Il'ichev and co-workers [45]. Before describing the main consequences of such dependence, it is worth remembering that, for many grain boundaries layouts, the properties are strongly influenced by the effect of faceting of the junction boundary, as we discussed in the previous paragraph. We emphasize that, within the  $d$ -wave scenario, faceting has a more significant influence on the electronic properties of boundaries with a misorientation close to  $45^\circ$  than on boundaries with smaller misorientation angles. Grain-boundary junctions, fabricated on bicrystal substrates with misorientation angle of  $45^\circ$ , contain a higher density of facets, therefore the supercurrent density  $J_S$  is a random alternating function in the plane of the contact (see Figure 2.11). These microstructural issues are an obstacle to the observation of 2<sup>nd</sup> harmonic effects. Therefore,

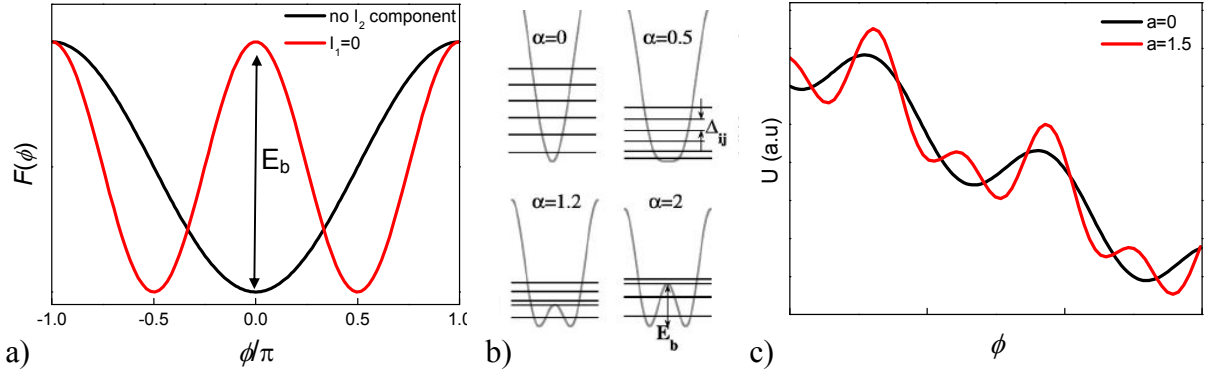


Figure 2.13 Effect of the second harmonic of the current phase relation on the free energy of a junction (a) and on the washboard potential for a fixed bias (c). In inset (b) the change of the energy barrier  $E_b$  is showed for different values of the ratio  $a=I_2/I_1$ .

grain boundary junctions showing less influence on the microstructure on their properties are, again, favoured when dealing with the study of the 2<sup>nd</sup> harmonic in the CPR.

The free energy of the junction, when taking into account the current-phase relation (2.7) can be written as:

$$F = -\left(\frac{\Phi_0}{2\pi c}\right)\left(I_1 \cos \phi + \frac{I_2}{2} \cos 2\phi\right) \quad (2.9)$$

In Figure 2.13 the two limit cases of CPR with only the  $I_1$  component or only the  $I_2$  component are plotted. For a current phase relation with a pure double periodicity (as the 45° bicrystal junction mentioned) the free energy has a degenerate ground state with minima occurring at finite values of the phase (a similar condition was described for a ring containing a  $\pi$  junction in applied magnetic field in section 2.3.3). The plot in Figure 2.13a can also be read as two potential wells divided by a barrier whose height  $E_b$  depends from the relative amount of  $I_1$  and  $I_2$ ; it is zero in the first case and maximum in the second. The developing of the barrier  $E_b$  changes also the distribution of the energy levels inside the wells. It is therefore important to study what happens for intermediate values of the ration  $I_2/I_1$ . Tzalenchuck et al. [46] calculated the evolving of the energy levels inside the potential well for different values of the parameter  $a=I_2/I_1$  (Figure 2.13b). From their calculations it is possible to see that already above  $a=0.5$  the potential becomes bistable. Increasing the  $I_2$  component and the parameter  $a$ , the barrier height  $E_b$  increases, so does the spacing between the ground state and the higher excited levels. This makes the junction a quasi-two level system, since the transitions to the higher levels are suppressed. Indeed, for  $a$  in the range 1.2–1.7 the splitting between the first and second levels (100 mK) is almost two orders of magnitude less than the splitting with the third level (>3 K). They can therefore be considered well decoupled if the operation temperature is set in the sub-Kelvin range. This shows how, in the correct configuration, a single Josephson junction could act as a quantum device through the manipulation of its state across the energy levels. The main obstacle to such goal is the presence of quasi particles due to the nodes of the order parameter. The same symmetry allowing the presence of the second harmonic is, indeed, also the main obstacle to its use. In HTS materials, the order parameter, therefore the superconducting gap, goes to zero in correspondence of the four nodes. In these points, excitation of single electrons, which are of course not coherent and source of noise, becomes possible. Moreover, as we described in the

previous paragraph, the transport in many GB structures is not directional: it takes place through a cone more than in a single direction, therefore the nominal orientation of the junction will not be preserved during the transport. These decoherence factors brought the scientific community to deny for many years the possibility that macroscopic quantum effects, although theoretically possible, could actually take place in HTS structures. Advance in fabrication techniques as well as in the understanding of HTS phenomenology, instead, brought only two years ago to the first proof of macroscopic quantum behaviour in a grain boundary biepitaxial junction. For the first time, the energy level quantization described in this paragraph was proved together with the possibility to induce the excitation from one level to the other using microwaves [47, 48].

The presence of a second harmonic in the CPR influences also the dynamic of the junction. As described in section 1.3.3, the dynamic of a Josephson junction can be analysed resorting to the washboard model described by equation (1.11). In the presence of both first and second harmonic, the washboard potential can be written as follows:

$$U(a, \varphi) = - \left( \frac{I_1 \Phi_0}{2\pi} \right) \left( \frac{I_C}{I_1} \gamma \varphi + \cos \varphi - \frac{a}{2} \cos 2\varphi \right) \quad (2.10)$$

where  $a$  is the ratio between the second and the first harmonic of the current phase relation,  $I_C = I_1 \max_{\varphi} \{ \sin \varphi - a \sin 2\varphi \}$  is the maximum critical current of the junction and  $\gamma = I / I_C$  is the normalized bias and determines the tilt of the washboard potential. In Figure 2.13b the equation (2.10) is plotted for a fixed bias and  $a=1.5$ . For a fixed critical current  $I_C$ , the second harmonic, compared to the case of a pure  $\sin \varphi$ , reduces the barrier height and increases the frequency at which the phase oscillates inside the well. Consequently, the escape rates in the thermal and quantum regimes are larger for  $a>0$  rather than for  $a=0$ . In other words, the presence of the second harmonic enhances the probability for macroscopic quantum tunnelling [47].

One of the easiest ways to check for the presence of a 2<sup>nd</sup> harmonic component is to analyze the  $I_C(H)$  pattern of the junction. When the current-phase relation (2.7) is inserted in the general equation (1.6) for the dependence of the critical current on the magnetic field, one can simulate the effect of different values of the  $a=I_2/I_1$  ratio on the shape of the magnetic pattern. Figure 2.14 shows some examples of such simulations. For a dominant 2<sup>nd</sup> harmonic component, the periodicity of the pattern is doubled. When both 1<sup>st</sup> and 2<sup>nd</sup> harmonics are present, with a sufficiently high  $a$  ratio, bumps appear at the side of the main lobe and dips in the secondary lobes. Given the importance of the 2<sup>nd</sup> harmonic for the quantum application of HTS junctions, one of the aim of this work has been also to realize junctions where it is possible to identify such a component. The results obtained will be shown in chapter 6.

The observation of MQT in a biepitaxial junction [48] has been the first proof of macroscopic quantum behaviour of an HTS device. It demonstrates that it is possible to design a device where the disrupting effects of the disorder at the junction's interface, the complexity of the materials and the presence of nodes in the order parameter, generating quasi particles, are limited. In this respect, advances in the realization techniques of HTS devices are of the utmost importance.

In the next paragraph, we will summarize the most important features needed for the application of HTS junctions to quantum electronics.

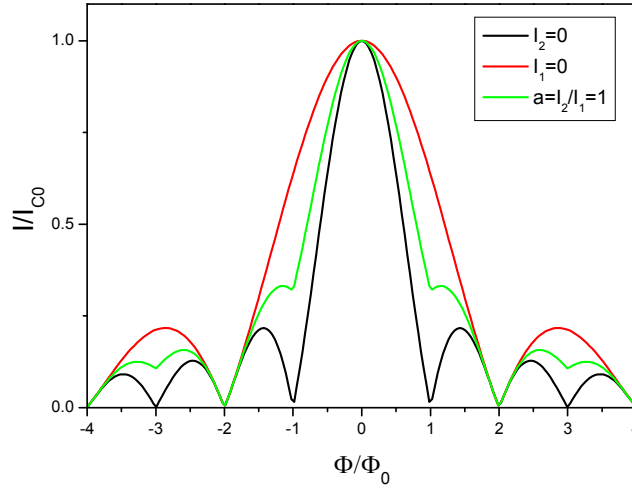


Figure 2.14 Effects on the 2<sup>nd</sup> harmonic in the current-phase relation on the magnetic pattern. The black curve is the Fraunhofer-like pattern for the pure  $\sin\phi$  dependence, the red curve refers to a pure 2<sup>nd</sup> harmonic CPR and the green curve to a CPR with a ratio  $a=1$

## 2.4. Grain boundary junctions in superconducting electronic applications

In this chapter the main features of HTS GB Josephson junctions were described. The  $d$ -wave order parameter symmetry gives unique properties to HTS junctions, which do not have any analogy with systems based on conventional superconductors [10].

Even if the HTS structures are not optimal, compared with low critical temperature superconductor Josephson junctions, the state of the art allows the realization of weak links with unexpectedly high quality and quantum properties, which open interesting perspectives for the future. One of the most appealing is the “quiet qubit” proposal exploiting HTS junction circuits with an energy–phase relation with two minima at  $\pm\Phi_0/2$ . This self generated field could be used to replace the constant magnetic external bias need for the qubit operation, removing a source of noise and decoherence [49,50,51, 52, 53]. Two of the possible configurations for such devices are sketched in Figure 2.15. One possibility is offered by a S–D–S’ structure with the  $d$ -wave electrode misoriented by  $45^\circ$  [49] (Figure 2.15a); in another, “all HTS” configuration, two  $45^\circ$  asymmetric GB junctions could form a phase qubit whose operating point is stable and protected by external field fluctuations [54].

Recently, the spontaneous generation of a fractional magnetic flux quanta in a  $\pi$ -ring was exploited in a logic circuit, a flip-flop, in which the fractional flux polarity is controllably toggled by applying single flux quantum pulses at the input channel [55]. The integration of  $\pi$  rings into conventional rapid single flux quantum (RSFQ) logic as natural two-state devices brings many advantages. A complication in standard RSFQ is that superconducting ring structures have one lowest energy state, i.e., the zero-flux state, and a degenerate first-order state with a flux of  $\pm\Phi_0$ . To reach an operating point with a twofold degenerate lowest energy state, a bias current must be asymmetrically injected, requiring additional bias lines and control over these currents. In principle, the flip-flop device could be designed to work also without this current, provided an even higher asymmetry in the critical currents of the junctions. This asymmetry imposes strict margins on the design parameters, such as the junction critical currents and the inductance values. These factors have until now strongly hampered the development of large-scale RSFQ logic circuits.

The spontaneous generation of fractional flux in the  $\pi$ -shift device eliminates the need for

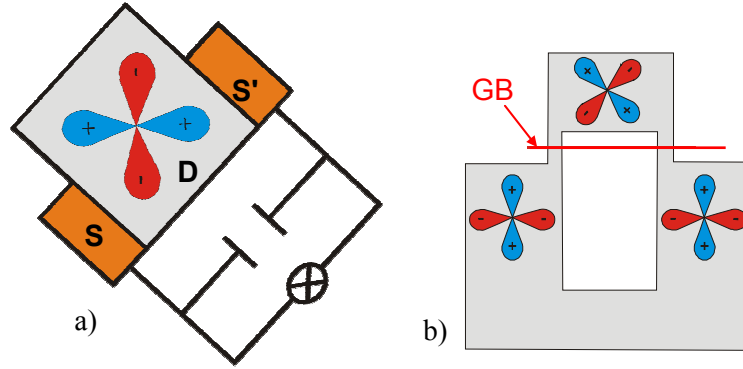


Figure 2.15 Two proposal for implementation of HTS junctions to quantum electronics, taking advantage of the degenerate ground state arising in particular junctions' configurations: (a) S-D-S' structure involving both conventional and d-wave superconductors proposed by Ioffe *et al.* [49] and (b) 45° asymmetric SQUID proposed by Amin *et al.* [54]

the asymmetrically injected bias current, which reduces the amount of connections to external control electronics and allows for symmetry in the design parameters, with great benefit in the design process and fabrication. The devices described in Ref. [55] were realized using the artificial barrier technology described in section 2.1, involving high-T<sub>c</sub> and low-T<sub>c</sub> superconductors.

Some optimism in the possibility of exploiting the intrinsic bistable properties of HTS for quantum circuitry is encouraged also by a series of recent results, in which current versus the superconducting phase ( $I_c(\varphi)$ ) measurements on bicrystal grain boundary junctions, especially in 45° configurations, have reported the prevalence of the 2<sup>nd</sup> harmonic component in the CPR under some conditions [45].

There are, however, many concerns about the quietness of these devices. While on the one hand a 45° misorientation of the order parameter in one electrode is necessary to generate the  $\pi$ -behaviour and the double degenerate ground state, the zero energy gap in these same directions may lead to spontaneous currents which may cause additional noise and decoherence mechanisms. Nevertheless, it has also been argued that problems in observing quantum effects due to the presence of gapless quasi-particle excitations could be overcome by choosing the proper working phase point. In particular, decoherence mechanisms can be reduced by selecting appropriate transport directions because of the strong phase dependence of the quasi-particle conductance in a *d*-wave GB junction. Additional concerns are also connected to structural properties: what is common to most HTS junctions is that the intrinsic features we described are combined with the influence of the microstructure in determining the junction properties.

A promising route to further improve the quality of the junctions is the realization of smaller junctions. Submicron HTS junctions have already been used to reduce decoherence [46] and observe the  $2\varphi$  component [45]. They could prove to be more uniform and of better quality for applications. Measurements on such structures could also provide feedback to improve GB junctions and to clarify the transport mechanisms of GB barriers.

To summarize, the main fundamental characteristics needed for the application of an

HTS junctions design to superconducting electronics and quantum systems can be listed as follows:

- Possibility to isolate and exploit intrinsic  $d$ -wave induced effects over extrinsic effects artifacts
- Possibility to isolate and exploit the  $2\phi$  component in the current-phase relation
- Reproducible and controllable junctions' properties (low spread in the junctions' parameters)
- Tuning of the critical current  $I_C$  and the normal state resistance  $R_N$  in order to adapt to the experiment or the application's requirements
- Possibility to realize both underdamped and overdamped junctions

Besides these basic issues, some technological features are needed as well:

- Flexibility in the junctions' structure, in particular in order adapt the materials to the experimental and electronic integration requirements
- Higher control of the GB microstructure
- Stability of the properties with time

The biepitaxial junctions we studied during this work have most of these requisites and are also suitable for further advance from the technological point of view.

It was demonstrated that the GB barrier in these structures is characterized by a lower transmissivity, if compared to other HTS junctions' structures. The reason for this characteristic is to be found probably in the off-axis electrode (see Figure 2.3c), implying that the transport has to take place in part along the  $c$  axis. The result is the possibility to have underdamped behaviour (see Figure 1.5b and Figure 1.7b). It was also showed that in these junctions the effects of the barrier microstructure on the transport are less influential, the behaviour of the  $J_C$  versus the misalignment angle of the junctions, as an example, was proved to be determined only by the order parameter symmetry (see Figure 2.5c). Finally, in these junctions macroscopic quantum effects and energy level quantization were demonstrated for the first time for HTS devices [30, 31].

Biepitaxial junctions could also offer the advantages of an "all HTS" design for superconducting electronics, when compared to the devices used for example, for the flip-flop circuit realization described in [55].



### **3. *Biepitaxial junctions experimental techniques: thin films deposition and characterization***

This chapter is meant to describe the improvements aimed to a better control of the biepitaxial junctions structure. We improved the control of all the fabrication steps, in particular the deposition of thin films, a fundamental issue for high quality junctions. Nanotechnology techniques were also used for the first time for the realization of sub-micron biepitaxial junctions, also with the aim of approaching novel transport regimes and obtain information on the microscopic mechanisms of GB and, more general, on HTS transport.

In this and the following chapter the issues concerning the realization of the biepitaxial junctions will be described. There are two fundamental steps in the realization of GB devices: the deposition of thin films and the patterning of them. Special attention is paid to these aspects because of their technological impact, which is in the spirit of the TIMSI PhD program. In this chapter we will deal with the first issue, leaving a detailed explanation of the second to the next chapter.

#### **3.1. *Biepitaxial junctions' structure and fabrication procedure***

In biepitaxial junctions, the two different crystalline orientations of the YBCO film needed to obtain the grain boundary are induced using a structured substrate. The template for the growth is defined with a patterned seed layer, inducing a growth with an orientation different from the one induced by the substrate.

The fabrication procedure of the biepitaxial junctions realized in this work can be roughly sketched out as follows (the letters refer to the panels in Figure 3.1):

a. Deposition of the seed layer thin film.

RF magnetron sputtering and pulsed laser deposition (PLD) were used for this step. Great care has to be used in seed layer growth optimization, since the quality (the smoothness and the uniformity) of the seed layer film is very important for the subsequent growth of the HTS film.

b. Patterning of the seed layer.

This step can be divided in three stages:

- realization of a “positive” mask intended to protect part of the seed layer area
- removal of the seed layer area not protected by the mask via ion milling
- removal of the mask

The mask realization technique determines the minimum dimension of the structure that will be realized and the sharpness of the edges. During this work photolithography and electron-beam lithography were used.

c. Deposition of the YBCO film and of a protective layer of gold.

Again, two different techniques were used: inverted cylindrical magnetron sputtering and PLD. The layer of gold deposited soon after the YBCO film, either by sputtering or by thermal evaporation, is needed to protect the superconductor from coming into contact with chemicals used in the following steps and also to realize, during the last step of the fabrication, the electrical contacts for the transport measurements.

d. Patterning of the YBCO film

The procedure for the patterning of the YBCO film is similar to the one for the seed layer.



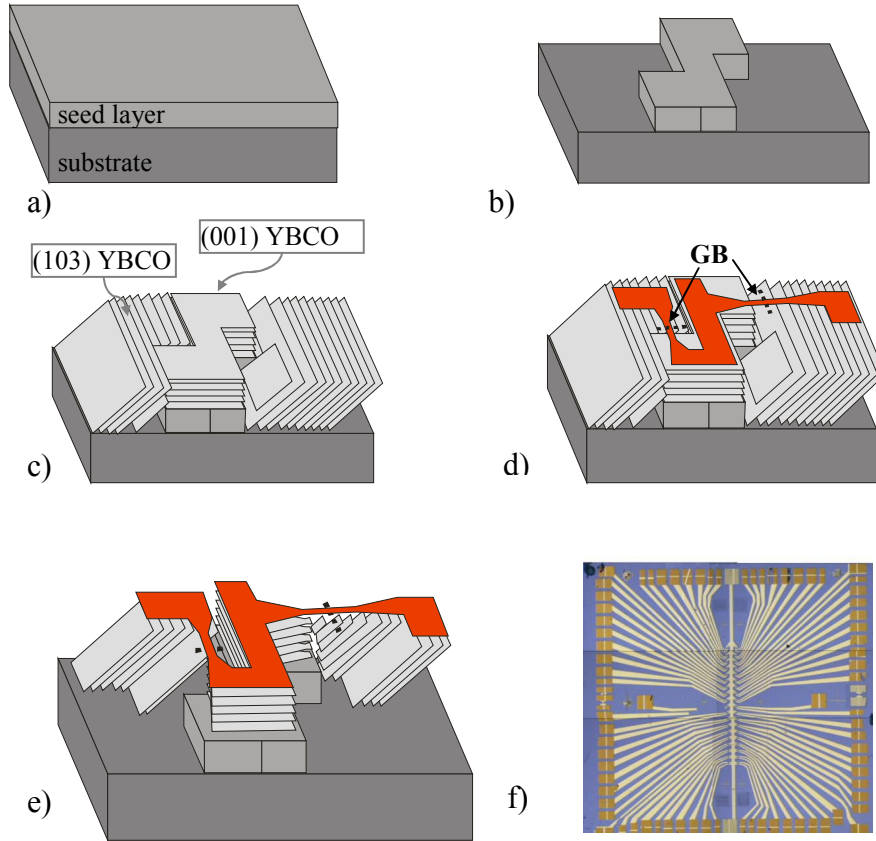


Figure 3.1 Fabrication steps of the biepitaxial junctions: a) deposition and b) patterning of the  $\text{CeO}_2$  seed layer; c) deposition of YBCO thin film; d) and e) patterning of the YBCO film. Panel f) shows an optical microscope image of one of the samples realized during this work.

However, due to the higher structural complexity of the material and to the sensitivity to oxygen loss, greater care has to be taken during the patterning steps involving high temperature, as for example the curing of the resist, or ion milling, during which heat can be generated due to impact with energetic ions.

As a last step, gold pads are defined using photolithography and ion milling. They will be used for the connection to the measuring units.

Among the main characteristics of these junctions there is, as pointed out in the previous chapter, the off axis electrode obtained thanks to the (103) orientation of the YBCO film grown on the (110) oriented substrate. This feature most likely determines the lower barrier transmissivity that characterizes the transport properties of these devices.

Another feature of great interest both for the studies of fundamental physics and for future applications is the possibility to realize junctions with different misorientation angles on the same chip. The misorientation angle  $\theta$  in these structures is defined as the angle between the normal to the GB plane and the [001] direction of the substrate. In Figure 3.2 three possible orientations are sketched, with  $\theta = 0^\circ$ ,  $90^\circ$  and  $45^\circ$ . The two extreme cases,  $\theta = 0^\circ$  and  $90^\circ$  correspond to a [100]  $45^\circ$  tilt and a [100]  $45^\circ$  twist GB respectively (the definition of tilt and twist were given in chapter 2); intermediate angles correspond to a mix of tilt and twist. The different misorientation angles are obtained changing the patterning geometry of the seed layer; in this way all the desired misorientation angles can be realized and, most interesting, on the same chip. The chips realized during this work, as an example, contain 76 junctions, divided in groups of four per each angle going from  $0^\circ$  to  $90^\circ$  in  $5^\circ$  steps (Figure 3.1f). The transport properties of biepitaxial junctions are influenced by the asymmetry of the order parameter, therefore it is possible to realize on the same chip junctions where this effect

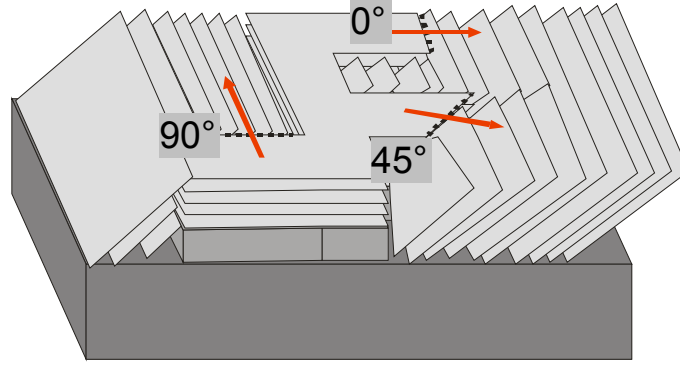


Figure 3.2 Realization of different misorientation angles  $\theta$  in a biepitaxial GB junction. Three angles are showed:  $\theta=0^\circ$ ,  $45^\circ$  and  $90^\circ$

is taken advantage of in different ways. As an example, it is possible to carry out a homogeneous study of the effects of  $d$ -wave symmetry on a given property of the devices, on a single chip. It is also a great plus in electronic applications and for the study of fundamental aspects of HTS physics. It is worth noting that the biepitaxial technique is the only technique for the realization of HTS GB junctions among the currently available ones, allowing the realization of junctions with different misorientation angles on the same chip; in the case of bicrystal and step edge technique, the GB angle has to be the same for all the devices on the chip.

Furthermore, the use of  $\text{CeO}_2$  as a seed layer allows a better exploitation of the  $d$ -wave symmetry of the order parameter. The first generation of biepitaxial junctions realized in Naples used a (110) oriented  $\text{MgO}$  film as a seed layer. The epitaxial relations between the lattice parameters determine a (001) growth of the YBCO on (110) oriented  $\text{MgO}$ . When, on the other hand,  $\text{CeO}_2$  is used, the (001) oriented YBCO cells undergo a  $45^\circ$  in plane rotation. This further rotation adds to the tilt and twist, leading to the following misorientation:

$$\begin{aligned} &[001] \ 45^\circ \text{ tilt} + [100] \ 45^\circ \text{ tilt for } \theta = 0^\circ \\ &[001] \ 45^\circ \text{ tilt} + [100] \ 45^\circ \text{ twist for } \theta = 90^\circ \end{aligned}$$

The additional  $45^\circ$  tilt around the  $c$ -axis induced using  $\text{CeO}_2$  enhances the effects of the  $d$ -wave symmetry of the order parameter, as is sketched in Figure 3.3. Moreover, in the presence of faceting, a characteristic commonly present in GBs, could give rise to  $\pi$  loops.

A further degree of freedom offered by the biepitaxial technique is in the choice of the substrate material. The most common substrate for HTS devices is the strontium titanate  $\text{SrTiO}_3$  (STO). It has optimal chemical compatibility with YBCO and its structure is stable at the high temperatures used for the realization of YBCO films. Most important, the lattice parameters of STO and YBCO have a low misfit. It is important to choose materials with similar lattice parameters when realizing such complex structure, since the stress deriving from the need to adapt the lattice of the film to the substrate's one can result in the deformation of the HTS elementary cell, the creation of cracks, dislocations and impurities. On the other hand, STO gives some problems in the case of experiments in presence of microwaves. One important example is represented by the energy level quantization experiment described in Ref. [31]. Here, the microwaves used to induce the transition from one energetic level to the other are coupled to the junction through the substrate. It was shown that the coupling was strongly frequency dependent, indeed for frequencies larger than 4 GHz, no microwaves could be coupled. The reason was found in the high dielectric constant of the STO substrate. Moreover, the STO substrate acts as a dielectric resonator: microwaves that do not match the resonance condition of the STO substrate will be reflected to a large extent. These influences from the substrate add to the intrinsic complexity of the biepitaxial structure,

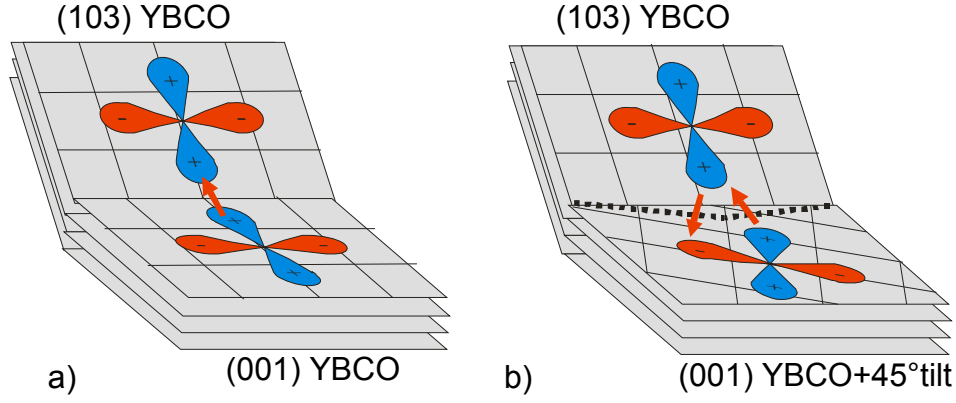


Figure 3.3 Comparison between the tilt GB structure ( $\theta = 0^\circ$ ) obtained using MgO (a) and  $\text{CeO}_2$  (b) as a seed layer. In the latter case, a  $45^\circ$  in plane rotation is added with the consequence of possible formation of  $\pi$  loops

making it more complicated to model the junctions' behaviour, as for example was showed in Ref. [56].

To overcome this problem, during this work we tried to extend the junctions' fabrication procedure to another substrate material: lanthanum aluminate  $\text{LaAlO}_3$  (LAO). The advantages given by the use of LAO for microwave applications are due to its lower dielectric constant ( $\epsilon_r \approx 23$ , compared with  $\epsilon_r \approx 330$  for STO) and lower loss tangent ( $3 \times 10^{-5}$  at 77K, compared with  $6 \times 10^{-2}$  for STO) [57, 58]. On the other hand, the use of LAO raises problems during the junctions fabrication, due to its fragility and to the presence of many twin boundaries. The high temperature needed for the YBCO deposition process promotes their motion, with the consequence of introducing strain, defects and possibly cracks in the YBCO film. Despite these problems, we succeeded in realizing good quality junctions using LAO substrates, as will be described later in this work.

To summarize, the biepitaxial technique used during this work offers a good number of degrees of freedom thanks to the possibility to:

- change the misorientation angle of the junctions on the same chip
- realize both 0 and  $\pi$  junctions with the use of different seed layers materials
- choose the type of substrates depending on the different experiments or applications

The main properties of the materials used for the realization of biepitaxial junctions are listed in Table 3-1.

This chapter focuses on the thin films deposition steps of the biepitaxial junctions' realization procedure outlined at the beginning of the paragraph. The deposition techniques used and the results obtained will be described. Therefore, before going into the details of the realization techniques, it is worth giving some description of the tools used during this work for the determination of the structural quality of the realized films.

### 3.2. Techniques for the structural characterization of thin films

The performances of GB junctions rely on a great extent on the structural properties of the thin films used for their realization. This is even more important in the case of biepitaxial junctions, having a rather complex structure.

The structural aspects we have been concerned of during this work are:

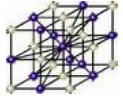
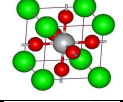
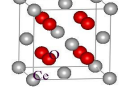
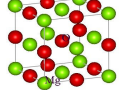
material	crystal cell	lattice parameter (nm)	dielectric constant	$\tan \delta$
LaAlO <sub>3</sub>		0.382	23	$3 \cdot 10^{-5}$
SrTiO <sub>3</sub>		0.391	330 @300K	$6 \cdot 10^{-2}$
CeO <sub>2</sub>		0.541	17	
MgO		0.421	9.6	$5 \cdot 10^{-4}$

Table 3-1 Main properties of the materials that can be used in the realization of biepitaxial junctions. during this work, STO and LAO were used as substrate and CeO<sub>2</sub> as seed layer.

- The crystal orientation of the films
- The absence of spurious phases
- The absence of precipitates
- The smoothness and uniformity of the films

The technique used to investigate the first two issues is x-ray diffractometry, allowing a precise determination of the crystalline orientation of the film and, eventually, the presence of second phases with a different orientation. For the films surfaces quality, atomic force microscopy was widely employed. Some analyses were also carried out with scanning electron microscopy, in collaboration with the Second University of Naples.

### 3.2.1. X-Ray diffraction

X-ray diffraction (XRD) is a powerful technique used to uniquely identify the crystalline orientations and phases present in materials and to measure some structural properties of crystalline films such as strain state, grain size, epitaxy, preferred orientation, and defect structure. XRD can also be used to determine the thickness of thin films and multilayers. Besides offering high accuracy in the measurement of atomic spacing, XRD is also a noncontact and non-destructive technique.

Crystalline materials consist of atomic planes, each characterized by a different  $d$  spacing. If  $a$ ,  $b$ , and  $c$  are unit vectors corresponding to the edges of the unit cell, any atomic plane can be uniquely distinguished by its Miller indices that are the three reciprocal intercepts of the plane with the  $a$ -,  $b$ -, and  $c$ -axes and are reduced to the smallest integers having the same ratio. Thus, an  $(hkl)$  plane intercepts the crystallographic axes at  $a/h$ ,  $b/k$ , and  $c/l$ . The  $d$ -spacing between  $(hkl)$  planes, denoted  $d_{hkl}$ , will depend on the crystal structure and the lattice constants [59]. The materials involved in this work have either a cubic structure (STO, LAO, CeO<sub>2</sub>) or an orthorhombic one (YBCO); for these types of cells the value of  $d_{hkl}$  can be calculated with the following formulas:

$$\frac{1}{d_{hkl}^2} = \frac{1}{a^2} (h^2 + k^2 + l^2) \quad (\text{cubic cell})$$

$$\frac{1}{d_{hkl}^2} = \frac{h^2}{a^2} + \frac{k^2}{b^2} + \frac{l^2}{c^2} \quad (\text{orthorhombic cell})$$

where  $a, b, c$  are the lattice constant of the crystal.

When there is constructive interference from x-rays scattered by the atomic planes in a crystal (see inset in Figure 3.4), a diffraction peak is observed. The condition for constructive interference from planes with spacing  $d_{hkl}$  is given by Bragg's law:

$$n\lambda = 2d_{hkl} \sin \theta_{hkl}$$

where  $\lambda$  is the x-ray wavelength and  $\theta_{hkl}$  is the angle between the atomic planes and the incident (and diffracted) x-ray beam.

The most common layout for an x-ray diffractometer is the Bragg-Brentano geometry (Figure 3.4). The x-rays, usually generated by a Cu source with a wavelength  $\lambda=1.54\text{\AA}$ , are collimated by a series of slits, and then impinge on the specimen at an angle  $\omega$ . After passing through receiving slits, the diffracted x-rays are detected. In order to carry out a complete characterization of the sample's crystalline properties, the diffractometers have four degrees of freedom. They can be indicated with the following symbols, as shown in Figure 3.4:

- $2\theta$ : the angle between the impinging beam and the detector
- $\omega$ : the angle between the impinging beam and the sample surface
- $\varphi$ : the rotation of the sample around the normal to its surface
- $\psi$ : the rotation around the direction given by the intersection between the sample surface and the diffraction plane

X-ray analysis can be made in symmetric and asymmetric arrangements. In the first case, the sample has its surface positioned symmetrically with respect to the source and detector, the relation between  $\omega$  and  $2\theta$  is kept constant:  $\omega=2\theta/2$  and only the crystallographic planes that are parallel to the sample's surface will be analysed. In the second case, an additional rotation is given to the sample in order to bring family of plans non parallel to the surface in the Bragg's conditions.

During this work, both symmetric and asymmetric measurements have been carried out. In the following, a list of the measurements used is given:

- $\theta/2\theta$  diffraction pattern  
Is realized changing the values of  $\omega$  and  $2\theta$  keeping the relation:  $\omega=2\theta/2$ . When the angle  $2\theta$  reaches the values associated, through the Bragg's law, to a family of plans parallel to the sample surface, a peak in the diffraction pattern is generated. This is the main type of measurement to investigate the orientation of the crystalline film and, eventually, the presence of second phases grown with different orientations. It gives also qualitative information about the dimensions of coherent diffusion domains (from the width of the peaks) and the relative amount of phases with different orientations (from the ratio of the intensity of the peaks related).
- Rocking curve (or  $\omega$  scan)  
Is used to get information about a selected family of plans. It is realized keeping fixed the value of  $2\theta$  and changing  $\omega$  around the value corresponding to the family of plans considered. In the case of a perfect crystal, this measurement gives as a result a very

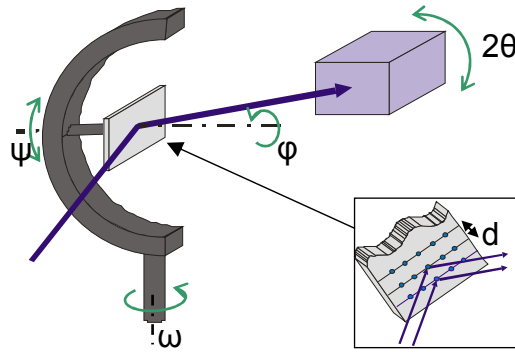


Figure 3.4 Sketch of the four degrees of freedom of a four circles goniometer for x-ray analysis

narrow peak, whose width is in principle related only to the angular resolution of the instrument. In the case of real films, not all the planes of the family will be perfectly aligned, and the width of the peak gives qualitative information about the degree of such misalignment.

- **Glancing incidence x-ray reflectivity**  
Is a measurement which can determine the thickness, roughness, and density of the film. Since their refractive index is less than 1, x-rays experience total external reflection at incidence angles less than a critical angle. By varying the incidence angle near this value, the penetration depth of the incident x-rays is varied. From the interference of the diffracted x-rays originated from different depths, the depth-dependent structure of the specimen may be obtained. During this work this technique was used to measure the thickness of the films deposited.
- **Texture measurement ( $\varphi$  scan)**  
This is an example of asymmetric measurement. It is realized considering a family of plans forming an angle  $\alpha$  with the surface of the sample, fixing the values of  $\omega$  and  $2\theta$  so that  $\omega = 2\theta/2 + \alpha$  and changing the value of  $\varphi$ . This measure is useful to check the alignment of the crystallographic axes of the film with respect to the substrate.
- **Asymmetric  $\theta/2\theta$**   
This measurement technique is similar to the  $\theta/2\theta$  diffraction pattern measurement described before, with the additional rotation of  $\alpha$  in order to investigate also a family of planes that are not parallel to the surface. It was often used during this work in order to distinguish between phases whose diffraction conditions in the symmetric arrangement are so close that could be discriminated using a conventional  $\theta/2\theta$  measure.

### 3.2.2. Atomic force microscopy

This technique was used during this work to study the uniformity and, more in general, the quality of the surfaces of the films and of the grain boundaries realized. It is also of great help in some steps of the patterning process to check for eventual damage of the surfaces.

In an Atomic Force Microscope (AFM), sketched in Figure 3.5, an atomically sharp tip is scanned over a surface. Feedback mechanisms enable the piezo-electric scanners guiding the tip to maintain this at a constant force above the sample surface to obtain height information. Tips are typically made from Si, in some cases coated with a metal like Pt, and extended down from the end of a reflective cantilever, upon which a diode laser is focused. As the tip scans the surface of the sample, moving up and down with the contour of the surface, the laser beam is deflected off the attached cantilever into a photodiode. The photodetector measures



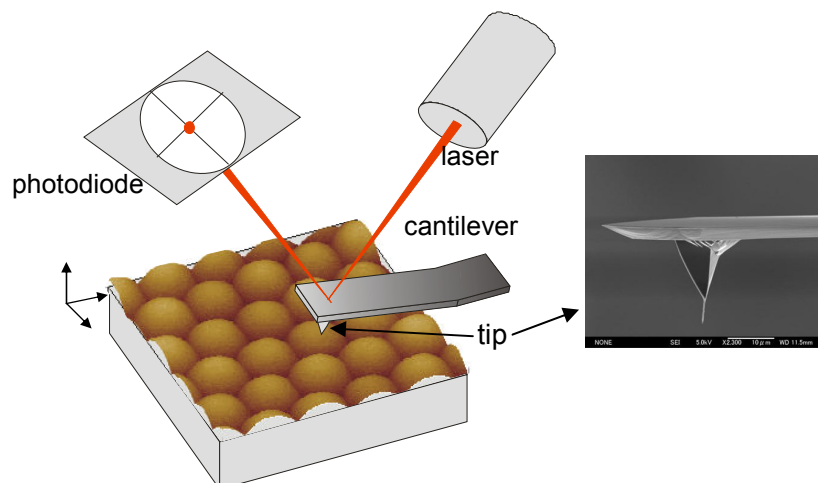


Figure 3.5 Sketch of the operation of an AFM: a laser is focused on a reflective cantilever where an atomically sharp tip is built in (inset). The changes in the height of the tip are recorded with a photodiode.

the difference in light intensities between the upper and lower panel, and converts it into a voltage signal. Feedbacks from the photodiode difference signal, through software control from a computer, are then sent to the piezo-electric transducers to adjust the tip height. Topographical maps of the sample surface are then constructed by plotting the local sample height versus horizontal probe tip position [59].

In atomic force microscopy, three techniques can be used: contact mode, non contact mode and tapping mode. The fastest and more flexible one is the tapping mode. It was developed as a method to achieve high resolution without inducing destructive frictional forces and allows topographic imaging of sample surfaces that are easily damaged or loosely hold to their substrate. Tapping mode imaging is implemented by oscillating the cantilever assembly at or near the cantilever's resonant frequency using a built in piezoelectric crystal. The piezo motion causes the cantilever to oscillate with high amplitude when the tip is not in contact with the surface. The oscillating tip is then moved toward the surface until it begins to lightly touch, or tap the surface. As the oscillating cantilever begins to intermittently contact the surface, the oscillation is necessarily reduced due to energy loss caused by the tip contacting the surface. The reduction in oscillation amplitude is used to identify and measure surface features. When the tip passes over a bump in the surface, as an example, the cantilever has less room to oscillate and the oscillation amplitude decreases. Conversely, when the tip passes over a depression, the cantilever has more room to oscillate and the amplitude increases (approaching the maximum free air amplitude). The digital feedback loop then adjusts the tip-sample separation to maintain constant amplitude and force on the sample.

### 3.2.3. Scanning electron microscopy

The Scanning Electron Microscope (SEM) is a widely employed thin film and coating characterization instrument. A schematic of the typical SEM is shown in Figure 3.6. Electrons thermionically emitted from a tungsten cathode filament are accelerated to an anode, focused by condenser lenses into a beam with a very fine spot size. Coils located at the objective lens deflect the beam allowing to scan the specimen surface either linearly or in raster fashion. Upon impinging on the specimen, the primary electrons decelerate and transfer energy inelastically to other atomic electrons and to the lattice. Through continuous random scattering events, the primary beam effectively spreads and fills a teardrop-shaped interaction

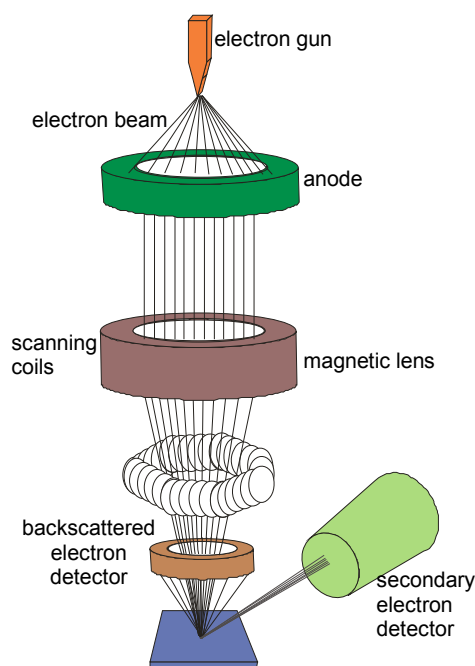


Figure 3.6 Sketch showing the main components of a scanning electron microscope

volume under the specimen surface with a multitude of electronic excitations. The result is a distribution of electrons that leave the specimen with an energy spectrum including secondary electrons, Auger electrons and elastic backscattered electrons. In addition, target X-rays are emitted, and other signals such as light, heat, and specimen current are produced, and the sources of their origin can be imaged with appropriate detectors.

The various SEM techniques are differentiated on the basis of what is subsequently detected and imaged. The most common imaging mode, and the one used during this work, relies on detection of the secondary electrons, the least energetic emitted species. Their very low energy means they originate from a subsurface depth of several angstroms. The signal is captured by a detector which is rastered in synchronism with the raster-scanned primary beam. Three-dimensional quality images can also be obtained from non planar surfaces: the contrast variation observed is due to the fact that sloping surfaces produce a greater secondary electron yield because the portion of the interaction volume projected on the emission region is larger than on a flat surface.

Using SEM it is possible to obtain detailed images of the sample's surface to identify the presence of precipitates, check the grain size and shape. Nevertheless, it is not possible to quantify the smoothness of the surface and SEM can be used only on conducting specimens.

### **3.3. Hints on the theory of films growth**

During this work different physical vapour deposition (PVD) techniques were used to realize the thin films constituting the biepitaxial devices. The object of PVD is to controllably transfer atoms from a vaporized source to a substrate where film formation and growth proceed. In this paragraph, the main theoretical ideas at the base of this rather complex phenomenon are given. It is useful to keep in mind, however, that so many factors are involved in the growth of thin films that it is almost impossible to take into account all of them. This is even more true in the case of growth of multicomponent films, such as YBCO,



where a number of different atomic species are involved. In these cases, the problem of thin films nucleation and growth has not been solved yet. The theories that will be described in the following pages offer a guideline to the problem; they can be useful, in particular, to highlight the qualitative effects of deposition parameters such as substrate temperature and ambient gas pressure, on the structure of the films.

### 3.3.1. Nucleation and growth

The formation of thin films takes place through different steps: during the early stages of the process atomic clusters nucleate, they eventually coalesce with each other and grow until covering the substrate. The grain structure that ultimately develops in a given deposition process is usually strongly influenced by what happens during these early steps of film nucleation and growth.

Soon after exposure of the substrate to the vapour in which the species to be deposited are dispersed, a uniform distribution of small but highly mobile clusters or islands is observed. The next stage involves merging of the islands by a coalescence phenomenon that is liquid like in character especially at high substrate temperatures. Coalescence decreases the island density, resulting in local denuding of the substrate where further nucleation can then occur. Coalescence continues until a connected network with unfilled channels in between develops. With further deposition, the channels fill in and shrink, leaving isolated voids behind. Eventually even the voids fill in completely, and the film is said to be continuous. This collective set of events occurs during the early stages of deposition, typically accounting for the first few hundred angstroms of film thickness.

Three basic growth modes have been observed: (1) island (or Volmer-Weber), (2) layer (or Frank-van der Merwe), and (3) Stranski-Krastanov [60]. Island growth occurs when the smallest stable clusters nucleate on the substrate and grow in three dimensions to form islands. This happens when atoms or molecules in the deposit are more strongly bound to each other than to the substrate. The opposite characteristics are displayed during layer growth. Here the nucleus expands in two dimensions resulting in the formation of planar sheets. In this growth mode the atoms are more strongly bound to the substrate than to each other. The layer plus island or Stranski-Krastanov (S.K.) growth mechanism is an intermediate combination of the two previous modes. In this case, after forming one or more monolayer, subsequent layer growth becomes unfavourable and islands form. The transition from two- to three-dimensional growth is not completely understood, but any factor that disturbs the monotonic decrease in binding energy characteristic of layer growth may be the cause. For example, due to film-substrate lattice mismatch, strain energy accumulates in the growing film. When released, the high energy at the deposit-intermediate layer interface may trigger island formation. This growth mode is fairly common.

### Nucleation

Film-forming atoms or molecules in the vapour phase are assumed to impinge on the substrate, creating aggregates that either tends to grow in size or disintegrate into smaller entities through dissociation processes. The free-energy change accompanying the formation of an aggregate of mean dimension  $r$  is given by

$$\Delta G = a_3 r^3 \Delta G_v + a_1 r^2 \gamma_{vf} + a_2 r^2 \gamma_{fs} - a_2 r^2 \gamma_{sv} \quad (3.1)$$

The chemical free-energy change per unit volume,  $\Delta G_v$ , drives the condensation reaction. Nucleation is possible only when the gas-phase supersaturation generates a negative  $\Delta G_v$ . The parameters  $\gamma$  indicate the interfacial tensions, the subscripts  $f$ ,  $s$ , and  $v$  representing film,

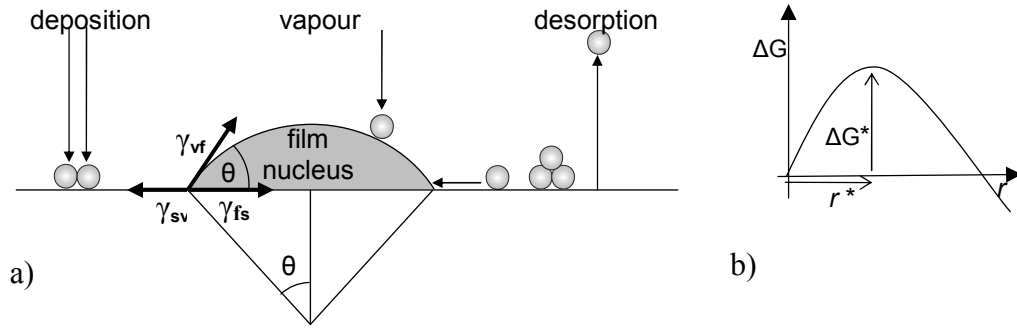


Figure 3.7 Schematic of basic processes on substrate surface during physical vapour deposition (a) and free energy change  $\Delta G$  as a function of clusters size  $r$ .

substrate, and vapour, respectively (Figure 3.7), and  $a_1$ ,  $a_2$  and  $a_3$  are geometrical factors related to the nucleus shape. Considerations of the mechanical equilibrium among the interfacial tensions yields Young's equation

$$\gamma_{sv} = \gamma_{fs} + \gamma_{vf} \cos \theta \quad (3.2)$$

Therefore, the contact angle  $\theta$  depends only on the surface properties of the involved materials. The three modes of film growth described in the previous section can be distinguished on the basis of equation (3.2): For island growth,  $\theta > 0$ , and therefore  $\gamma_{sv} < \gamma_{fs} + \gamma_{vf}$ . For layer growth the deposit "wets" the substrate,  $\theta = 0$  and  $\gamma_{sv} = \gamma_{fs} + \gamma_{vf}$ . Lastly, for S.K. growth,  $\gamma_{sv} > \gamma_{fs} + \gamma_{vf}$ .

Returning to equation (3.1), it is possible to define a critical nucleus size  $r^*$  given by the condition  $d\Delta G/dr = 0$ . An aggregate smaller in size than  $r^*$  disappears by shrinking, lowering  $\Delta G$  in the process. Critical nuclei grow to supercritical dimensions by further addition of atoms, a process that similarly lowers  $\Delta G$ . Correspondingly, the free energy evaluated at  $r = r^*$ ,  $\Delta G^*$ , represents the energy barrier for the formation of a stable nucleus (see Figure 3.7b).

This formalism provides a generalized framework for inclusion of other energy contributions. If, for example, the film nucleus is elastically strained due to the mismatch between film and substrate, then a term  $a_3 r^3 \Delta G_s$ , where  $\Delta G_s$  is the strain energy per unit volume, should be added. It brings an overall increase in the energy barrier  $\Delta G^*$ . Substrate charge and impurities similarly influence  $\Delta G^*$  by affecting terms related to both surface and volume electrostatic, chemical, etc., energies.

Substrate temperature and deposition rate are among the chief variables affecting deposition processes. A higher substrate temperature leads to:

- an increase in the size of the critical nucleus
- a discontinuous island structure is predicted to persist to a higher average coverage
- increase in the number of supercritical nuclei; thus, a continuous film will take longer to develop at higher substrate temperatures.

Increasing the deposition rate results in:

- smaller islands
- $\Delta G^*$  is also reduced, therefore nuclei form at a higher rate, suggesting that a continuous film is produced at lower average film thickness.

In the view of junctions applications, large crystallites or even monocrystal formation would be preferred. This is associated with a large  $r^*$  and  $\Delta G^*$ , equivalent to high substrate temperatures and low deposition rates. Alternatively, low substrate temperatures and high deposition rates yield polycrystalline deposits. While it is easy to independently tune the substrate temperature, the deposition rate is mainly determined by the dynamics of deposition technique. The two deposition methods used during this work, magnetron sputtering and pulsed laser deposition, are indeed characterized by different deposition rates. This is an important information in order to understand the different structural properties of the films deposited during this work, as will be shown in section 3.4.

### **Clusters coalescence**

The results of the kinetic theories of nucleation indicate that, in the initial stages of growth the density of stable nuclei increases with time up to some maximum level before decreasing. The coalescence processes that are operative beyond the cluster saturation regime are characterized by the following features:

- Decrease in the total projected area of nuclei on the substrate
- Increase in the height of the surviving clusters
- Nuclei with well-defined crystallographic facets become rounded.
- The composite island generally reassumes a crystallographic shape with time.
- When two islands of very different orientation coalesce, the final compound cluster assumes the crystallographic orientation of the larger island.
- The coalescence process frequently appears to be liquid like in nature with islands merging and undergoing shape changes after the fashion of liquid droplet motion.
- Prior to impact and union, clusters have been observed to migrate over the substrate surface in a process described as cluster-mobility coalescence.

Several mass-transport mechanisms have been proposed to account for these coalescence phenomena, such as sintering, cluster migration and ripening, i.e. growth of the larger clusters at the expense of the smaller ones.

#### **3.3.2. Expitaxial thin films and structural defects**

Epitaxy refers to extended single-crystal film formation on top of a crystalline substrate. Two types of epitaxy can be distinguished: *homoepitaxy* refers to the case where the film and substrate are the same material, whereas *heteroepitaxy* refers to films and substrates of different materials, and is of course a more common phenomenon.

In heteroepitaxy the lattice parameters are necessarily unmatched, therefore either edge dislocation defects form at the interface, or the two lattices strain to accommodate their crystallographic differences.

An important quantity that characterizes epitaxy is the lattice misfit  $f$  of the film related to the substrate, defined as

$$f = (a_0(s) - a_0(f)) / a_0(f) = \Delta a_0 / a_0 \quad (3.3)$$

where  $a_0(f)$  and  $a_0(s)$  refer to the unstrained lattice parameters of film and substrate, respectively. A positive  $f$  implies that the initial layers of the epitaxial film will be stretched in tension, and a negative  $f$  means film compression. Later in this chapter the lattice relations for the materials used during this work and the derived misfit will be presented.

The basic theory that accounts for the changes taking place during the formation of an epitaxial film was introduced by Frank and van der Merwe [61]. The theory predicts that any

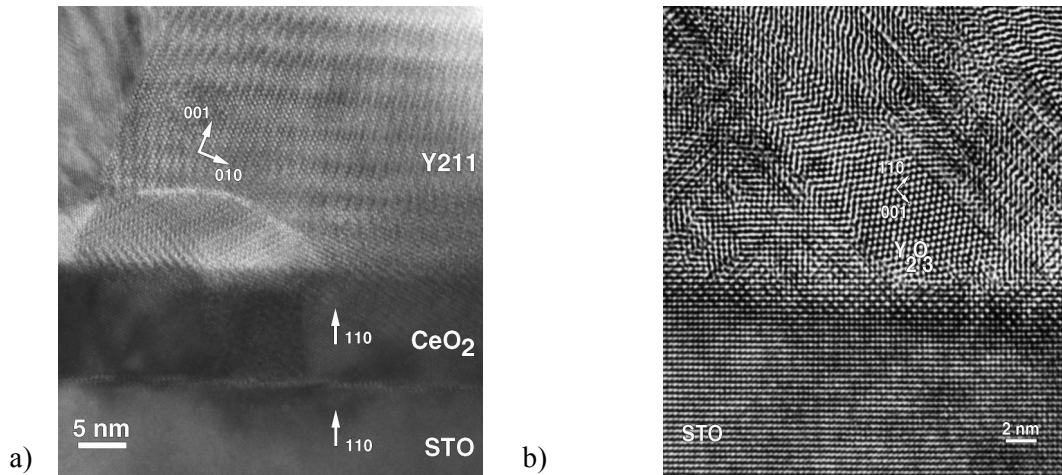


Figure 3.8 Transmission electron microscope (TEM) images highlighting the presence of Y211 and  $\text{Y}_2\text{O}_3$  phases in biepitaxial structures.

epitaxial layer having a lattice parameter mismatch with the substrate of less than  $\sim 9\%$ , as in our case, would grow pseudomorphically. At the beginning, the deposit would be elastically strained to have the same interatomic spacing as the substrate; then, with increasing film thickness, the total elastic strain energy increases, and a relaxed structure would form. Regions of relatively good fit are separated by misfit dislocations that relieve a portion of the misfit. As the film continues to grow, more misfit is relieved until at infinite thickness the elastic strain is totally eliminated.

The issues just raised with respect to misfit dislocations are but a part of a larger concern for defects in epitaxial films. Such defects may degrade many device properties by altering carrier concentrations and mobilities. The sources of defects in epitaxial films can be divided into the following categories [62]:

- Propagation of defects from the substrate into the epitaxial layer  
A classic example of this type of defect is the extension of a dislocation from the substrate surface into the growing film. In order to limit the presence of this type of defect, substrate treatments are usually carried out during the realization of electronic devices. In the case of biepitaxial junctions, the substrates were annealed to allow a partial reorganization of the surface structure or cleaned with a soft etching in oxygen. Another example is represented by the formation of defects in the YBCO films due to twin boundaries in the substrate. This condition is found in LAO-based junctions and will be discussed in section 6.1.
- Stacking faults.  
Stacking faults are crystallographic defects in which the proper order of stacking planes in crystal lattice of the deposited material is interrupted.
- Formation of precipitates or dislocation loops due to supersaturation of impurities  
The precipitates and dislocations usually are the result of solid-state reactions subsequent to growth. Films containing high dopant or impurity levels are susceptible to such defects. In the case of YBCO, precipitated species frequently observed are yttrium oxide ( $\text{Y}_2\text{O}_3$ ) and the Y211 phase ( $\text{Y}_2\text{BaCuO}$ ), often accumulating at the grain boundary [63]. Both these species are insulating, they can therefore change significantly the transport properties of the junctions. In Figure 3.8 images of such impurities found in biepitaxial structures are shown..

- Formation of low-angle grain boundaries and twins.  
Low angle grain boundaries and twins arise from misoriented islands that meet and coalesce. When this happens, small-angle grain boundaries or crystallographic twins result.

### **3.3.3. Epitaxial relations in our junctions' structure**

In this paragraph we will clarify the epitaxial relations existing in our junctions. This allows a better understanding of the biepitaxial junctions' structure and the issues involved in the realization of single phase epitaxial thin films.

For clarity, in this paragraph we will refer to (110) oriented STO substrates; given the structural similarity, what is said is valid for (110) LAO substrates also.

#### ***CeO<sub>2</sub> growth on (110) oriented STO substrate***

On (110) oriented STO substrates, (110) growth orientation is obtained for CeO<sub>2</sub> suitably tuning the deposition conditions. The (110) CeO<sub>2</sub> orientation can be understood in the framework of a near coincidence lattice site model, in which the epitaxial layer grows with its lattice sites in correspondence with the substrate's ones [64]. (110) STO planes have a rectangular lattice, with sides parallel to the [001] and [1-10] directions having lengths of 0.391 nm and 0.552 nm respectively. A (110) oriented CeO<sub>2</sub> film has also a rectangular lattice, with dimensions 0.522 nm and 0.780 nm, therefore can grow in such a way to fit the STO lattice within 2%, as showed in Figure 3.9a (the crystal structure and lattice parameters of the materials used for the fabrication of biepitaxial junctions are listed in Table 3-1). Traces of (111) CeO<sub>2</sub> orientation were sometimes found on the samples grown in nonoptimized deposition conditions; this growth has a good fit with only with the [001] direction of the STO lattice.

High quality biepitaxial junctions are realized using vicinal STO substrates, in which the normal to the substrate's surface is tilted of an angle  $\alpha$ , called vicinal angle, with respect of the normal of the lattice plane. The vicinal angle used during this work has been 3.5°. The (110) CeO<sub>2</sub> growth follows this vicinality, as will be showed in section 3.4.3.

#### ***YBCO growth on (110) oriented CeO<sub>2</sub> seed layer***

The [100] CeO<sub>2</sub> axis has the same length, within 0.6%, of the diagonal of the YBCO cell in the *a-b* plane. Therefore, YBCO films grow *c*-axis oriented on the (110) CeO<sub>2</sub> seed layer with a 45° rotation of its in plane directions with respect to the [001] and [1-10] CeO<sub>2</sub> directions. This orientation is shown in Figure 3.9b. Such a configuration allows to achieve a near coincidence of the epitaxial layer and substrate lattice sites along only one of the crystallographic directions (that is [001] CeO<sub>2</sub>). Such a “weak” lattice site coincidence is enough to select a single in-plane YBCO orientation on the vicinal substrates. On exact substrates, fractions of the non-rotated orientation, shown in Figure 3.9c, also allowing partial site coincidence, are sometimes found. The effects of the substrate vicinal cut in removing such duplicity will be described later in the paragraph.

#### ***YBCO growth on (110) oriented STO substrate***

The growth of YBCO films on (110) oriented STO substrates can lead to two orientations: (110) and (103). The competition between the two was extensively studied by Poelders *et al.*[65]. Their conclusion was that the relative amount of the two growths is strongly dependent on the film deposition temperature, with (103) growth being predominant at higher temperatures. During the fabrication of biepitaxial junctions, great care was dedicated to the tuning of the deposition parameter in order to obtain single phase (103)

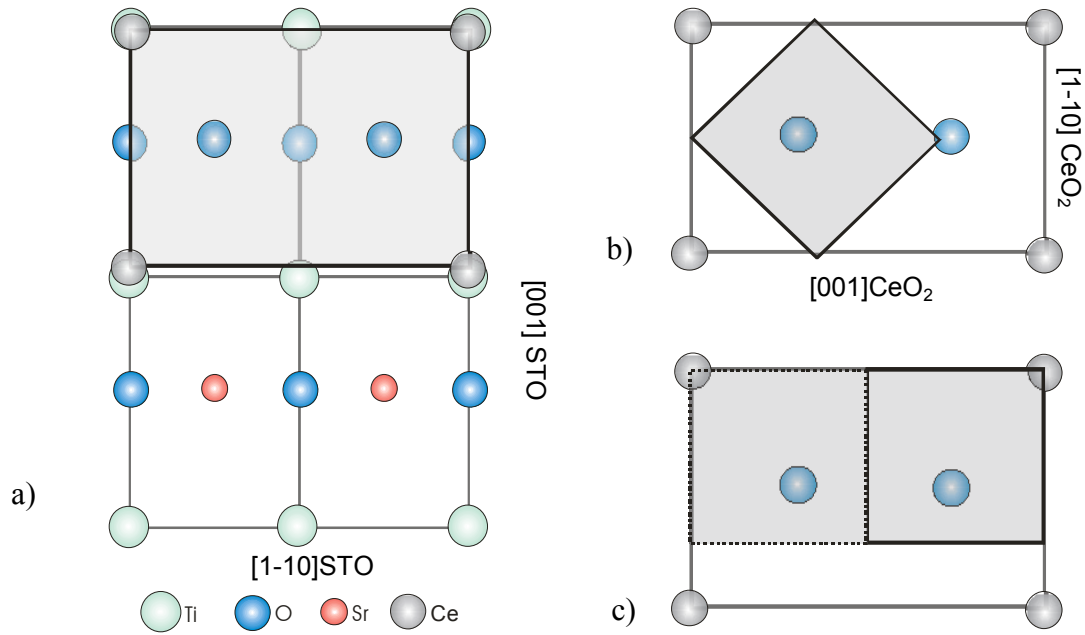


Figure 3.9 Epitaxial arrangement of the (110) CeO<sub>2</sub> cell on the surface lattice of the (110) STO substrate (a) and of the (001) YBCO cell on the (110) CeO<sub>2</sub> (b), with a 45° in plane rotation of the YBCO c-axis. Sometimes, the non rotated configuration (c) is also found as a minority phase when non vicinal substrates are used.

oriented YBCO, and exclude the presence of (110) components.

Due to the symmetry of the exact (110) STO surface, (103) YBCO grains can align the *c*-axis in two directions, that is parallel to [100] STO or to [010] STO (Figure 3.10a) [65,66]. The two growths are labelled (013) and (103); they only differ in the exchanging of the *a*- and *b*- axes. When, during the film growth, domains with the two orientations meet, triangular grains and 90° tilt boundaries are formed (Figure 3.10b) [67]. The two growth directions also lead to the formations of different types of GBs in the contact with the (001) growth on the seed layer. In one case, an almost perfect interface, suitable for the fabrication of homogeneous junctions is formed (Figure 3.10c), in the other the formation of a rough irregular interface takes place (Figure 3.10d). These configurations are different also for the microstructure, which could give rise to different transport properties. In order to select just one of the two orientations, vicinal substrates have been employed.

### ***Effects of the substrate vicinal cut***

The existence of both (103) and (013) orientations in YBCO films grown on (110) STO substrates is due to the orthorhombic YBCO structure with just a small difference between the length of the *a* and the *b* axes (only ~0.007 nm); therefore the two axes can easily swap, with the creation of twinning domains. In order to remove such mechanism, vicinal substrates can be employed, in which the two fold symmetry of the substrate surface is broken and a preference for only one domain is developed.

In vicinal substrates, terraces are created with height of a single cell and width depending on the substrate lattice parameter and on the vicinal angle and direction. From simple geometrical consideration, it results that the width of the terraces is proportional to the tangent of the vicinal angle, therefore it is infinite for perfect substrates with no miscut and decreases with increasing vicinality. The creation of the terraces changes the surface energy of the crystal and the unit cells at the interface are deformed [68]. On substrates with vicinal angle in

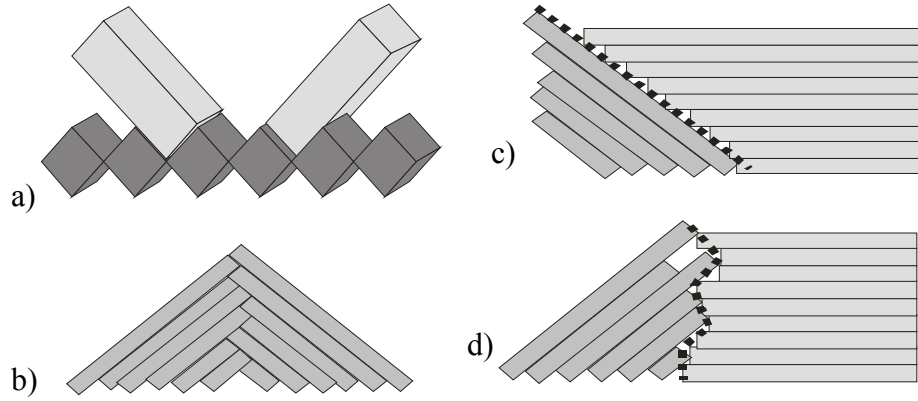


Figure 3.10 Issues related to YBCO growth on (110) oriented STO. (a) YBCO grains can align the  $c$  axis in two directions, giving rise to the (103) or to the (013) growth. When these two directions meet triangular grains are created with  $90^\circ$  tilt boundaries (b). They can also lead to the formation of different types of GB when meeting the (001) growth (c) and (d).

the [010] direction, as used during this work, this results in the deformation in the horizontal planes of the interface layers and a reduction in the lattice parameter perpendicular to the vicinal direction. The cells assume a more rectangular shape compared to the original square lattice of STO substrate. Due to this effect, YBCO tends to align its longer  $b$  axis along the step edges and its shorter  $a$  axis along the strained direction. As the vicinal angle increases, the substrate's terraces width decreases and the step edge density becomes larger; therefore more YBCO domains have the tendency to align. During this work, a vicinal cut of  $3.5^\circ$  towards the [010] direction was found to be sufficient for obtaining single domain (103) YBCO growth. For the same reasons, the non-rotated (001) YBCO growth on  $\text{CeO}_2$  (Figure 3.9c) is suppressed using vicinal substrates.

### 3.4. Thin films realization

During this work, different techniques were used to deposit the materials constituting the various layers of the biepitaxial devices. The metallic films used for the realization of contact pads and during some steps of the electron beam lithography were realized by electron beam evaporation, whereas the oxide films by magnetron and RF sputtering and pulsed laser deposition. Critical to the analysis and design of deposition processes involving highly energetic species is an understanding of what happens when ions collide with surfaces. Some of the interactions that occur are shown schematically in Figure 3.11. Each depends on the type of ion (mass, charge), the nature of surface atoms involved, and, importantly, on the ion energy. The number of such interactions suggests, again, that the problem of multi component thin films growth is complex, and still presents many obscure sides.

In this paragraph, a brief introduction of the deposition techniques, in particular referring to the deposition systems used during this work, will be given.

#### 3.4.1. Evaporation

Evaporation is a rather straightforward technique used to realize films of simple metals or bi-component alloys. The material to be evaporated is heated until its vapour pressure gives the evaporation rate desired, as follows from the formula:

$$\Gamma_e = 5.8 \times 10^{-2} \sqrt{M / TP_e}$$

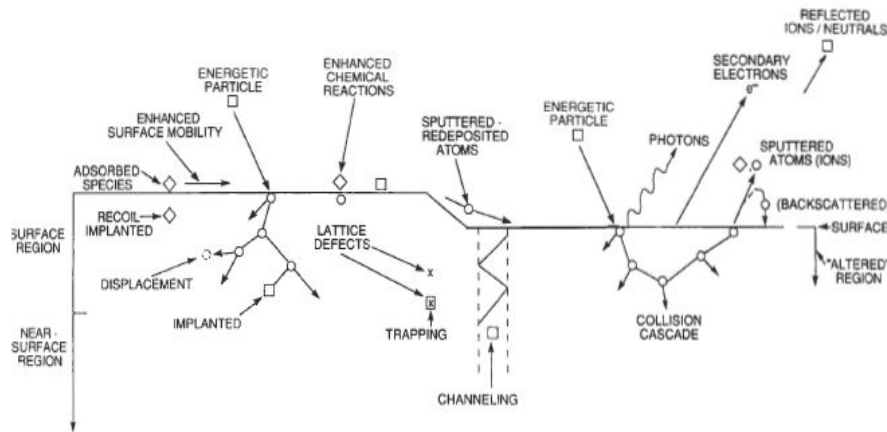


Figure 3.11 Sketch of the many effects of energetic particles bombardment during the growth of a film

where  $\Gamma_e$  is the mass evaporation rate,  $M$  the mass of the evaporated element,  $T$  the temperature and  $P_e$  the vapour pressure. Two modes of evaporation can be distinguished in practice, depending on whether the vapour effectively emanates from a liquid or solid source. A melt will be required if the element to be evaporated does not achieve a vapour pressure greater than  $10^{-3}$  torr at its melting point. Most metals fall into this category, and effective film deposition is attained only when the source is heated into the liquid phase. On the other hand, elements such as Cr, Ti, and C reach sufficiently high vapour pressures below the melting point and, therefore, sublime.

In order to obtain highly pure evaporated films, during this work e-beam evaporation was used. In the most common configuration of the gun source, electrons are emitted from heated filaments and a transverse magnetic field is applied, which serves to deflect the electron beam in a  $270^\circ$  circular arc and focus it on the hearth of the evaporant charge placed in a water-cooled crucible at ground potential. The purity of the evaporant is ensured because only a small amount of charge melts or sublimates so that the effective crucible is the unmelted skull material next to the cooled hearth.

### 3.4.2. Magnetron sputtering

In a typical sputtering system, the material to be deposited is in the form of a pellet called target. It is connected to the negative terminal of a dc or RF power supply, therefore represents the cathode of the system. The substrate that faces the cathode is usually grounded, and heated. After evacuation of the chamber, the process gas, typically argon, is introduced and serves as the medium in which a discharge is initiated and sustained. Microscopically, positive ions in the discharge strike the cathode plate and eject neutral target atoms through momentum transfer. These atoms enter and pass through the discharge region to eventually deposit on the growing film.

The manner in which a glow discharge progresses in a low-pressure gas using a high-impedance dc power supply is as follows. A very small current flows at first due to the small number of initial charge carriers in the system. As the voltage is increased, sufficient energy is imparted to the charged particles to create more carriers. This occurs through ion collisions with the cathode, which release secondary electrons, and by impact ionization of neutral gas atoms. With charge multiplication, the current increases rapidly, but the voltage, limited by the output impedance of the power supply, remains constant. Large numbers of electrons and ions are created. Eventually, when the electrons generated produce sufficient ions to regenerate the same number of initial electrons, the discharge becomes self-sustaining. The gas begins to glow now, and the voltage drops, accompanied by a sharp rise in current. At this state "normal glow" occurs. A further increase in power results in higher voltage and current



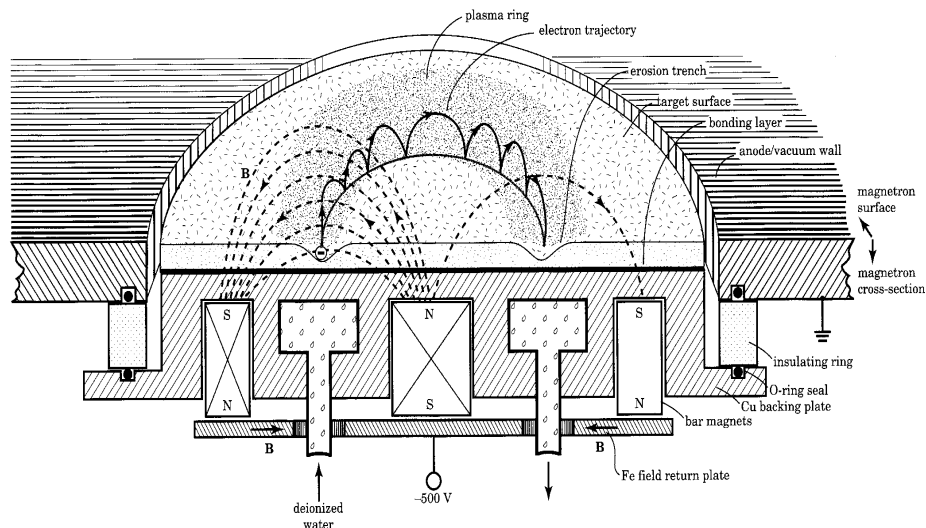


Figure 3.12 Sketch of a magnetron sputtering source. The presence of a magnetic field traps the electrons near the target, prolonging the electron residence time in the plasma and enhancing the probability of ion collisions

density levels. The “abnormal discharge” regime has now been entered, and this is the operative domain for sputtering and other discharge processes (e.g., plasma etching of thin films).

The addition of a magnetic field to the plasma dynamic is used to enhance the sputtering yield. When a magnetic field is superimposed on the electric field between the target and substrate, electrons experience the Lorentz force in addition to electric field force and their trajectory becomes spiral-like. Therefore, magnetic fields prolong the electron residence time in the plasma and thus enhance the probability of ion collisions. This leads to larger discharge currents and increased sputter deposition rates.

In magnetrons, electrons ideally do not even reach the anode but are trapped near the target, enhancing the ionizing efficiency there. This is accomplished by employing a magnetic field oriented parallel to the target and perpendicular to the electric field. Therefore, the magnetic field lines first emanate normal to the target, then bend with a component parallel to the target surface and finally return, completing the magnetic circuit (Figure 3.12). Electrons emitted from the cathode are initially accelerated toward the anode, executing a helical motion in the process; but when they encounter the region of the parallel magnetic field, they are bent in an orbit back to the target. By suitable orientation of target magnets, a “race track” can be defined where the electrons hop around at high speed. Target erosion by sputtering occurs within this track because ionization of the working gas is most intense above it.

### 3.4.3. $\text{CeO}_2$ films deposited via RF magnetron sputtering

RF sputtering was invented as a means of depositing insulating thin films. When an ac signal above 50 kHz is applied to the electrodes of a sputtering system, electrons oscillating in the glow region acquire enough energy to cause ionizing collisions, reducing the need for secondary electrons to sustain the discharge. Moreover, RF voltages can be coupled through any kind of impedance so that the electrodes need not be conductors. This makes it possible to sputter any material irrespective of its resistivity.

RF sputtering essentially works because the target self-biases to a negative potential. Once this happens, it behaves like a dc target where positive ion bombardment sputters away atoms for subsequent deposition. Negative target bias is a consequence of the fact that electrons are considerably more mobile than ions and have little difficulty in following the

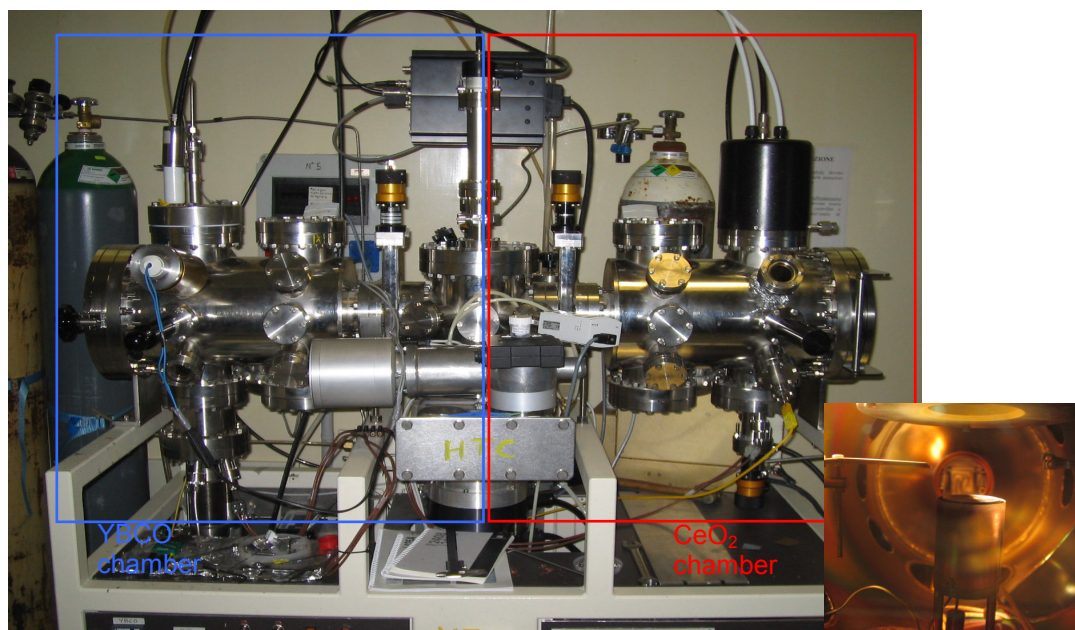


Figure 3.13 The sputtering system used during this work. The system has two separated chambers, one is dedicated to YBCO films deposition and the other to  $\text{CeO}_2$ . The latter one was set up during this work. In the inset, an inside view of the  $\text{CeO}_2$  chamber is shown: the heater, the shutter and the bottom part of the magnetron are visible.

periodic change in the electric field. The disparity in electron and ion mobilities means that isolated positively charged electrodes draw more electron current than comparably isolated negatively charged electrodes draw positive ion current.

A RF sputtering magnetron chamber was set up during this work to deposit the  $\text{CeO}_2$  seed layer films. The complete sputtering system is shown in Figure 3.13. It is composed of two cylindrical chambers connected by a central section through which the pumping is carried out by the means of a turbomolecular and a rotary pumps connected in series. The  $\text{CeO}_2$  deposition chamber is equipped with a planar magnetron source connected to an RF generator and a matching unit, a heater for the control of the substrate temperature and several pressure sensors. The process gas is introduced through mass flow controllers, allowing a precise calibration of the reciprocal ratio of process gas. Together with the argon gas necessary to the plasma generation, pure oxygen is introduced to allow a proper oxygenation of the  $\text{CeO}_2$  film; the ratio between Ar and  $\text{O}_2$  is kept at 1:1.

The deposition procedure involves the following steps (note that the steps sequence is common to many deposition procedures):

- The substrate is loaded and glued to the heater surface using a silver-based compound
- The chamber is evacuated to a pressure of  $\sim 10^{-7}$  mbar
- The temperature of the heater is slowly raised to anneal the substrate  
This step is carried out at  $750^\circ\text{C}$  for about one hour. The aim is to remove impurities and promote a partial reorganization of the substrate surface, reducing the number of defects that could propagate into the film.
- The gases are introduced into the chamber and the plasma is switched on. While the substrate is covered by a shutter, the plasma is let on for several minutes to allow the stabilization and the cleaning of the target surface
- The shutter is removed and the heater raised to approach the plasma for the desired deposition duration
- At the end of the deposition, the heater temperature is ramped down.

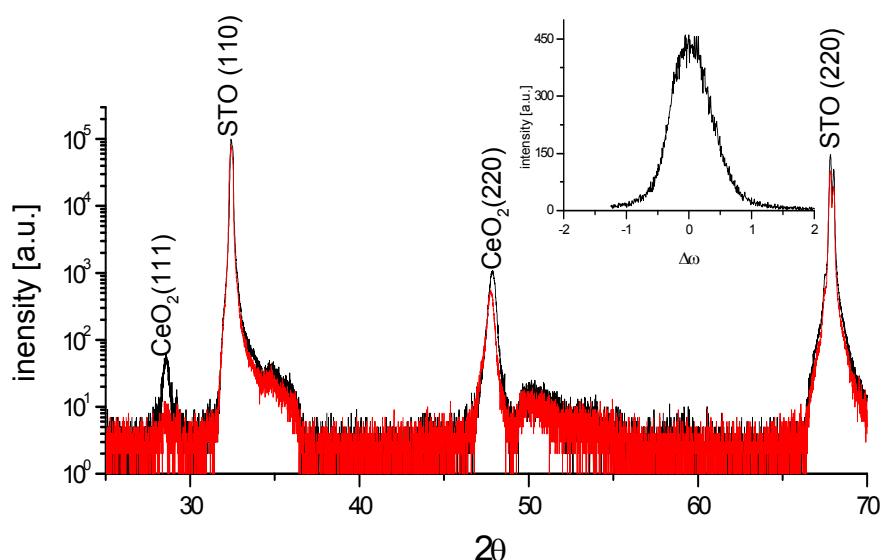


Figure 3.14 X-ray diffraction pattern of  $\text{CeO}_2$  films realized during this work. In the  $\theta/2\theta$  symmetric  $\theta/2\theta$  measure, the orientation of the phases present in the film can be detected. The black curve shows a predominant orientation (110) with traces of (111) phase. The red curve shows a single (110) orientation. In the inset, a rocking curve of the (220)  $\text{CeO}_2$  peak is shown. The FWHM is  $0.7^\circ$ , meaning a very good alignment of the (110) family of planes.

During this work, the main deposition parameters were tuned to obtain high quality  $\text{CeO}_2$  films. The properties we are more concerned of are the crystallographic orientation of the films and the surface smoothness.

As described in section 3.3.3, the  $\text{CeO}_2$  crystallographic orientation needed for this type of biepitaxial junctions is the (110) orientation. Competing with this growth there is the (111) one. If traces of this latter are present in the  $\text{CeO}_2$  films, the subsequent YBCO growth can be hindered. To check the presence of (111) orientation,  $\theta/2\theta$  symmetric diffraction patterns were measured. Figure 3.14 shows an example of such measurements. The (111) phase is clearly present in the black curve and absent in the red one. In the inset a rocking curve around the  $\text{CeO}_2$  (220) peak is also shown. The (220) peak is found at  $\Delta\omega=0$  with respect to the substrate alignment, this means that the  $\text{CeO}_2$  growth follows perfectly the vicinal cut of the STO. The rocking curve allows an estimation of the alignment of the planes belonging to the same family; a narrow peak means a good alignment. The full width at half maximum (FWHM) of the peak shown in the inset of Figure 3.14 is  $0.7^\circ$ , a good value for a film grown on a vicinal substrate.

In order to obtain single-oriented (110)  $\text{CeO}_2$  films, a detailed study on the effects of the deposition parameters on the orientation of the films has been carried out during this work. The main parameter influencing the film orientation is, as often, the deposition temperature. With deposition temperature we mean the temperature measured by a thermocouple inserted under the heater surface. This temperature is a good estimation of the substrate's one. One should not forget, nevertheless, that, the plasma deposition being a very complex phenomenon, there is a strong interaction among all the deposition parameters. Optimal results can be obtained only by taking into account and tuning different parameters in parallel. During this work we found that also the deposition pressure and the distance between the substrate and the target have a great influence on the final orientation of the film. Once found the range of temperature, pressure and distance giving satisfactory results, i.e. a predominant (110) growth, we chose to keep constant the temperature and vary the other two parameters. To evaluate the results x-ray diffraction was again used. As mentioned in section 3.2.1, x-ray diffraction patterns can give a rough estimation of the relative amount of the phases present in

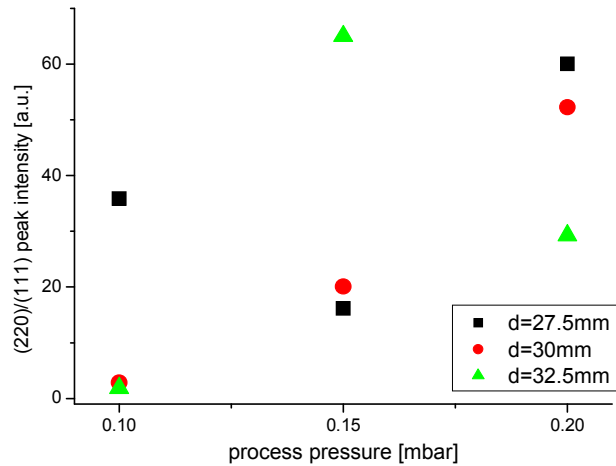


Figure 3.15 effect of the process gas pressure and substrate-target distance in the ratio between the (220) and (111) peaks intensities, measure with x-ray diffractionmetry.

a crystalline film by the ratio of the diffraction peaks. The ratios between the (220) and the (111) peaks intensities are shown in Figure 3.15 for three values of pressure and distance. An increase in the pressure was found to bring an increase in the (220)/(111) intensity ratio, except for the further distance ( $d=32.5\text{mm}$ ) data. These last data were found to be very scattered; probably in this condition the substrate is outside the plasma optimal zone and the other deposition parameters have less influence with respect to such instability. The optimal deposition conditions found with the help of these data are listed in Table 3-2.

CeO <sub>2</sub> - RF sputtering deposition parameters	
T <sub>heater</sub>	790°C
p <sub>O<sub>2</sub>+Ar</sub>	0.2 mbar
O <sub>2</sub> :Ar	1:1
substrate-target distance	27.5mm
plasma power	40W
deposition rate	4nm/min

Table 3-2 Optimized CeO<sub>2</sub> deposition parameters for RF sputtering

Once obtained single oriented films, an analysis of the surface quality was carried out. The smoothness of the CeO<sub>2</sub> layer is necessary for the subsequent growth of the YBCO film. The tuning of the RF plasma power was found to be of great importance to obtain smooth films with no precipitates. CeO<sub>2</sub> films deposited in the optimal conditions of temperature, pressure and distance and at a power of 100W showed, when imaged with an AFM, precipitates with an average height of tens of nanometres. Reducing the power to 40W the precipitates disappear and the films show a very smooth surface (Figure 3.16a,b). The uniformity of the surface is confirmed by the glancing incidence x-ray reflectivity measurement: the possibility to obtain the oscillations showed in Figure 3.16c is related to the presence of a smooth surface. From these oscillations it was also possible to measure the thickness of the films, therefore calculate the sputtering rate of the system (listed in Table 3-2).

Finally, it is interesting to note a peculiarity in the CeO<sub>2</sub> structure emerging from the AFM analysis. The two images of Figure 3.16a and b refer to a 17 nm and 27 nm films respectively, the direction of the substrate vicinal cut is also showed. The width of the grains in the two images is roughly the same, but in 27nm film they are also elongated along a

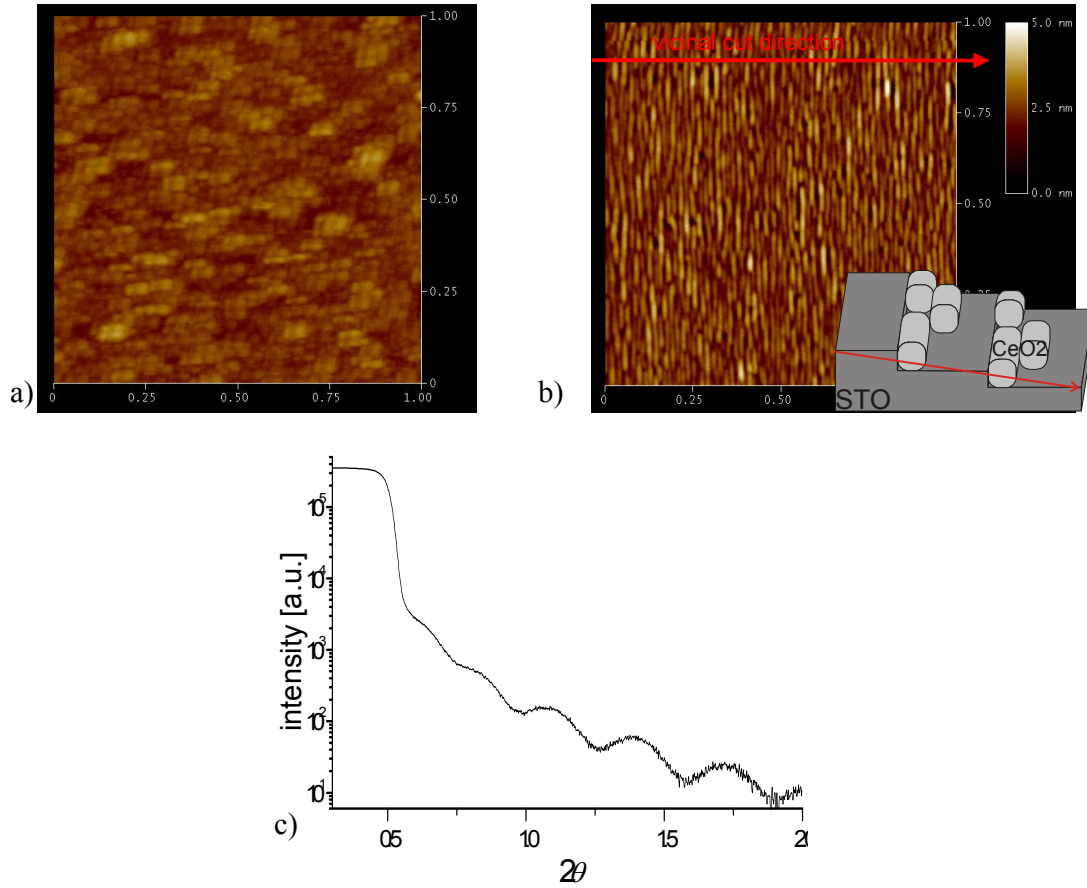


Figure 3.16 AFM (a) and (b) and glancing incident reflectivity (c) measurements on sputtered  $\text{CeO}_2$  films. Images (a) and (b) refer to 17 nm and 27 nm films respectively; in the inset of (b) a sketch of the probable growth mechanism is shown. Figure (c) shows the thickness measurement of film (b).

common direction. This suggests that the grains, after nucleating, tend to grow with the deposition time along a preferential direction, perpendicular to the substrate vicinal cut. Therefore it is possible to conclude that the grains tend to nucleate and grow along the steps in the vicinal substrate (inset in Figure 3.16b). This is a hint of layer by layer growth (see section 3.3.1) and a further proof of the high structural quality of the films realized.

#### 3.4.4. YBCO films deposited via inverted cylindrical magnetron sputtering

The presence of oxygen is a crucial feature for the transport properties of YBCO; it has to be carefully controlled in order to obtain an optimal doping and maximum critical temperature. Therefore, the deposition of YBCO films takes place in a mixed atmosphere of oxygen and argon. In a standard planar magnetron configuration, the oxygen atoms would generate negative ions; they would be accelerated towards the substrate causing, in turn, the bombardment of the just deposited film. One of the configurations studied to avoid this problem is the cylindrical configuration [69]. The target has the shape of a hollow cylinder, with the magnets placed along its internal or external surface. The external configuration is called inverted cylindrical magnetron (ICM) and is used since many years for the realization of high quality YBCO films. The magnetic field lines are radially oriented with respect to the target surface, keeping the ions inside the target surface and preventing them from reaching the substrate where the deposition is taking place.

The deposition procedure steps for the deposition of YBCO films via ICM are, basically,

similar to the ones already described for CeO<sub>2</sub> films, with the only addition of an annealing step at the end of the deposition procedure. During this step the oxygen is forced in the structure promoting the transition from tetragonal to orthorhombic. The temperature and pressure parameters used in this step are listed in Table 3-3.

A small but important detail was also improved during this work: thanks to the installation of a high performance ceramic heater, capable to reach 1100°C, the deposition of YBCO was carried out without gluing of the sample to the heater surface. The consequent easiness in unloading the sample proved to be of great help when using LAO as a substrate. This material is, indeed, characterized by higher fragility when compared to STO. During its removal from the heater surface, at the end of the YBCO deposition, cracks are often generated, which could hinder the devices properties. Avoiding the use of glue, instead, allowed an easier realization of LAO based junctions.

The deposition calibration for biepitaxial junctions' YBCO films is a rather complex problem. It is necessary to promote two radically different kinds of growth, the (001) on the seed layer and the (103) on the substrate, during the same deposition process. It was often found, during this work, that the conditions for an optimal growth and superconducting properties of one of them didn't match the conditions for the other. A very narrow parameter window, in conclusion, is available to obtain, at the same time, good quality for both growths. These parameters are listed in Table 3-3.

YBCO - ICM sputtering deposition parameters	
T <sub>heater</sub>	850°C
P <sub>O2+Ar</sub>	0.7 mbar
O <sub>2</sub> :Ar	1:1
substrate-target distance	2 mm
plasma power	100W
deposition rate	4nm/min
T <sub>annealing</sub>	450°C
P <sub>O2 annealing</sub>	800 mbar

Table 3-3 Optimized YBCO deposition parameters for ICM sputtering

Figure 3.17 presents a summary of the x-rays measurements realized on the YBCO films deposited during this work. These measurements were performed on an YBCO film deposited on a STO substrate partially covered by a CeO<sub>2</sub> seed layer. In this way, it was possible to analyse at the same time the two different growths of the YBCO film.

In the top panels symmetric  $\theta/2\theta$  diffraction patterns are shown. The measure on the left side was carried out adding a shift in  $\theta$  corresponding to the substrate vicinal cut. In this way, the substrate's (110) planes were brought in Bragg's condition. As already showed in section 3.4.3, the CeO<sub>2</sub> film follow the vicinality of the STO, therefore the (220) CeO<sub>2</sub> peak is visible in this measurement. On the other hand, it was found out that YBCO films of the thickness used for our junctions (above 150nm) relaxes the substrate and seed layer's vicinality. In Figure 3.17a, indeed, no YBCO peaks are present (with the exception of a tiny (005) peak). In order to bring the YBCO planes in Bragg's conditions it is necessary to remove the vicinality shift, as it was done for the measure in Figure 3.17b. The (001) family of planes becomes parallel to the samples surface and the diffraction peaks, even of the 8<sup>th</sup> order, are clearly visible. In Figure 3.17c the rocking curve of the (005) YBCO peak is compared with the one for the (220) CeO<sub>2</sub>. The FWHM is 0.6°, hint of a highly ordered film. The (005) YBCO peak is found at  $\Delta\omega \approx 3.5^\circ$  with respect to the substrate and the CeO<sub>2</sub> orientation since YBCO doesn't follow the STO vicinality.



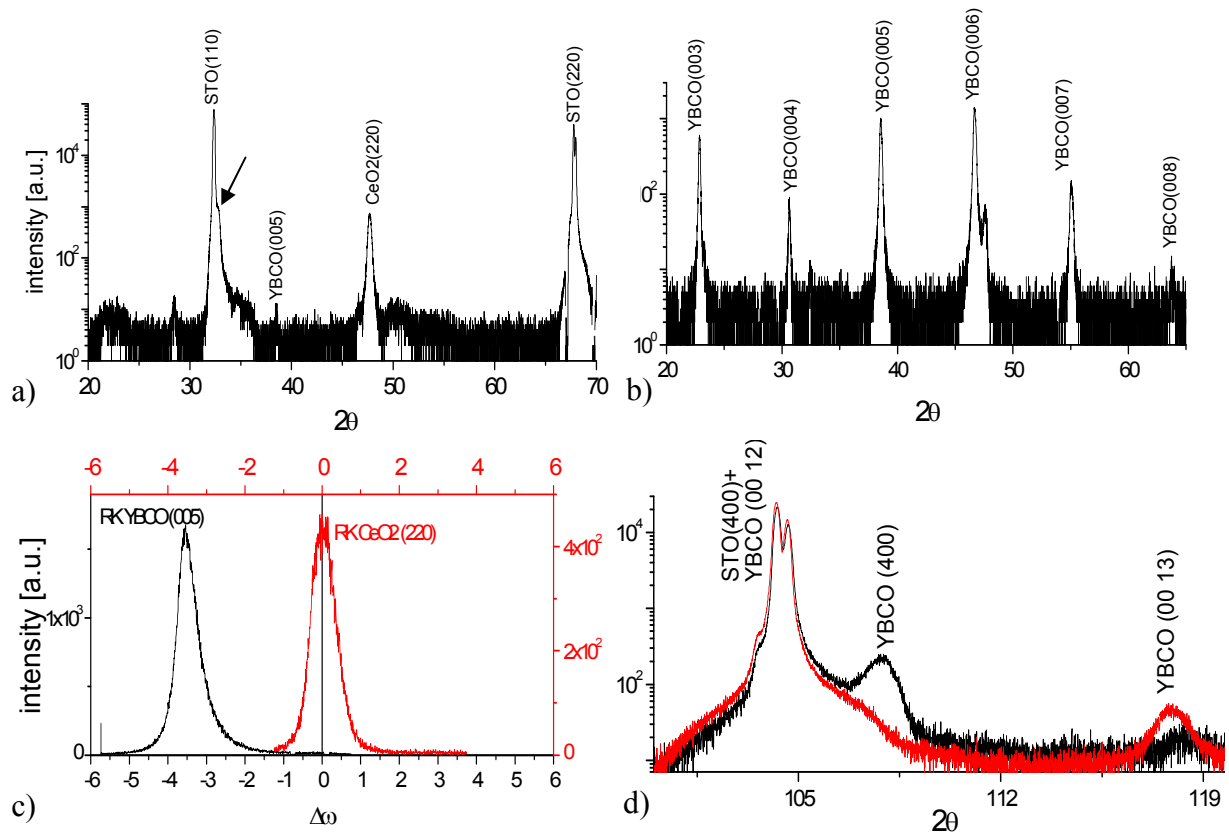


Figure 3.17 Set of x-ray measures performed on an YBCO film grown on a STO (110) substrate partially covered by a (110) CeO<sub>2</sub> seed layer film. (a) and (b) are two symmetric  $\theta/2\theta$  diffraction patterns aligned on the substrate and on the YBCO respectively. The rocking curves of (c) demonstrate that the CeO<sub>2</sub> film follows the vicinality of the substrate, while the YBCO film doesn't. In (d) two asymmetric  $\theta/2\theta$  patterns are shown. They are used to determine the presence of the (110) phase (in this case the phase is absent).

As regards the (103) growth, the  $2\theta$  value for the (103) reflection is very close to the STO (110) one and, since the substrate peak is very high, the (103) peak will fall under it. In Figure 3.17a, indeed, a shoulder is barely visible close to the STO (110) peak (it is indicated with an arrow). Moreover, it has been demonstrated that the (103) YBCO planes and the (110) STO planes are not perfectly aligned ( $\Delta\omega=0.43^\circ$ ) [66], therefore (103) planes are not in perfect Bragg condition in the measurement conditions of Figure 3.17a. Asymmetric measurements are necessary also to check for the presence of (110) phase, that is competing with the (103) one when the deposition temperature is not high enough (as reported in section 3.3.3). Two asymmetric  $\theta/2\theta$  are shown in Figure 3.17d. The red curve was obtained with a rotation of an angle  $\omega=45^\circ$ , for the black curve an additional rotation of  $\varphi=180^\circ$  around the normal to the sample surface was imposed. In these plots the (040) YBCO reflection ( $2\theta=105.03^\circ$ ) is absent, proving that the (110) phase content must be below a few percent. Similar types of measurements were performed also on LAO/CeO<sub>2</sub>/YBCO structures.

The surface structure of YBCO films was observed with a scanning electron microscope, in collaboration with the Second University of Naples (SUN). A striking feature of the (001) YBCO films deposited with our ICM sputtering system is the smoothness and uniformity, as showed in Figure 3.18. The absence of impurities and holes in the YBCO structure is important for the realization of reproducible junctions. The high quality of these films makes it possible to realize smaller structure; it is indeed under way a project to realize YBCO nanowires using these films. From the images of Figure 3.18 it is also possible to distinguish

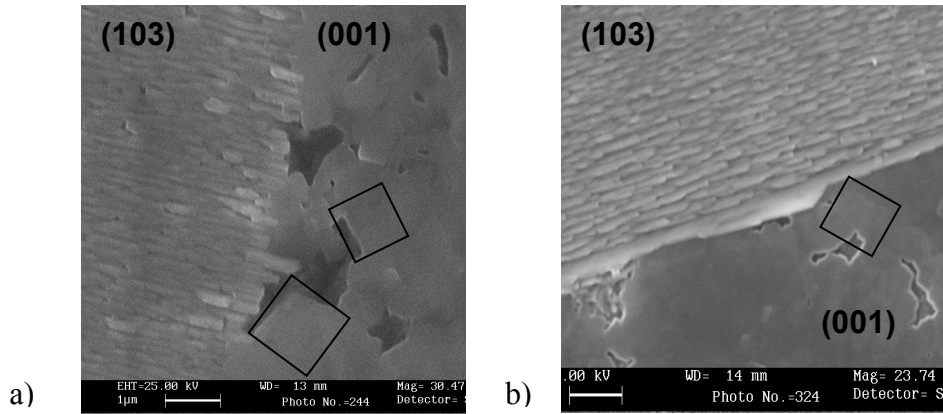


Figure 3.18 SEM images of two samples realized using STO (a) and LAO (b) as a substrate and  $\text{CeO}_2$  as a seed layer. The images dimensions are, for both,  $7 \times 7 \mu\text{m}$ .

the  $45^\circ$  in plane rotation of the (001) YBCO cells, highlighted by the squares in the images. As regards the (103) growth, it is characterized by elongated grains, due to fact that the (103) grains grow faster in a preferential direction [67]. The length of such grains was found to grow, to a certain extent, with increasing the deposition temperature. Longer grains are desirable for biepitaxial junctions, the ideal situation being the one in which the junction bridge crosses only one grain. The grains showed in Figure 3.18 are more than  $1 \mu\text{m}$  long. Finally, the bump in the Figure 3.18b grain boundary is a frequent feature observed in photolithographically patterned samples. It is probably due to a slope in the patterned shape and over-etching of the seed layer, leading to an overgrowth of the (103) YBCO grains on the slope itself and on the (001) area. This problem has been greatly reduced with the e-beam patterning procedure.

### 3.4.5. Pulsed laser deposition

In the pulsed laser deposition (PLD) technique, the target material is vaporized using a laser beam focused on its surface. The target is mounted on a carousel and rotated during the laser deposition in order to allow a uniform ablation of its surface and avoid any dependence in the ablated material from eventual dishomogeneity in the target composition. The ablated species expand until they reach the substrate positioned in front of the target and condense to form the film. The PLD deposition of oxide materials is carried out in pure oxygen atmosphere.

The interaction between the laser and the target is a very complex process, involving many physical mechanisms, often interacting. The formation of the ablated material cloud starts after a short interval ( $\leq 1 \text{ ns}$ ) from the arrival of the laser shot on the target surface. Therefore the shot, whose duration is about 20ns in the case of excimer laser, interacts with the whole vapour-solid system causing an increment in the ablated material amount and in the vapour temperature and ionization. The vaporization due to the laser impact causes a local increase in the temperature in a small volume (the laser spot area on the target per a few micron of depth), with consequences on the composition and angular distribution of the vaporized material. The plasma generated via PLD expands mainly in the direction orthogonal to the target surface, with an ellipsoidal shape called plume. Many studies have shown that the internal composition of the plume is not uniform, the plasma spatial and kinetic distribution depending on many parameters such as the laser energy for unit surface, the shot duration, the deposition gas nature and pressure. Another parameter to be considered is the laser repetition





Figure 3.19 PLD system at the Microtechnology and Nanoscience Department of the Chalmers University used during this work

rate. As described in section 3.3.1, the atomic specie impinging the substrate can diffuse on the surface before coalescing and form stable clusters. Therefore, it is important to select the ablation rate in order to give the species enough time to form a crystalline structure before the arrival of the successive atoms.

The PLD technique is a very versatile one and is used to realize metal, semiconductor as well as oxide films [70]. Moreover, through the use of a motorized carousel controlled by a computer, it is possible to focus the laser on targets of different composition and realize multilayers [71]. The deposition rate for PLD is higher than the one of magnetron sputtering. This offers the advantage of a rapid process, but is, sometimes, a disadvantage for the films quality. The system at the Microtechnology and Nanoscience Department of the Chalmers University (Sweden) used during this work for the realization of some of the biepitaxial samples is showed in Figure 3.19. Both  $\text{CeO}_2$  and YBCO films were realized using this system.

### ***PLD deposition of $\text{CeO}_2$ films***

Also in this case, the focus of the deposition process was on the realization of smooth, single-phase films. The PLD system used is equipped with an RF ion gun; this gave the possibility to perform an in-situ treatment of the STO substrate prior to the  $\text{CeO}_2$  deposition. The treatment consists of an etching in argon, followed by a softer etching in argon and oxygen; the first step is used to clean the surface of the crystal and removing impurities, the second to rearrange it and, thanks to the presence of oxygen, to fill the oxygen vacancies eventually created during the first step. After the substrate cleaning, the deposition is carried out with steps similar to the ones described in section 3.4.3, the only difference being the way the plasma is created. The parameters used for the deposition are listed in Table 3-4.

CeO <sub>2</sub> - PLD deposition parameters	
T <sub>heater</sub>	790°C
p <sub>O2</sub>	0.2 mbar
substrate-target distance	15mm
laser energy	102mJ
repetition rate	1Hz
deposition rate	60 nm/min (0.85nm/shot)

Table 3-4 Optimized  $\text{CeO}_2$  deposition parameters for PLD

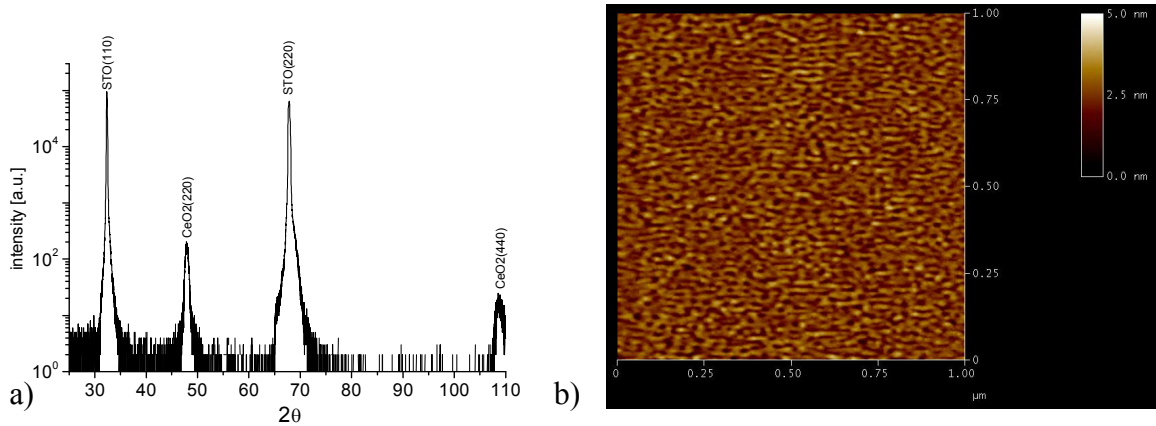


Figure 3.20 X-ray  $\theta/2\theta$  diffraction pattern (a) and AFM image (b) of a CeO<sub>2</sub> film realized with PLD. The film is single oriented and has a smooth and uniform surface

X-ray analysis showed a single-oriented structure for these films and absence of (111) phase (Figure 3.20a). The surface of the films is also smooth (Figure 3.20b) with elongated grains. Comparing the AFM image of Figure 3.20b with the one showed in Figure 3.16b, referring to a sputtered CeO<sub>2</sub> film of about the same thickness, one can note that, in the latter case, the CeO<sub>2</sub> grains are longer. This is compatible with the different characteristics of the PLD and sputtering techniques: the lower deposition rate of the sputtering process probably allows a better organization of the CeO<sub>2</sub> clusters on the edges of the substrate steps and the growth of the grains in a preferential direction.

### ***PLD deposition of YBCO films***

The optimization of the YBCO deposition process via PLD was carried out, during this work, in the view of sub-micron junctions' fabrication. A characteristic often observed in YBCO films, especially the (001) oriented ones, is the presence of voids, as the ones clearly visible in the SEM image of Figure 3.18a [72, 73, 74]. The reason for their creation is to be found in the growth mechanism of YBCO. It is commonly accepted that YBCO grows following an island mechanism. In particular, the growth starts in a 2D fashion [75], with stable nucleuses being composed of elementary cells placed side by side. This kind of growth lasts for about 10-20nm, then the accumulated stress promotes the creation of dislocations (as described in section 3.3.2) with a vector perpendicular to the sample surface. The preferential nucleation site for the dislocations is in the space between the 2D islands. The dislocations start, in turn, to attract the incoming material. The growth proceeds all around the dislocations, turning to 3D growth, and assuming a spiral-like shape. The voids are therefore created in between the 3D islands. It is often observed that the density of voids, behaving as the other types of defects, is higher in correspondence of the grain boundary. When attempting to realize very narrow junctions, it is therefore necessary to reduce these voids.

Once obtained films with an adequate critical temperature, we chose to concentrate our efforts in the optimization of the grain structure of the films tuning the temperature, the deposition pressure and the repetition rate. The (001) YBCO test films were deposited on STO/CeO<sub>2</sub> bilayers; this made the tuning procedure significantly longer for the addition of the CeO<sub>2</sub> deposition step, but made also the testing conditions more likely and close to the real bi-epitaxial structure. As can be seen from the AFM images of Figure 3.21 the effect of a change in both the temperature and the O<sub>2</sub> pressure is dramatic. An increase in the temperature has the effect of promoting the coalescence of the voids, so one goes from a film with many small voids to one with fewer voids but of bigger dimensions. Increasing the pressure from 0.6mbar to 0.8mbar the structure of the film changes completely, small

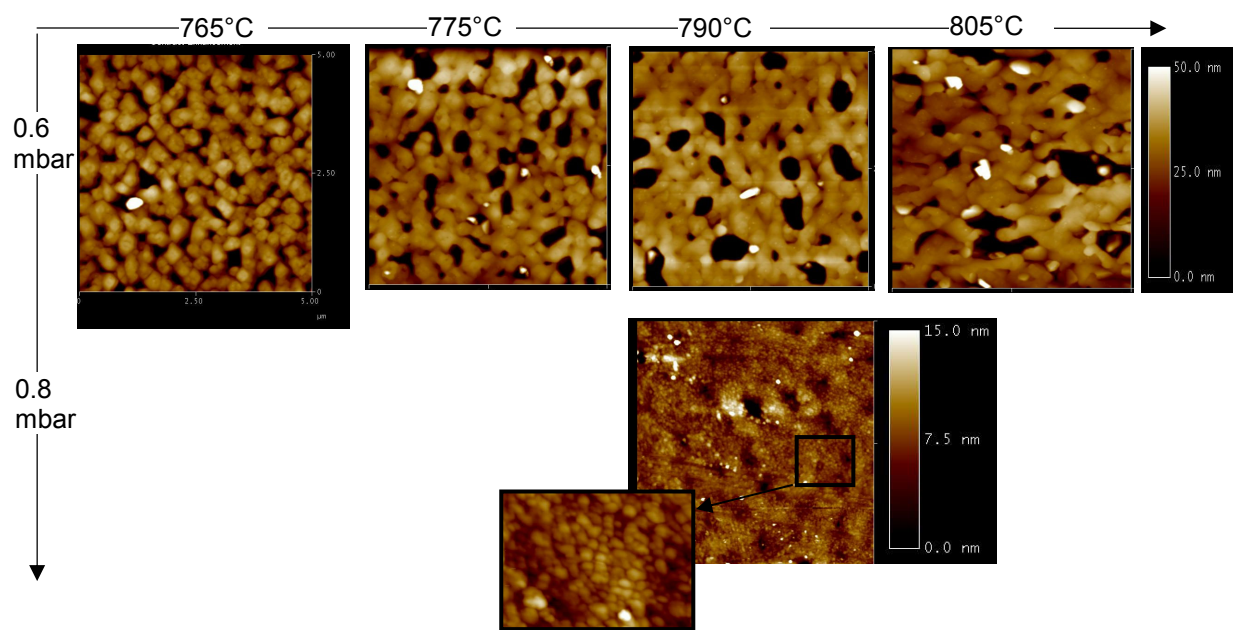


Figure 3.21 5x5  $\mu\text{m}$  AFM images of YBCO films realized via PLD, at different values of temperature and  $\text{O}_2$  pressure.

spherical grains with lateral dimension of about 70nm appear. The reason for the development and the nature of these structures is still not clear. From these considerations, we derived the deposition parameters listed in Table 3-5.

YBCO - PLD deposition parameters	
$T_{\text{heater}}$	790°C
$p_{\text{O}_2}$	0.6 mbar
substrate-target distance	15mm
laser energy	102mJ
repetition rate	10Hz
deposition rate	80 nm/min (0.8nm/shot)
$p_{\text{O}_2}$ annealing	800 mbar

Table 3-5 Optimized YBCO deposition parameters for PLD

#### **4. *Biepitaxial junctions experimental techniques: patterning***

For the realization of biepitaxial junctions three patterning steps are required: 1) definition of the seed layer geometry, 2) definition of the junctions' bridges, 3) definition of the gold pads needed for the electrical connections of the devices. The patterning procedure involves the creation of a protective mask and the etching of the material left exposed. During this work, two different lithographic techniques for the mask realization have been employed, based on UV light (photolithography) or on an electron beam (e-beam lithography). As regards the etching step, ion milling is the technique of choice for HTS devices.

The patterning procedure is a delicate step in HTS junctions' fabrication. The vulnerability of YBCO, especially to oxygen loss and interaction with water, makes it necessary to adopt special measures to ensure extra protection of the material during exposure to liquids like resist, developers and during process steps requiring the heating of the specimen (as for example resist baking). These issues are yet more stringent when realizing structures of smaller dimensions, since the degradation, the loss of oxygen in a small area of the YBCO structure results in a proportionally bigger damage for the structure. A further difficulty is given by the structure itself of the biepitaxial junctions. In bicrystal junctions, the HTS film is grown on a bare substrate; often a (001) oriented substrate is chosen to obtain a (001) YBCO growth, which gives a flat surface. In the case of biepitaxial junctions, on the other hand, the (001) YBCO growth is obtained on the top of a (110) oriented seed layer that has already undergone a patterning step, and the second electrode is obtained with a (103) oriented growth, that is more irregular. The surface of a biepitaxial sample is, in conclusion, intrinsically rougher and uneven, presenting an additional challenge in the application of nanolithographic techniques and requiring higher efforts for the realization of good quality devices and the set up of a reliable patterning procedure. The payoff of such efforts is the possibility to realize more versatile devices, exploiting the peculiar properties of their GB barrier and combining them with the prospects given by the transport in the nanoscale regime.

In this chapter the issues related to the different patterning procedures will be addressed. After a presentation of the photolithographic technique used to realize junctions with width in the micron regime, we will deal in detail with the electron-beam procedure finalized for the realization of narrower junctions, down to 0.6 $\mu$ m wide.

##### **4.1. *Mask making techniques: photolithography***

Micrometer-size biepitaxial junctions were fabricated for the first time in Naples in the late 90ties with the use of photolithographic techniques [11, 27, 64]. Since then, the lithographic process for these junctions has been improved with the aim to reach higher reproducibility and, above all, lower the damage for the YBCO film. An important step added has been the deposition of an Au film on the YBCO one. The Au protects the superconducting film during the fabrication, avoiding the contact with water and other chemicals, and is only removed at the end of the fabrication procedure.

Optical lithography is basically a photographic process by which a light sensitive resist is exposed and developed to form three-dimensional patterns on the substrate. The photoresist image has the exact shape of the intended pattern in the plane of the substrate, with vertical walls through the thickness of the resist; the parts of the substrate covered with resist will be protected from etching.

The general sequence of processing steps for a typical optical lithography process is as follows: substrate preparation, photoresist spin coat, prebake, exposure and development. A resist strip is the final operation in the patterning process, after the resist pattern has been transferred into the underlying layer using ion milling.

Substrate preparation is intended to improve the adhesion of the photoresist material to the substrate. This has been accomplished during this work by substrate cleaning to remove contamination, especially in the form of particulates that could result in defects in the final resist pattern.

After cleaning, a thin, uniform coating of photoresist at a specific, well controlled thickness is realized by the process of spin coating: the photoresist is poured onto the sample, which is then spun on a turntable at a high speed, producing a resist film of a controlled thickness. Stringent requirements for thickness control and uniformity and low defect density call for particular attention to be paid to this process, where a large number of parameters can have significant impact on photoresist layer quality. The resist thickness is an important factor in this process, since it influences the exposure and development parameters and the sharpness of the pattern edges. During this work, layers about 1  $\mu\text{m}$  thick were found to bring the best results in terms of pattern quality and process reproducibility.

After coating, the resulting resist film will contain between 20 – 40% by weight solvent. The post-apply bake process, carried out at 70-100°C, is used to dry the photoresist by removing this excess solvent. The main reason for reducing the solvent content is to stabilize the resist film. At room temperature, an unbaked photoresist film will lose solvent by evaporation, thus changing the properties of the film with time. By baking the resist, the majority of the solvent is removed and the film becomes stable at room temperature. Moreover, the film thickness is reduced, adhesion is improved, and the film becomes less tacky and thus less susceptible to particulate contamination. Typical bake processes leave between 3 and 8% residual solvent in the resist film. Unfortunately, there are other consequences of baking, among them the decomposition of the photoactive resist component, or the oxidizing of another component, the resin. Moreover, the exposure of the YBCO film to such temperatures could promote the loss of oxygen and accelerate YBCO reactions with  $\text{H}_2\text{O}$  and  $\text{CO}_2$  to form hydroxides and carbonates. Thus, during this work, the baking temperature and duration were carefully tuned to maximize the benefits of solvent evaporation and minimize the detriments both for the film and the resist.

After this preparation steps, the sample is ready for UV exposure. It is placed under a glass mask (photomask) where a layer of chromium reproduces the desired pattern, and UV light is shined on. The areas not covered by chromium will be exposed. Before the exposure of the photoresist can begin, the mask must be aligned. In the case of biepitaxial junctions, the second photolithographic step, needed to define the junctions' bridges, is particularly delicate since it is necessary to align the bridges of the mask in correspondence of the grain boundaries. The alignment process is manual and helped by markers previously patterned in the seed layer mask.

Contact and proximity lithography are the simplest methods of exposing a photoresist through the master pattern of the photomask. During this work, contact lithography was used to obtain high resolution: the mask is pressed against the resist-coated sample during exposure. Because of this contact, the gap between the sample and the optical disturbance (the photomask) goes ideally to zero and the diffraction effects, that would distort the pattern, are minimized. Actually, in real systems the mask contact varies across the sample surface, since neither the sample nor the mask is perfectly flat. The major disadvantage of contact lithography is the generation of defects in the sample and the mask due to the contact, but this is a minor inconvenient in the research field.

The resolution of this process has two basic limits: the smallest image that can be projected onto the wafer, and the resolving capability of the photoresist. From the projection imaging side, resolution is determined by the wavelength of the imaging light and the numerical aperture (NA) of the projection lens according to the Rayleigh criterion:  $R \propto \lambda / NA$ . The resolving capability of the photoresist depends on the ability to reconstruct



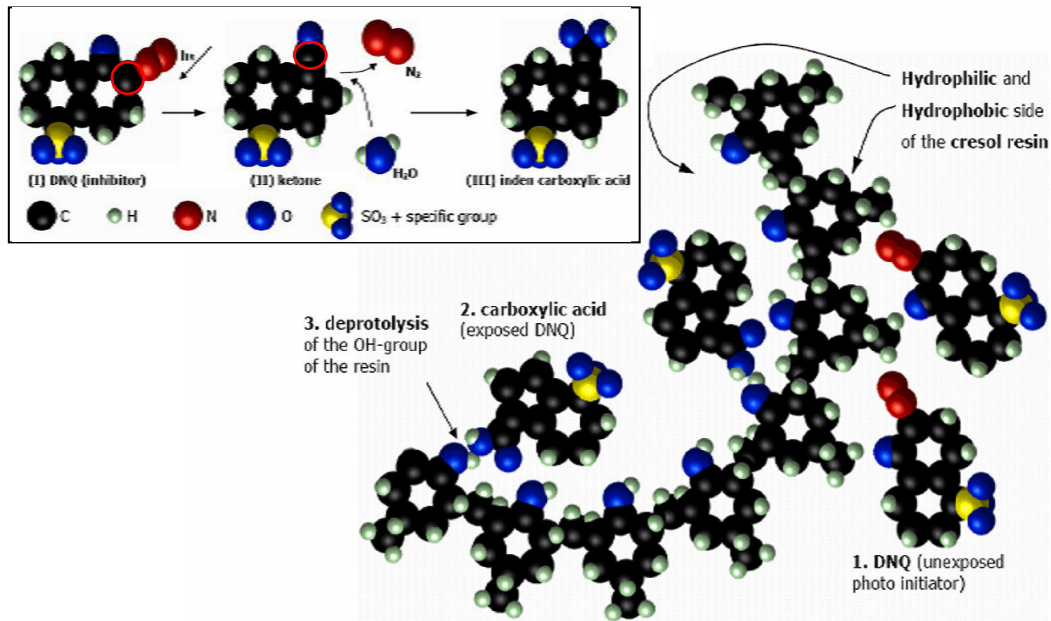


Figure 4.1 Chemical process through which the DQ component of the photoresist forms carboxylic acid under UV exposure (inset) and become soluble by connecting to the hydrophilic part of the resin.

the pattern from the projected image. The resolution achieved during this work was  $\sim 2\mu\text{m}$ .

The basic principle behind the operation of a photoresist is the change in solubility of the resist in a developer upon exposure to light [76]. Thus, a spatial variation in light energy incident on the photoresist will cause a spatial variation in solubility of the resist in developer. The main photoresist components are, besides the solvent, a water soluble resin and a photoactive compound, the diazoquinones (DQ). In positive resist, the DQ acts as inhibitor before the exposure, slowing the rate at which the resist will dissolve in the developing solution, by chemical bonding to the resin. Upon exposure to light, a chemical process occurs by which the inhibitor becomes a sensitizer, increasing the dissolution of the resist. The more sensitive a photoresist is, the faster the process will be, since it requires a smaller amount of light energy to create the chemical change described. In Figure 4.1, this chemical process is showed. When exposed to UV light, the DQ compound releases  $\text{N}_2$ , leaving a reactive carbon site. One way to stabilize the structure is to move one of the carbons outside the ring (showed in red in the inset of Figure 4.1). The oxygen atom is then covalently bonded to this external carbon atom, this molecule is called ketene. In the presence of water, a final rearrangement occurs in which the double bond to the external carbon atom is replaced with a single bond an OH group. This final product is the carboxylic acid. The carboxylic acid is soluble in the water-based developer by connecting to the hydrophilic part of the resin.

Development is undoubtedly one of the most critical steps in the photoresist process. The characteristics of the resist-developer interactions determine to a large extent the shape of the photoresist profile and, more importantly, the linewidth control.

After the patterns have been lithographically printed in photoresist, they must be transferred into the substrate. Etching is the most common pattern transfer approach for HTS devices and will be described later in the chapter. When the etching is complete, the resist is stripped leaving the desired pattern etched into the deposited layer. The stripping is performed by dipping the sample in an acetone bath.

Photolithography is a very well established and reliable technique. It has, nevertheless, some weak points. Firstly, the resolution that is limited, as showed, to the micrometer range.

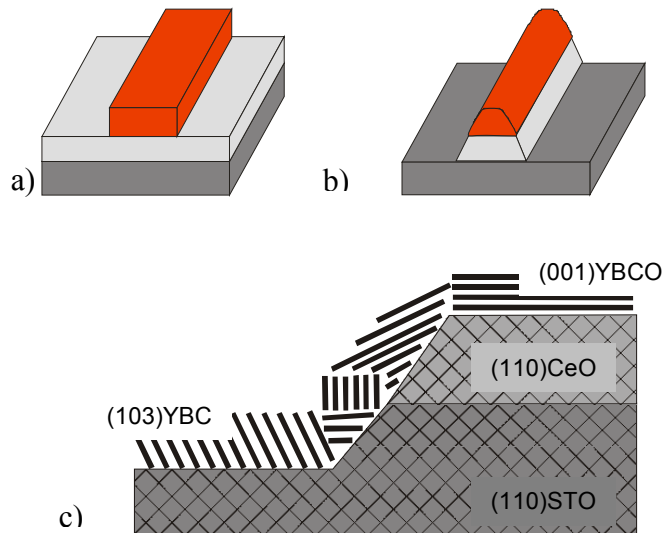


Figure 4.2 Problems related to the photoresist mask edges erosion: a sharp pattern (a) is transformed in a rounded one (b) due to the effect of the ion milling, exposing a larger area of the film that is damaged, and creating a slope. In the case of the seed layer, the slope will promote a disordered growth leading to grain boundaries in series (c). The sketch presents the case in which the seed layer was overetched and a slope created also in the substrate.

Moreover, the photoresist can suffer significant edge erosion. This means that, at the end of the patterning process, the edges of the photoresist mask, and of the patterned film, will not be straight but will show a slope (Figure 4.2). In the case of the seed layer pattern, this slope could interfere with the growth of the YBCO grains. Transmission electron microscope analysis have shown that the epitaxial growth is perturbed, different crystalline orientations appear with the creation of grain boundaries connected in series, in an uncontrolled way [77]. During this work, it has also been often observed an overgrowth of the (103) YBCO grains on the (001) grains, as showed in the SEM images of Figure 1.17b. As regards the YBCO patterning process, a higher edge erosion of the photoresist mask exposes a larger area of the YBCO film to the energetic argon ions. The exposed YBCO can be damaged to the extent of losing its superconductive properties, therefore, the “active” area of the junction will be much smaller than the nominal one. This effect becomes more important when reducing the size of the junctions. During this work, the edge erosion in the photoresist mask and the damage of the YBCO film were limited decreasing as much as possible the energy of the argon ions during the etching procedure.

#### 4.2. Mask making techniques: electron beam lithography

Electron beam lithography is a specialized technique for creating the extremely fine patterns. Derived from the early scanning electron microscopes, the technique consists in scanning a beam of electrons across a surface covered with a resist film sensitive to those electrons, thus depositing energy in the desired pattern in the resist film. The resolution this technology is capable of is very high, down to tens of nanometres. It is also very flexible and can work with a variety of materials and an almost infinite number of patterns. Nevertheless, it requires an expensive and complicated equipment and frequent service. The sub-micrometer biepitaxial junctions described in this work, with width in the range 0.6-1.5 $\mu\text{m}$ , were realized in the MC2 laboratories of the Chalmers University of Technology, where a strong knowledge in nanofabrication technology and physics of nanodevices has been established during the years. It has been the first time that such complex HTS structures were

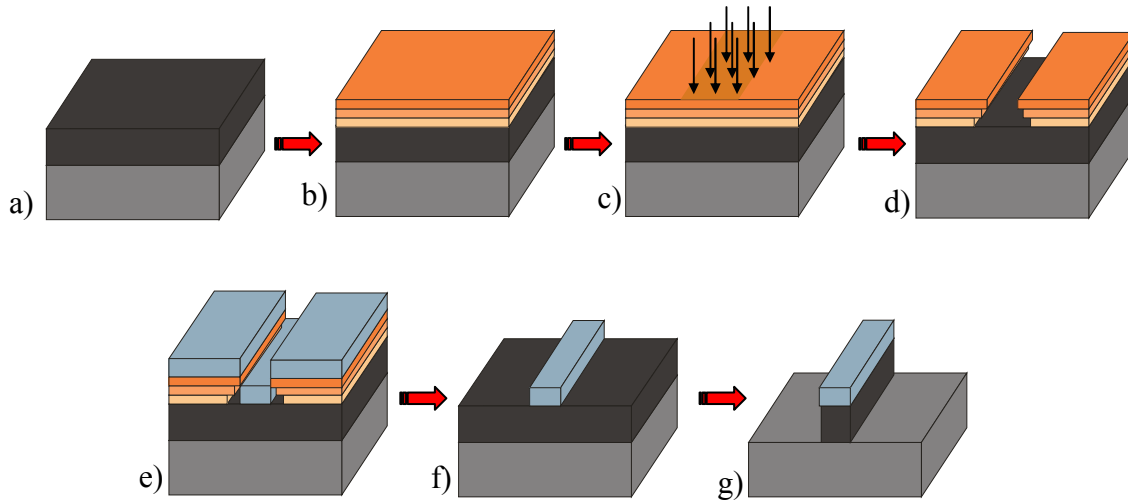


Figure 4.3 Steps of the mask realization procedure using e-beam and carbon technology. A carbon film is evaporated on the sample (a) and covered with three layers of e-beam resist (b). The resist is exposed (c) and developed (d) leaving an undercut. Then, a Cr thin film is evaporated (e). Through lift off (f) and subsequent plasma assisted removal of the carbon outside the Cr mask (g), the mask is transferred to the carbon layer.

realized using nanofabrication technologies (the HTS nanojunctions reported in the literature are mostly bicrystal structures [18, 25, 45, 46]). With this work the feasibility of such nanostructures was assessed, and the possibility to effectively use nanotechnologies in the HTS devices fabrication could open important perspectives in the field of superconducting electronics.

For the realization of sub-micrometer structures the process of mask making is not as simple as the one described in the previous paragraph. The problems related to the edge erosion of the resist mask become of primary importance when the size of the patterned structure decreases. In Chalmers an amorphous carbon mask technology has been developed [78]. The mask is transferred from the exposed resist to the carbon layer via lift off. The steps of this mask fabrication procedure are sketched in Figure 4.3 and they are the same both for the seed layer patterning and for the YBCO film. In the following sections of this paragraph a description of each process step will be given.

#### 4.2.1. Carbon deposition

The choice of carbon as mask material is due to its superior resistance to argon ions milling. Carbon proved to have an etching rate of  $\sim 0.60 \text{ nm/min}$  at  $0.1 \text{ mA/cm}^2$ ,  $500 \text{ eV}$ , and  $0^\circ$  incidence angle for a continuously running ion gun [78]. This etching rate is about ten times lower than for an electron beam resist. It has also a lateral resolution low enough for the realization of HTS junctions and small edge erosion. The redeposition of etched material in the mask shadow often occurring during the ion milling is also much less than for a resist mask because the carbon mask can be made significantly thinner thanks to its higher resistance. However, carbon is extremely sensitive to the presence of residual gases like  $\text{O}_2$ , which increases the etching rate by as much as 30%. A low background pressure in the vacuum chamber before starting the ion milling procedure is therefore of great importance for successful processing. On the other hand, the sensitivity to oxygen becomes a positive point when removing the mask since this can be easily accomplished with a low-power oxygen plasma that doesn't damage the sample but removes completely the carbon.

During this work the amorphous carbon layer has been deposited via the electron gun



evaporation technique described in section 3.4.1. Carbon belongs to that group of material for which evaporation is accomplished from a solid source. The purity of the carbon layer is of the outmost importance during this fabrication process. Any impurity, particle or trace of other materials in the carbon film could result in a damage or disuniformity in the carbon mask that would provide a non uniform coverage and protection during the ion milling procedure. A high level of vacuum was therefore reached in the evaporation chamber before starting the carbon deposition and a pre-evaporation of titanium, which acts like impurities getter was performed. The carbon was the deposited at about 1Å per second until reaching a thickness of 90nm.

#### **4.2.2. Electron beam resist**

In this work a positive electron beam resist system was used. Positive e-beam resist works, in principle, in the same way described in section 4.1 for positive photoresist, with the difference that it is sensitive to electrons in a certain energy range instead of UV light. The electron irradiation breaks polymer backbone bonds in the resist, leaving fragments of lower molecular weight. Later, the developer selectively washes away the lower molecular weight fragments, thus forming a positive tone pattern in the resist film. The patterning procedure used in this work requires a lift-off step (Figure 4.3e), for which it is important to create a large undercut in the resist profile. Therefore, a resist system composed of three layers of two different compositions was used:

- a first layer (bottom layer) of a copolymer of methyl methacrylate and methacrylic acid [P(MMA-MAA)]
- a middle layer of polymethyl methacrylate (PMMA) soft baked
- a top layer of PMMA

The developer used is a mixture of isopropanol and water in 14:1 ratio. The layers have different developing speed, the copolymer being developed more rapidly than the PMMA and the soft baked PMMA more rapidly than the hard baked one. In this way, a large undercut is produced, as showed in Figure 4.3d, that will allow good results for the lift off process and a chromium mask with sharp edges.

The baking is performed at the lowest temperature allowed for this type of resist, which is 135°C, in order not expose the YBCO film to the high temperature promoting oxygen loss and speeding reactions with water and CO<sub>2</sub>.

#### **4.2.3. Electron beam exposure**

In this section, the main issues connected to the exposure step of the electron-beam lithography (EBL) process are reported. Unlike photolithography, EBL doesn't make use of a mask for the pattern transfer to the sample, but this is directly written on the sample with the electron beam. We will give a rapid description of an EBL system will be given and of the issues related to the transmission of the pattern to the EBL machine.

##### ***Elements of an EBL system***

Figure 4.4a shows the block diagram of a typical EBL system and control electronics. The part of the system that forms the electron beam is called column. The column of the JEOL system used during this work is sketched Figure 4.4b. It consists of an electron source, lenses, alignment systems for centering the beam in the column, apertures for helping to define the beam, a blanker for turning the beam on and off, a stigmator for correcting any astigmatism in the beam, a mechanism for deflecting the beam, and finally, an electron

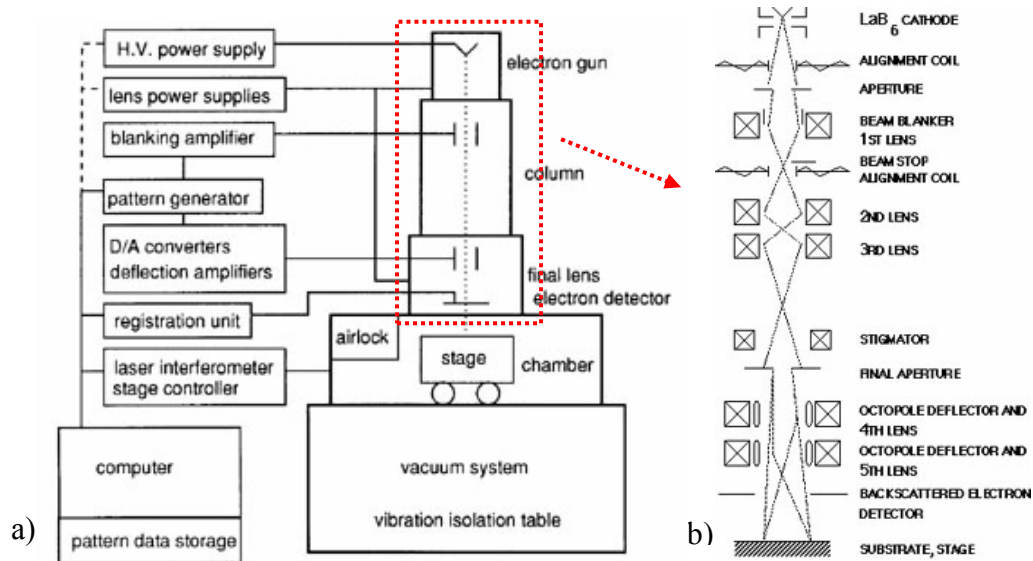


Figure 4.4 Sketch of the major components of a typical electron beam lithography system (a) and of the JEOL JBX-5DII system (b).

detector for assisting with focusing and locating marks on the sample [76, 79]. These components are described in the following.

- Electron source

Electrons may be emitted from a conducting material either by heating it to the point where the electrons have sufficient energy to overcome the work function barrier of the conductor (thermionic sources) or by applying an electric field sufficiently strong that they tunnel through the barrier (field emission sources). The most used solution in EBL systems is the first one. The JEOL system used in this work is equipped with a lanthanum hexaboride source. Three key parameters of the source are the virtual source size, its brightness, and the energy spread of the emitted electrons. The size of the source is important since determines the amount of demagnification the lenses must provide in order to form a small spot at the target. Brightness can be compared to intensity in light optics, so the brighter the electron source, the higher the current in the electron beam. A beam with a wide energy spread (which is undesirable, as will be shown later when dealing with electron lenses) is similar to white light, while a beam with a narrow energy spread would be comparable to monochromatic light.

- Electron lenses

Electron lenses behave in principle the same as optical lenses, with the differences that electron lenses can be made only to converge, not diverge. Also, the quality of electron lenses is not nearly as good as optical lenses in terms of aberrations. In EBL systems, magnetic lenses are often used. They are formed from two circularly symmetric iron (or some other high permeability material) polepieces with a copper winding in-between (Figure 4.5a). The divergence of the magnetic flux imparts a force on electrons back towards the optical (Z) axis, resulting in focusing action. The magnetic field also causes a rotation of the electrons (and the image) around the Z axis in a corkscrew fashion. Although this does not affect the performance of the lens, it does impact the design, alignment, and operation of the system. The EBL system used in this work has two final objective lenses (4<sup>th</sup> and 5<sup>th</sup> lens in Figure 4.4b); only one can be used at a time depending on the beam diameter needed. In this work, for example, the contacts area of the YBCO pattern requires less resolution than the bridge's area. Therefore, in order to

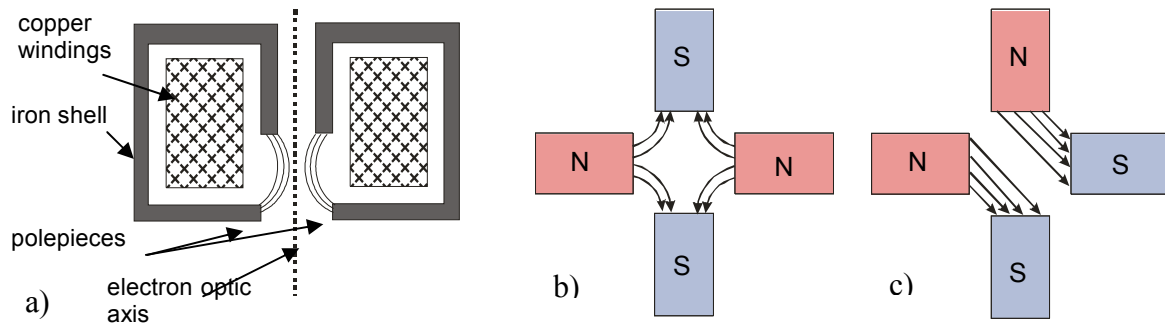


Figure 4.5 Some EBL system components: cross section through magnetic lens (a), magnetic field distribution for a stigmator (b) and a simple beam deflector (c)

optimize the process, the exposure was divided in two parts, the first was carried out with the 5<sup>th</sup> lens and low current to expose the small bridges, the second at higher current with the 4<sup>th</sup> lens and a larger filed size for the contacts areas.

- Apertures

Apertures are small holes through which the beam passes on its way down the column. They may be used to stop any stray electrons without affecting the beam itself or turn the beam on and off, as for the blanking apertures. A beam limiting aperture has two effects: it sets the beam convergence angle (measured as the half-angle of the beam at the target) through which electrons can pass through the system, controlling the effect of lens aberrations and thus resolution, and also sets the beam current. In Figure 4.6 the effects of the three apertures on the beam diameter in the JEOL JBX 5DII system are shown.

- Blanker

Turning the beam on and off is usually accomplished with a pair of plates set up as a simple electrostatic deflector. One or both of the plates are connected to a blanking amplifier with a fast response time. To turn the beam off, a voltage is applied across the plates which sweeps the beam off axis until it is intercepted by a downstream aperture.

- Stigmator

A stigmator is a special type of lens used to compensate for imperfections in the construction and alignment of the EBL column. These imperfections can result in astigmatism, where the beam focuses in different directions at different lens settings; the shape of a nominally round beam becomes oblong, resulting in smeared images in the resist. The stigmator cancels out the effect of astigmatism, forcing the beam back into its optimum shape. Stigmators may be either electrostatic or magnetic and consist of four or more poles (eight is typical) arranged around the optical axis (Figure 4.5b).

- Electron beam deflectors

Deflection of the electron beam is used to scan the beam across the surface of the sample. As with lenses, it can be done either magnetically or electrostatically. The coils or plates are arranged as shown in Figure 4.5c. Deflecting the beam off axis introduces additional aberrations that cause the beam diameter to deteriorate, and deviations from in plane linearity increase as the amount of deflection. These effects limit the maximum field or deflection size that can be used.

- Backscattered electrons detector

Some steps of the exposure, such as focusing, deflection calibration, and alignment marks detection, require the possibility to image the sample's surface. Unlike scanning electron microscopes, which image with low voltage secondary electrons, EBL systems normally detect high energy backscattered electrons since these electrons can more easily penetrate the resist film. The signal from low energy secondary electrons may be also obscured by the resist.

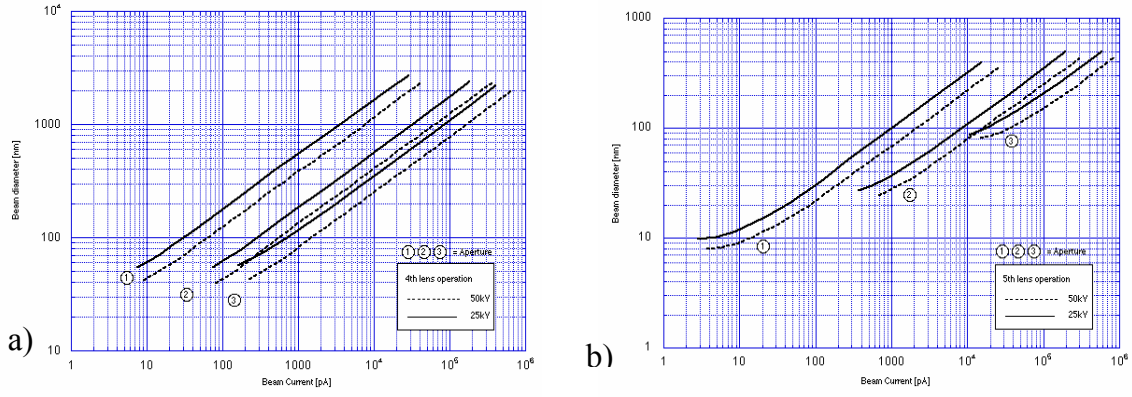


Figure 4.6 Beam diameter vs. beam current for the three apertures of the JBX-5DII system when using the 4<sup>th</sup> lens (a) or the 5<sup>th</sup> lens (b)

## Resolution

There are several factors that determine the resolution of an electron beam system. First is the virtual source size  $d_v$  divided by the demagnification of the column,  $M^1$ , resulting in a beam diameter of  $d_g = d_v / M^{-1}$ . If the optics of the column were ideal,  $d_g$  would be the beam diameter. Unfortunately, lenses are far from perfect. Spherical aberrations result from the tendency of the outer zones of the lenses to focus more strongly than the centre of the lens. The resultant diameter is  $d_s = 1/2 C_s a^3$ , where  $C_s$  is the spherical aberration coefficient of the final lens and  $a$  is the convergence half-angle of the beam at the target. Using an aperture to limit the convergence angle thus reduces this effect, at the expense of reduced beam current. Chromatic aberrations result from lower energy electrons being focused more strongly than higher energy electrons. For a chromatically limited beam, the diameter is  $d_c = C_c a DV / V_b$ , where  $C_c$  is the chromatic aberration coefficient,  $DV$  is the energy spread of the electrons, and  $V_b$  is the beam voltage.

Finally, quantum mechanics gives the electron a wavelength  $L = 1.2 / V_b^{0.5}$  nm; although much smaller than the wavelength of light, this wavelength can still limit the beam diameter by classical diffraction effects in very high resolution systems. For a diffraction limited beam, the diameter is given by  $d_d = 0.6L / a$ . To determine the theoretical beam size of a system, the contributions from various sources can be added in quadrature:  $d = (d_g^2 + d_s^2 + d_c^2 + d_d^2)^{0.5}$ .

## Mask data preparation and patterns alignment

In EBL lithography no mask is used and the electron beam is directly scanned over the sample surface. To guide the electron beam, the desired pattern is drawn, then it is converted in a format suitable for the EBL machine to read.

When drawing a pattern for EBL, the writing procedure of these machines has to be considered. Since the deflecting range of the electron beam is limited, EBL systems use the vector scan method illustrated in Figure 4.7, in which patterns split into fields and sub fields. The beam is rastered in the sub field filling the shape, then it is moved to the next sub field. Between shapes the beam is turned off (blanked) and is deflected in a direct vector to the next shape. When the shapes in all the sub fields have been exposed, the sample is moved and the next field is processed.

A computer aided design (CAD) program is usually used to lay out the pattern and to generate output in a standard exchange format. A separate program is then used to convert the intermediate format to machine-specific form. This last step can be quite involved since in

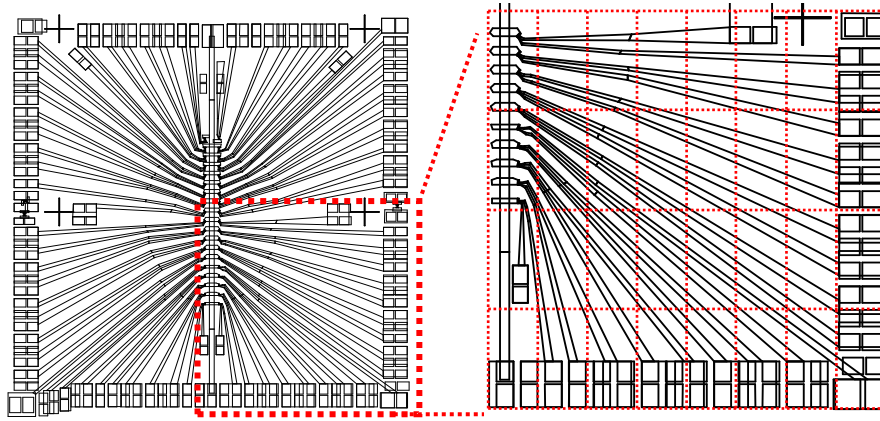


Figure 4.7 Example of the vector-scan writing strategy: the patterns are split into fields and sub fields and the stage moves from one to another,

most cases polygons must be reduced to primitive shapes (e.g., trapezoids or triangles and rectangles), and the pattern must be fractured into fields, subfields, and even sub-subfields. In the case of the EBL system used in this work, for high resolution patterns the writing field is as small as 80 nm. Larger patterns are formed by moving the sample and stitching fields together and field stitching errors will be around 20 nm, so while drawing the pattern one should take care that any fine lines should not be placed at a field boundary.

Another issue to be considered is the alignment. In photolithography, the alignment is made manually, positioning the sample under the photomask in such a way that the alignment markers of the mask coincide with the ones previously patterned on the sample. In EBL the procedure is more complex. For the seed layer, whose pattern has to be simply positioned at the centre of the sample, the alignment was made by calculating from the corners position, observed using the backscattered electrons detector described in the previous section, the coordinates corresponding to the centre of the sample and giving these coordinates as zero position for the pattern. For the YBCO pattern alignment, instead, gold marks were used. The best tolerance is achieved when the alignment marks are within several hundred micrometers of the critical region, in our case the bridges region. Therefore, gold alignment marks, in the form of crosses were defined in the protecting layer covering the YBCO before the EBL patterning. This requires a photolithography step, during which the gold pattern is manually aligned with the seed layer markers, and an ion milling step in which the gold layer is made thinner with except to the resist covered crosses area. The gold markers will be visible under the EBL system thanks to the difference in height that generates contrast with the background. Then, the coordinates of the crosses is used as a reference to position the YBCO pattern. The manual alignment of the gold markers with the seed layer ones determines the quality of the YBCO pattern alignment, therefore is a very delicate step. During the mask preparation, this issue has been taking into account drawing junctions' bridges long enough that could compensate for misalignments up to 1  $\mu\text{m}$  in both x and y direction.

Besides the pattern description, in an EBL procedure there are also two files containing information about the exposure conditions: the Jobdeck Definition file (.jdf) and the Schedule Definition file (.sdf). The jdf file describes the layout and the order of execution and what calibration routine to be used; the sdf file describes the working conditions (holder, sample position, accelerating voltage). With EBL technology it is possible to expose several samples also with different patterns during the same run; the positions of the samples and the patterns to assign each of them are specified in the sdf file.

#### 4.2.4. Mask transfer to the carbon layer

After the exposure, the pattern is developed by dipping in a solution of isopropanol and water. The optimal developing duration has to be enough to allow the undercut to fully develop but not too long, as there is the risk to overdevelop the resist upper layers and create a faceted pattern.

The positive pattern created has, then, to be transferred to the carbon layer to create the carbon mask for the ion milling etching. A chromium metal layer serves as an intermediate etching mask when the circuit pattern is transferred.

The chromium film is realized with the electron beam evaporation method. The film has to be thick enough to serve as a robust mask and not too thick or it will not possible to etch it away during the following ion milling and to remove the mask after the etching. During this work, 20nm thick films were used.

The next step of the procedure is the lift off (Figure 4.3f). It is performed in acetone. If the developing of the resist has been made properly and large undercut is present, the lift off process will be very quick and no chromium will be left outside the mask. When the undercut is not properly developed, on the other hand, residual chromium will be left and instead of having sharp edges, the mask will show chromium flakes along them. Since the edges of the mask are the areas where the grain boundary will grow, residual chromium in these areas means that the whole sample as to be discarded.

The final step of the mask transfer is the removal of the carbon outside the chromium layer. This is accomplished with a high oxygen pressure plasma etching. This technique is based on low power plasma generated at relatively high pressure (in our case 50W and 100mTorr of O<sub>2</sub>). The plasma creates oxygen ions that reacts with the carbon atoms producing CO and CO<sub>2</sub> that are subsequently pumped away from the chamber [76]. Since the energy of ions in the plasma is quite low, and their mean free path is much less than the chamber size, the etching process depends only on the chemistry of the plasma and not on the mechanical action of the ions, as occurring in the ion milling process that will be described in the next paragraph. Moreover, the plasma etch keeps the mask shape and does not damage the chromium mask nor the sample surface, the final result is thin layer of chromium on a carbon mask. The sample is finally ready for the ion milling process.

#### 4.3. Ion milling

The ion milling technique uses the same sputtering principles explained in the beginning of section 3.4.2 with the difference that, this time, the target to be eroded is the sample. Ion milling has the significant advantages in terms of directionality and, since the erosion rate is not much dependent on the specie, it can be used to treat quaternary systems as YBCO.

The basic components of an ion gun are showed in Figure 4.8a. A tungsten filament, acting as a cathode, is heated using a voltage  $V_f$ . The electrons produced are accelerated toward the anode. On the way, they impact the argon atoms introduced in the chamber and ionize them. A grid held at a voltage  $V_g$  accelerates the ejected ions toward the target where they will impinge removing the material not protected by the mask.

Ions arrive at the target surface with an energy given by

$$E_{ion} = q|V_p - V_g| = q|V_a + V_{pa} - V_g|$$

where  $V_p$  is the plasma voltage with respect to ground,  $V_a$  the difference between  $V_f$  and the anode potential and  $V_{pa}$  the plasma voltage with respect to the anode. The latter quantity is only a few volts because of the large anode area (all the chamber acts as anode). Therefore, the

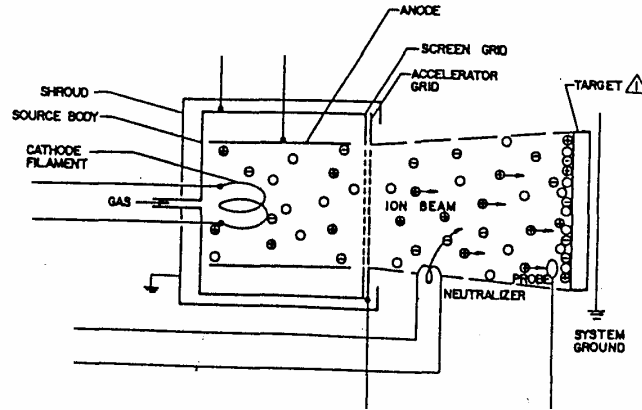


Figure 4.8 Sketch of an ion gun with its main components

extracted ion energy is controlled by changing  $V_a$  and  $V_g$ . Other parameters to be tuned to optimize the ion milling procedure are the argon gas pressure and the sample distance from the ion source and the tilt of the sample stage. Low beam current and voltage have been used for the etching of the YBCO film to reduce the damage to the smaller bridges. The etching parameters, both for CeO<sub>2</sub> and YBCO are showed in Table 4-1.

At the same power level, etching rates tend to be lower, by more than an order of magnitude, than film deposition rates. This means that etching requires high power levels. The combination of high power levels and long etching times cause samples to reach high temperatures. This is a point of the outmost importance when realizing YBCO devices, since the edges of the superconducting film can be severely damaged because the temperature-enhanced loss of oxygen, and in the damaged areas the film will lose its superconducting properties. The depth of these areas depend on many factors, such as the mask quality, the ion milling angle and above all on the parameters used for the ion milling procedure. The damage depth is a limiting parameter in the junction's width reduction; a better controlled ion milling process allows for the realization of narrower junctions. The use of YBCO thicker films, in the range 150-200nm, as used in this work, is also believed to help the realization of narrower junctions, since the film will contain enough oxygen to self-heal the oxygen loss at the edges [80, 46].

During the realization of the biepitaxial junctions described in this work the heating of the sample under ion milling was limited in two ways: alternating milling runs with pauses to allow the cooling of the sample and, in the case of YBCO etching, cooling the sample holder with cold water or gas. In the ion milling system of the University of Naples laboratories, in particular, the sample is glued to a copper cold finger inside which nitrogen gas circulates. The gas is introduced through a spiral copper tube immersed in liquid nitrogen. The efficiency of this system is such that the sample stage reaches temperatures down to 160K.

Etching parameters	CeO <sub>2</sub>	YBCO
beam current	Naples: 10mA Chalmers: 7mA	Naples: 8mA Chalmers: 5mA
beam voltage	Naples: 500V Chalmers: 300V	Naples: 400V Chalmers: 300V
sample holder cooling	no	Naples: LN2 (160K) Chalmers: water (9°C)

Table 4-1 Etching parameters for CeO<sub>2</sub> and YBCO films. Slightly different parameters were used for YBCO etching in Naples and Chalmers.



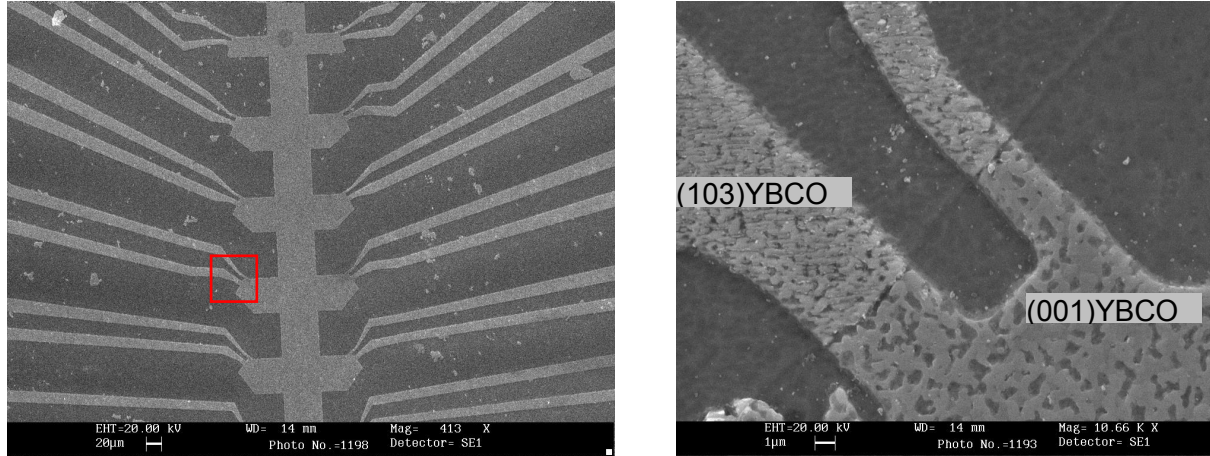


Figure 4.9 SEM images of biepitaxial junctions realized during this work. The widths of the bridges are 5.5 and 2.5 $\mu\text{m}$ .

## 4.4. Results

In this sections, the results of the junctions fabrication procedure will be shown with the help of SEM and AFM images. The transport properties of the devices will be described in detail in the chapter 6.

### 4.4.1. Micrometric junctions

Figure 4.9 shows some SEM images of a first batch of junctions 5.5 and 2.5 $\mu\text{m}$  wide realized using photolithography. During this work, the photolithographic process originally set up has been improved with excellent results in the increase in the samples lifetime. The realization of high quality  $\text{CeO}_2$  and YBCO films, as described in the previous chapter, a careful tuning of the ion milling parameters, for example, allowed for a drastic reduction in the junctions disuniformity. A higher yield in junctions' production was also reached, decreasing to just a few units the not working junctions on each chip. Samples realized during this work have shown durability and little modification in their transport and superconducting properties even after some years and tens of cool downs. This is an important achievement in the view of electronic application of HTS devices.

### 4.4.2. Sub micrometric junctions

It is worth to stress that the biepitaxial structure is significantly more complex than the bicrystal one, requiring one more patterning step and the growth of the YBCO film on a structured substrate. The higher complexity of the realization procedure is paid off by the higher versatility of these junctions and by the unique barrier properties. The efforts made to realize biepitaxial junctions in the sub-micron regime are justified by the interesting output of studies on transport in biepitaxial junctions' nano-channels and by the prospect of a better exploitation of the biepitaxial junctions' properties.

During this work, junctions with different width, from 0.6 to 1.5 $\mu\text{m}$ , and different thickness of the YBCO film were realized. In Figure 4.10 AFM images of 1.3 and 0.6 $\mu\text{m}$  wide junctions are shown. The cross section along the line in Figure 4.10c gives a width of  $\sim 0.65\mu\text{m}$ . The slope showed by the edges of the bridge in Figure 4.10d is due in part to the finite radius of the AFM tip.



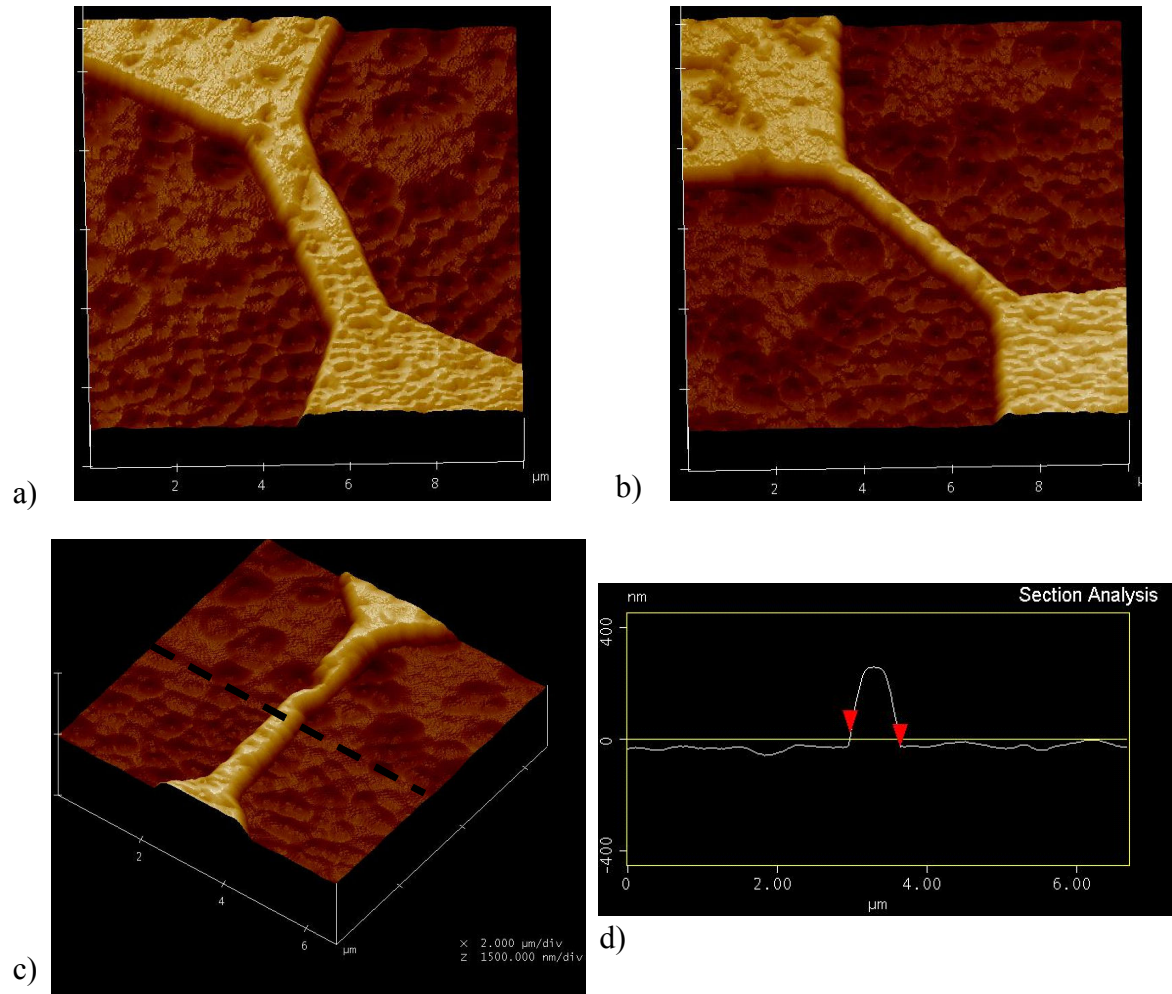


Figure 4.10 AFM images of biepitaxial junctions realized with electron beam lithography: (a) 1.3 μm junction with  $\theta=20^\circ$ , (b) 0.6 μm junction with  $\theta=45^\circ$ , (c) 0.6 μm junction with  $\theta=0^\circ$ , (d) profile of the junction showed in (c) along the line indicated. The slope of the bridge is due also to the finite radius of the AFM tip. The thickness of the YBCO film is ~120 nm for all the junctions. In the images is also possible to recognize the two different growth of the YBCO film.

In all the images, it is possible to clearly distinguish the two different growth of the YBCO film. In the top panels, for example, the elongated (103) grains are visible in the bottom right corner and the flatter (001) in the top left one. In conclusion, the AFM analysis performed at the end of the fabrication assesses the high structural quality and uniformity of the junctions' bridges. regimes.

## 5. *Measurement system and techniques*

The characterization of the biepitaxial junctions realized during this work was carried out in the University of Naples laboratories using a Heliox  $^3\text{He}$  system to reach temperatures down to 0.3K. This chapter is dedicated to the description of the measurements equipments and strategy, with particular attention to the improvements made during this work. Great efforts have been dedicated to noise reduction in the measuring strategy, shielding from external magnetic field and thermal coupling of the sample to the cooling unit. These improvements allowed the realization of the high quality/low noise measurements that will be described in the next chapter. The samples characterization and the continuous improvement of the measuring system and technique is the counterpart to the improvements to the fabrication procedure. This is again meant to highlight some technologically issues that have been faced during these 3 years in the spirit of a PhD program bridging engineering and physics.

### 5.1. *$^3\text{He}$ refrigerators description and operation*

Liquid nitrogen and helium are routinely used to reach the low temperatures needed for superconducting systems by simple immersion of the measuring inset in the liquid. The possibility to reach temperatures lower than the 4.2K of the liquid helium, on the other hand, opens the way to the investigation of more subtle phenomena and, when the temperature is low enough to “freeze” the quasiparticles noise, also of quantum effects. A series of refrigerators are now commercially available to reach ultra low temperatures. They use in different ways the peculiar properties of helium ( $^4\text{He}$ ) and of the valuable lighter isotope  $^3\text{He}$ , reaching temperatures slightly below 0.3K.

$^3\text{He}$  refrigerators operate by condensing a small charge of  $^3\text{He}$  and then pumping on it to reduce its vapour pressure. The decrease of the  $^3\text{He}$  vapour pressure down to about  $10^{-3}$  mbar brings a decrease in temperature, down to 0.3K, as it can be seen from the vapour pressure versus temperature graph in Figure 5.1. The pumping power needed to reach such a pressure is provided by a sorption pump. They rely on the dispersion forces existing between a gas and a surface to bind gas molecules on chilled surfaces inside the pump (cryosorption). In  $^3\text{He}$  refrigerators they consist of a cylindrical body filled with zeolite, a highly porous material with a surface to volume ratio of about 800 square meters per cubic centimetre. Zeolite particles are, in fact, characterized by molecular sized cavities linked by pores of a few Ångstrom of diameter that can trap gas molecules, in this case helium. The number of gas molecules that can be held on a given zeolite surface depends on the temperature. Practically, a sorb in a  $^3\text{He}$  refrigerator is designed so that at  $\sim 10\text{K}$  almost all of the  $^3\text{He}$  gets adsorbed, whereas at  $\sim 30\text{K}$  all the molecules desorb.

Figure 5.2a shows a sketch of a typical  $^3\text{He}$  system and its main working parts. The sample is mounted on the  $^3\text{He}$  pot at the bottom of the system, in a sample holder providing the electrical connections. The inset is closed with a brass shield and vacuum is realized inside the inner vacuum chamber (IVC) to provide isolation from the main liquid helium bath. The cooling to the base temperature of 0.3K takes place in three phases.

- From 300K to 4.2K

The first step of the cooling procedure is carried out by immersion in a liquid helium bath. The thermalization of the system is assured by a small amount of exchange helium gas previously inserted in the IVC.

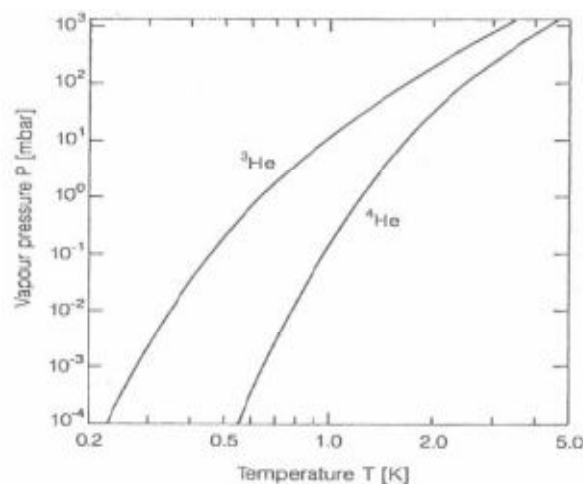


Figure 5.1  $^3\text{He}$  and  $^4\text{He}$  vapour pressure versus temperature.

- From 4.2K to 1.3K  
The condensation of the  $^3\text{He}$  gas takes place at temperatures below 2K. This temperature is achieved by pumping on liquid  $^4\text{He}$  extracted by the bath and contained in the 1K pot. From Figure 5.1 it is possible to see that to reach temperatures of about 1.3K a  $^4\text{He}$  vapour pressure of approximately 1 mbar is needed. The 1K pot is therefore connected to a rotary pump and the pumping power is regulated via a needle valve. During this phase of the cooling process the sorb is heated and kept at 35K. At this temperature, it will not absorb any  $^3\text{He}$ , therefore this can flow from the reservoir to the 1K pot, where it will condense, and then run down to cool the sample and the liquid  $^3\text{He}$  pot (Figure 5.2b). The system is kept in this condition for about 20 minutes to allow all the  $^3\text{He}$  gas to condense.
- From 1.3K to 0.3K  
At this stage, the  $^3\text{He}$  pot is full of liquid  $^3\text{He}$  at approximately 1.3K. The heating to the sorb is now switched off to allow the sorb to cool down. It will begin to reduce the vapour pressure above the liquid  $^3\text{He}$  so the sample temperature drops (Figure 5.2c). As the limiting pressure is approached, the temperature of the liquid  $^3\text{He}$  can be reduced to below 0.3K. The minimum temperature reached during this work was 0.245K.

When reached the base temperature, the temperature of the sample can be controlled, in principle, in two ways: directly heating the  $^3\text{He}$  pot or by adjusting the temperature of the sorb. The first way, although more direct and simple in the regulation, is practically never used since the heat supplied directly to the liquid  $^3\text{He}$  would make it evaporate too quickly. If the sorb temperature is set between 10 and 35K, on the other hand, it is possible to control the pressure of the  $^3\text{He}$  vapour and thus the temperature of the liquid  $^3\text{He}$ . The temperature of the sorb is continuously adjusted by the temperature controller to assure the stability of the  $^3\text{He}$  pot temperature, and therefore of the sample's one.

## 5.2. Upgrading of the Heliox $^3\text{He}$ system

Many improvements have been brought to the standard Heliox  $^3\text{He}$  refrigerator to fit to our measurements' requirements and decrease the measurement noise. Some improvements have also been brought with the aim to increase the system versatility and to be able to characterize different types of devices and samples with low or high impedance.

When realizing such improvements, one has to be careful in keeping the thermal load of the system as low as possible, in particular to the  $^3\text{He}$  pot. The limited cooling power of this system translates in limited hold time at base temperature. Therefore, the thermal conductivity

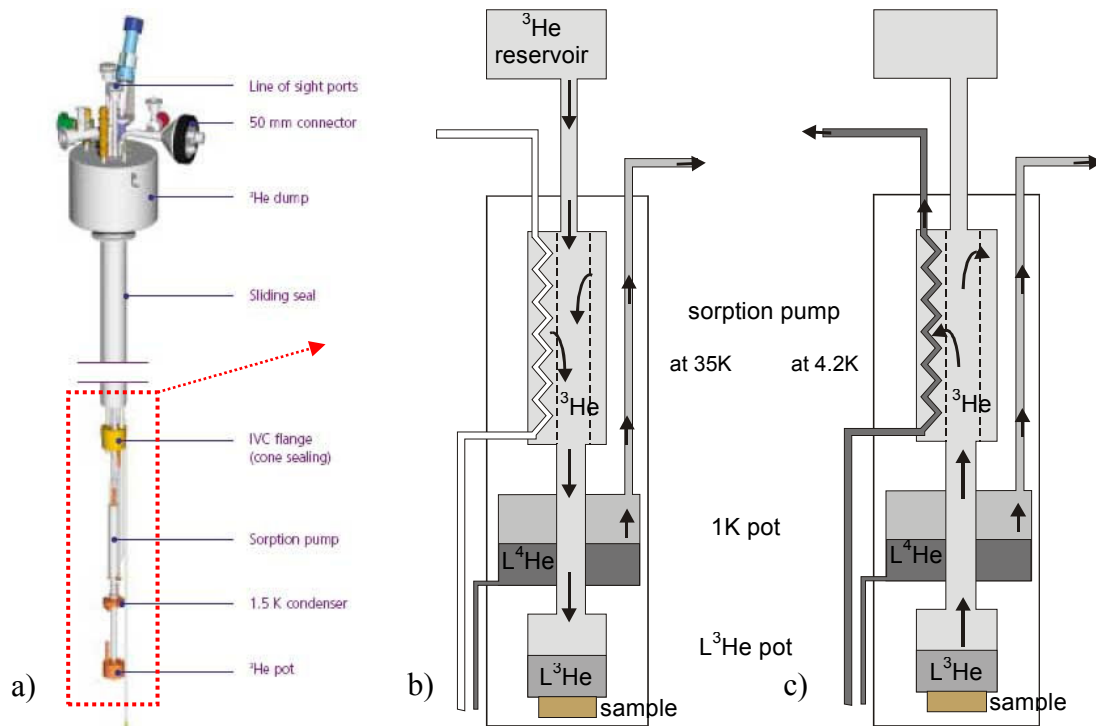


Figure 5.2 Sketch (a) and principle of operation of the  $^3\text{He}$  system during the condensing phase (b) and at base temperature (c)

of the materials used is of primary importance. Great care has also to be used in thermal anchoring of the wires and all the components to the various thermal stages in the system (4.2K, 1K pot and  $\text{L}^3\text{He}$  pot).

The original wiring of the system has been replaced with a higher performance one. Firstly, from room temperature to the 1K pot stage manganin and copper wires have been used. Manganin is the trademark of an alloy typically 86% copper, 12% manganese and 2% nickel; it is widely used in cryogenic measurements thanks to its low thermal conductivity (at low temperature, it is two orders of magnitude lower than the copper one) that helps in reducing the heat load to the refrigerating system. Nevertheless, its resistivity is higher if compared to copper, therefore we chose to use copper wires for the current carrying lines to avoid excessive heating, and manganin for the other lines. Each copper and manganin twisted pair has been inserted in a german silver capillar acting as a shield to external interference [81]. German silver, a copper, nickel and zinc alloy, was chosen for the easiness of working and, again, for its low thermal conductivity. From the 1K pot to the  $\text{L}^3\text{He}$  pot, instead, niobium–titanium superconducting wires have been used. The critical temperature of this alloy is 11K. The superconducting wiring is a very important improvement for this system. Thanks to it, we are able to bias the samples with higher currents without excessive heating.

The refrigerator was also equipped with a solenoid for the generation of magnetic field, which has been designed and fabricated in house. A superconducting Nb-Ti wire was used for the windings in order to generate high fields, up to 0.9Tesla with a current bias of 3mA, with low heating. This is an extremely high magnetic field compared with what is usually found in measuring systems designed for Josephson junctions based experiments. Thanks to the high performances of this solenoid, we were able to test the magnetic behaviour of ultra small junctions, as will be described in the next chapter. Another unique feature is the high uniformity of the generated field. This is achieved with a design in which the main coil is sided by two smaller ones, as sketched in Figure 5.3a. The field uniformity measurements are

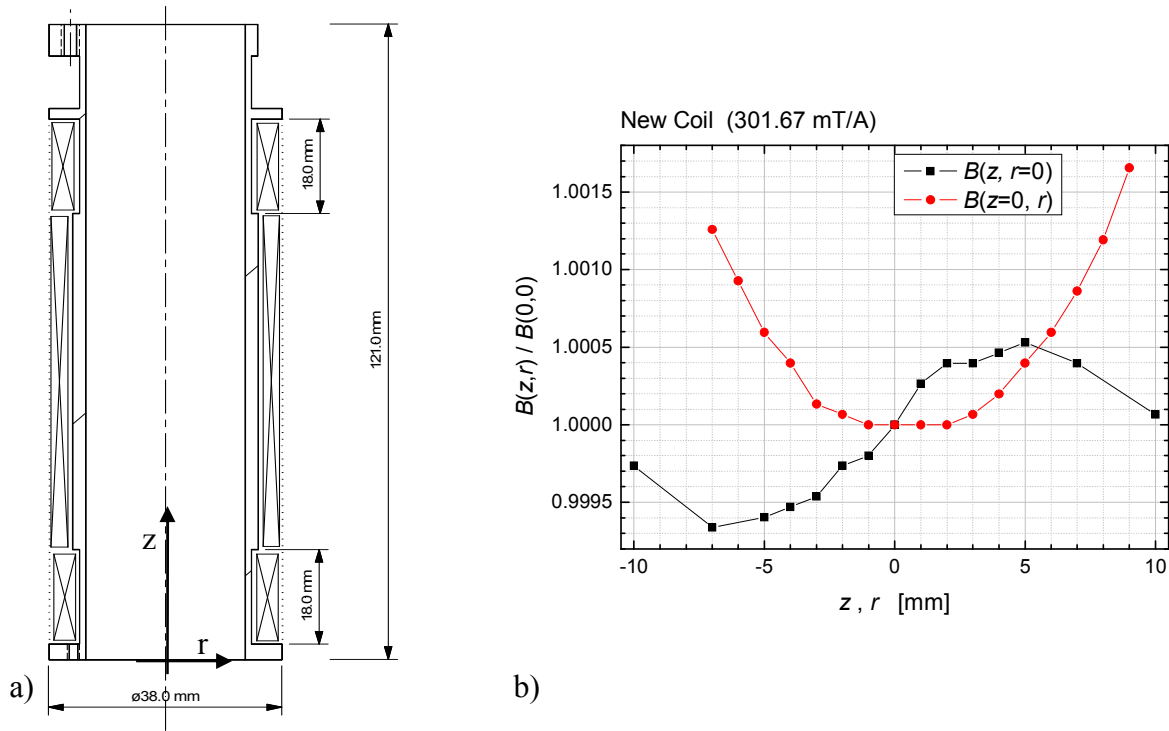


Figure 5.3 Sketch of the solenoid realized during this work for the generation of high, uniform magnetic field (a) and measurement of the field uniformity along the solenoid axes (black squares) and the radius (red dots).

shown in Figure 5.3b. The black squares represent the normalized field variation inside the solenoid along its longitudinal axes, whereas the red circles represent the variation of the field along the radius. The sample is positioned inside the solenoid at  $z=0$ . From the plot, it is possible to see that, for a 5x5mm area, that is in the sample's region, the field variation is in the order of  $10^{-3}$ . Finally, to allow operation also at high temperatures, the solenoid is thermally linked to the 1K pot. The temperature of the sample, that is of the  $^3\text{He}$  pot, is indeed independent of the 1K pot. Therefore, it is possible to drive the sample to high temperatures while keeping the 1K pot cold and the solenoid in the superconducting state. In this way the magnetic behaviour of samples can be measured at temperatures as high as 100K.

The sample is mounted, as already described, at the bottom of the  $^3\text{He}$  pot. To allow the electrical connection between the sample and the measuring system, the former is mounted on a chip holder. This has gold pads to which the junctions are connected with aluminium wire, bonded with ultrasound bonder machine. In Figure 5.4 one of the samples realized is showed as mounted on a chip holder and bonded. For obvious reasons, the chip holder is insulating. In these conditions, the cooling to the sample to ultra low temperatures comes not from the direct contact with the  $^3\text{He}$  pot but from the connecting wires. In the photo it is possible to see also a Cernox thermometer mounted on the top of the chip holder and bonded. It was added with the aim of measuring the temperature in a spot as close as possible to the sample.

At ultra low temperatures, the effective temperature of the sample is influenced also by the electrical noise brought by the connecting line with the external devices at room temperature. To remove this noise, filters have to be added to the electrical lines connecting the sample.

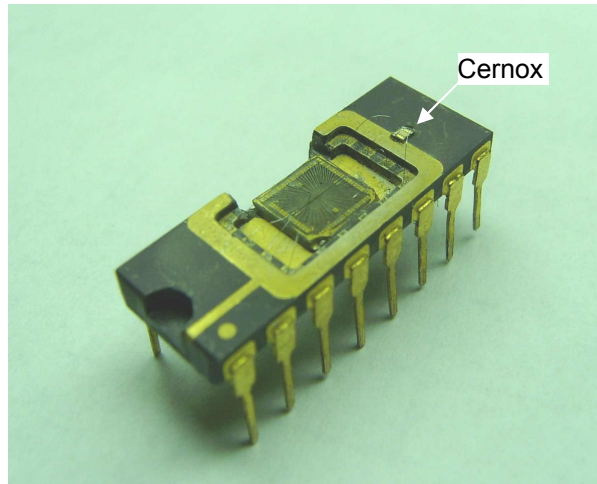


Figure 5.4 Photo of a chip mounted on the chip holder. On the right side of the chip holder a Cernox thermometer can be seen, bonded on the chip holder.

### 5.2.1. Cold filters

Filtering electrical lines connecting a room-temperature apparatus to an electronic device working at ultra low temperature is often of primary importance so that the desired effects are not hidden by thermal or environmental noise sources. Although a careful thermal anchoring of the electrical lines reduces the noise they generate themselves, it does not prevent the electromagnetic noise coming from parts at higher temperature from propagating along them. In Table 5-1 the conversion between the noise frequency and the temperature is shown. The effective thermalization of the device at a given temperature requires that this noise be sufficiently attenuated by filters.

The most effective way to filter a measurement system is to use several filtering stages at different temperatures. This strategy is needed to progressively filter the signal and to obtain an efficient cooling of the filters themselves [82]. During this work, two different types of filters have been realized and mounted on the  $^3\text{He}$  measuring unit both at the 1K stage and at the 300mK one. These filters are not commercially available, so they have to be designed and built on purpose. This requires, above all, a great deal of experience in the field of ultra low temperature and noise experiments. Moreover, filters intended to cut the higher frequencies of Table 5-1 are difficult to test since commercially available network analyser reach frequencies up to 10GHz. What happens to the filter response after this threshold can only be inferred from the improvement of the measurements' quality once the filter has been put in use.

Before describing the filters realized, it is worth mentioning also that the Heliox  $^3\text{He}$  system presents a problem when trying to mount electrical components, such as filters. This system was designed to be light and easy to handle, therefore it is very compact and the space inside the cold part is very limited. This requires particular design of the filters.

Frequency	Temperature
41.7MHz	1mK
4.84GHz	120mK
10.8GHz	260mK
41.7GHz	1K
175GHz	4.2K
3.2THz	77K
12.5THz	300K

Table 5-1 Frequency-temperature conversion table.



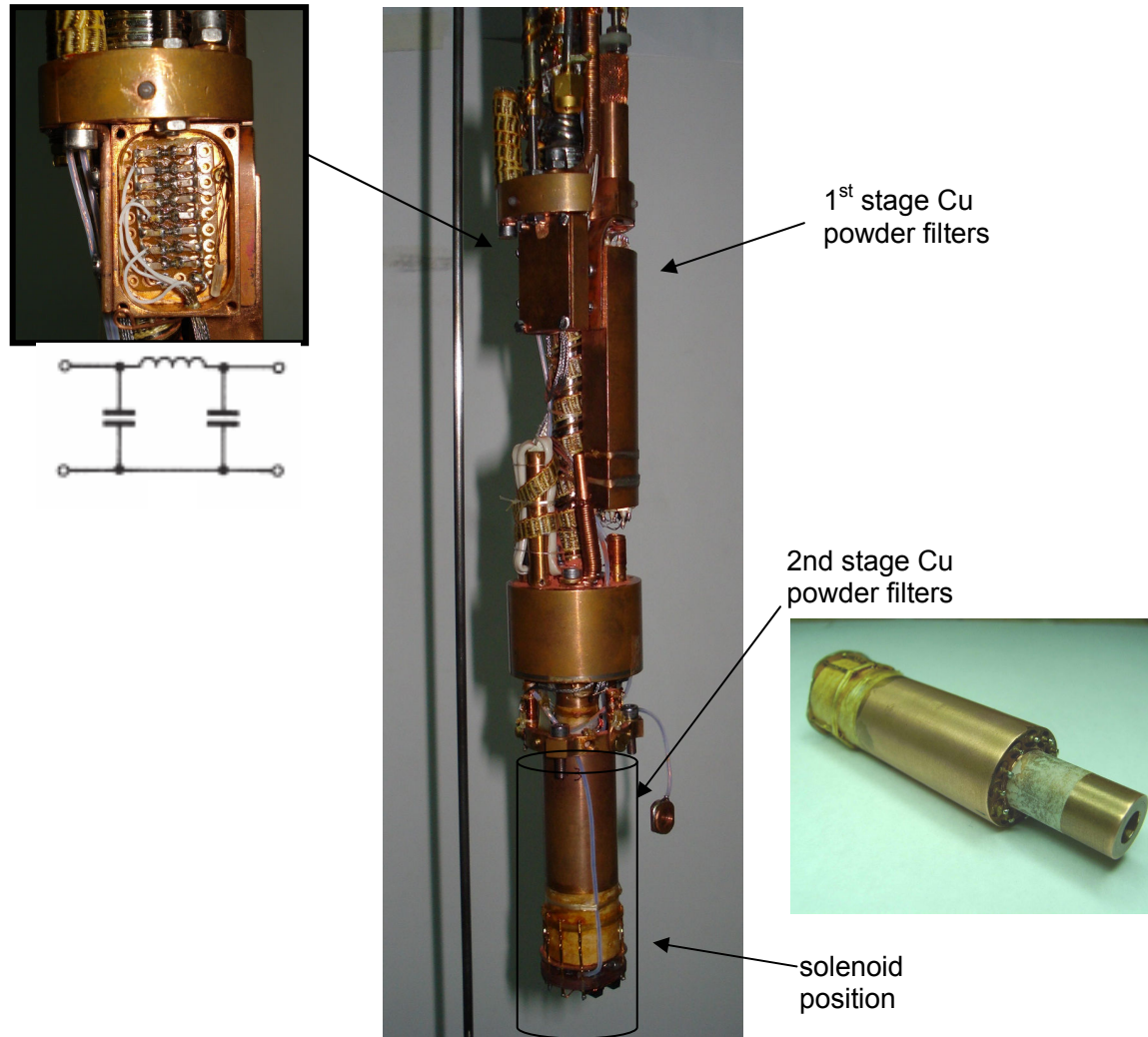


Figure 5.5 Filters mounted on the Heliox  $^3\text{He}$  system: pi-filters (left inset) and two stages of Cu-powder filters mounted at the 1K and 0.3K pots. The position of the bobbin is also indicated.

### ***Pi-filters***

The first filtering stage is composed of low pass  $\pi$  filters anchored to the 1K stage. They are showed in the left panel of Figure 5.5. A filter was realized for each measurement line with a  $100\Omega$  resistor and two  $1\text{nF}$  capacitors in parallel configuration. Everything is then enclosed in a copper box to allow good thermalization. From the values of the resistors and capacitors used a cut-off frequency of  $1.6\text{MHz}$  is obtained.

The main advantage of this type of filter is the possibility of filtering a large number of lines in a small volume. The disadvantage is the loss in attenuation at high frequencies due to the parasitic capacitance of the resistors.

### ***Cu powder filters***

The main improvement made to the Heliox  $^3\text{He}$  system has probably been the realization of an high frequency filtering system based on copper powder. These type of filters were first described by Martinis *et al* [83] and subsequently developed and discussed on more details by other groups [84, 85, 86]. They are used in experiments requiring the highest level of filtering, as for the to study of macroscopic quantum effects. They are realized with a spiral coil of insulated wire inside a tube filled with metal powder with a grain size that can go from  $5$  to  $30\mu\text{m}$ . Often copper powder is used, although some group report filters realized also with

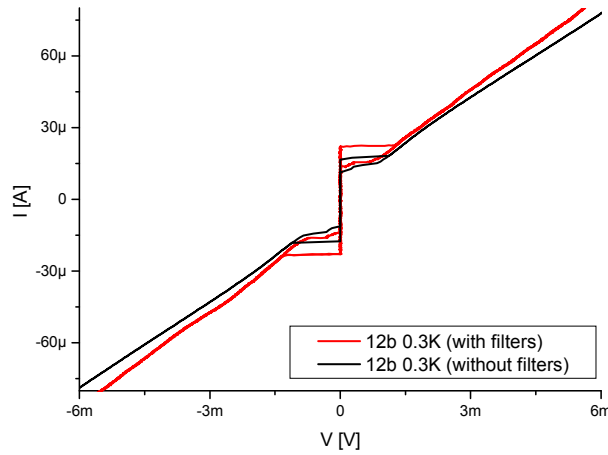


Figure 5.6 I-V characteristics of the same junction measured with Heliox system equipped with filters (red curve) and without filters (black curve)

stainless steel powder [84]. Since each grain of the powder is insulated from its neighbours by a naturally grown oxide layer, the effective surface area is enormous. The filter attenuates an incoming electrical signal via eddy current dissipation in the metal powder. The cut-off frequency of this type of filters is in the range of few GHz.

Cu-powder filters are quite complex and their design and realization requires deep knowledge of low noise measurement and cryogenics. They are also rather bulky; usually their length is in the range of tens of centimetres. Such a length is required to achieve a higher filtering of the measurement lines. These are the reasons why Cu-filters are commonly not mounted on  $^3\text{He}$  systems. During this work, instead, a new design was realized to fit two Cu-filters stages in the compact Heliox system.

The filters showed in Figure 5.5 measure 7 and 12 cm each and are anchored to the 1K stage and to the  $^3\text{He}$  pot respectively. In copper bulk pieces, suitably shaped, cylindrical holes were drilled, one for each measuring line, for a total of 12 lines. Manganin wires 50 cm were wound in spirals and inserted in the holes that were, then, filled with copper powder and sealed. In the final filter most of the powder is loose inside, this might help to reduce the stress in the filter during the cool down. In Cu-powder filters the cylinders are commonly sealed using connectors (usually of the SMA type) and the ends of the coils are soldered to the center pin. These connectors allow an easy mounting of the filter. This solution could not be used in our case due to the lack of space. Therefore, we screwed brass caps in the copper holes and the filter was connected to the lines by soldering.

The performances of the single stages were analyzed with a vector network analyzer, resulting in a cut-off frequency of 3GHz.

The effectiveness in reducing the measurement noise of the filters described can be shown comparing the measurements of the same junctions made with an Heliox system with no particular filtering and with the Heliox system used during this work. From Figure 5.6 it can be seen that the reduction in electronic noise brings an increment in the measured critical current of about 35%.

### 5.3. Measurement environment and strategy

All the measurements that will be shown in the next chapter were realized in a magnetically shielded environment. The shielding was provided by a system of superconducting and cryoperm screens. This system was built to fit in a measurement dewar to be filled with liquid helium and designed to provide an optimal screening in



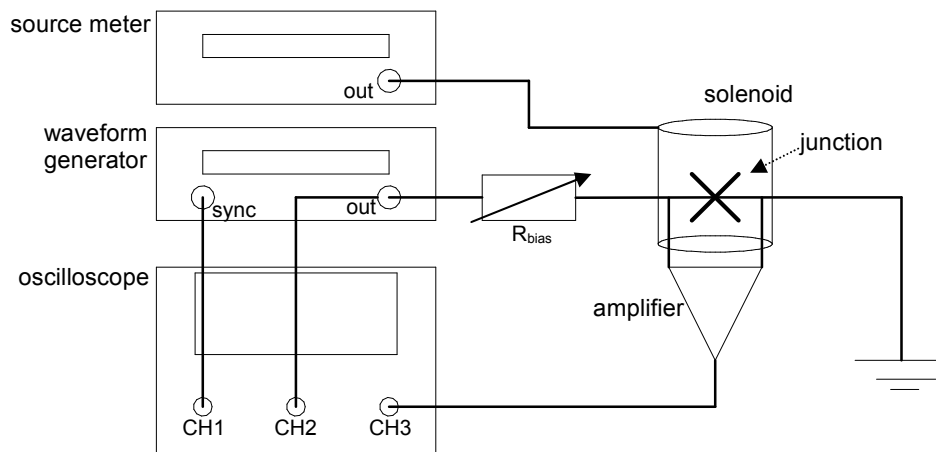


Figure 5.7 Measurement set up

correspondence of the region where the sample is positioned. The screens system is composed of two cryoperm screens 1mm thick as external screens, a lead screen of 1mm and a niobium screen of 0.1mm in the inner section. The combination of cryoperm and superconducting screens leads to a very high screening factor, calculated to be in the range  $10^{-5}$ – $10^{-6}$ . If only the superconducting screens were present, during the cool down of the screens the external magnetic field (as for example the earth magnetic field and the fields produced by electronic equipments) would be frozen inside the superconductors. Therefore, the cryoperm screens are added as external screens. On the other hand, a screening system made only with cryoperm would not be feasible, since the high magnetic fields produced by the solenoid used during our experiments would magnetize the material. Therefore, the superconducting screens are needed to “protect” the cryoperm.

It is worth remarking that it is not common to have such a good screening and, at the same time, a measurement solenoid capable to generate high fields, as the 0.9Tesla solenoid of our system. Usually, people are not concerned about the screening, when high fields are used. In optimizing both aspects, a more versatile system was realized.

The measurement set up used to measure the current-voltage characteristics of the junctions is shown in Figure 5.7. Other instruments can be added to this set up, for example lock-in amplifiers, to realize many types of measurements. However, the basic setup consists of:

- an Agilent 33120A wave form generator
- a LeCroy wave runner 6100A oscilloscope
- a Keithley 2400 source meter
- an Stanford Research System SP370 low noise current pre-amplifier
- different types of differential amplifiers build on purpose

The measurement strategy involves current biasing the junction under study and measuring the voltage signal. The bias is applied in the form of a triangular or sine wave from the Agilent wave form generator connected to a series resistor. By choosing different values of the resistor it is possible to bias the device in a wide range; the lower limit to the series resistor is represented by the resistance of the measurement lines. The signal from the sample is firstly sent to a battery driven amplifier. Different amplifiers were built during this work, to measure both high and low impedance samples. They can also be connected in series to reach

higher gains. For the Josephson junctions' measurements that will be shown in the next chapter, an amplification of 200 or 500 was usually found to be enough. The signal is then measured with a LeCroy oscilloscope and the data directly stored in it. For the magnetic field generation, the solenoid is biased with a Keithley source meter. In order to check the effective bias current, a low noise current pre-amplifier is sometimes added to the measurements set up.

All the instruments mentioned are decoupled from the laboratory electric lines using a transformer, to limit the external line disturbances influence on the measurement.

This set up and measurement strategy is also independent from a computer control, and does not require any measurement program to be written. This brings the possibility to change rapidly the measurement set up to perform new types of measurements and an overall increase of the measurement speed, since the communication step from the computer to the instruments is eliminated.

## 6. *Biepitaxial junctions' transport properties*

In this chapter the study of the transport properties of the devices fabricated with the techniques described in the chapters 3 and 4 will be shown. The devices are divided in three groups:

- $\text{LaAlO}_3$  (LAO) based micrometric junctions
- $\text{SrTiO}_3$  (STO) based micrometric junctions
- STO based sub-micrometric junctions

For each group, several samples, each containing 80 junctions, were realized. A large number of junctions is therefore available to carry out systematic and comprehensive studies.

For the first time, lanthanum alluminate has been used as a substrate material for the realization of biepitaxial junctions. The characterization of the first group of junctions will be shown to assess the feasibility of this technology.

As regards STO based junctions, their general characterization has been carried out extensively during the past years [11,19,27,29]. The aim of the present work has been therefore to improve the fabrication procedure, to gain a better control on the junctions' structure through an accurate tuning of the fabrication parameters and to increase the junctions lifetime and resistance to thermal cycling. Furthermore, we fabricated biepitaxial junctions down to  $0.6\mu\text{m}$  in order to investigate the sub-micrometer transport regime. It has been argued that different transport mechanisms can come into play when reducing the junctions width down to the mesoscopic range. An example is the experiment we will describe in chapter 6, on a self-protected nanometric channel. Also, Tzalenchuck and co-workers [46] found that, in ultra-narrow bicrystal junctions, the  $I_C$  does not scales proportionally with the junctions' width  $w$ . They identify two distinct regions, with different slopes, for the  $I_C$  vs.  $w$  behaviour, with the crossover almost exactly at  $1\mu\text{m}$ . They speculate that the narrow junctions region represents intrinsic properties of the junction barrier, while some other mechanism comes into play on the micrometer scale.

We plan to explore deeper the mesoscopic transport range exploiting the advantages of the biepitaxial structure. The realization procedure we implemented yielded high quality junctions whose magnetic behaviour points to single channel transport. Moreover, the directionality of the transport in biepitaxial structures was further proved by a tunnel spectroscopy experiment.

### 6.1. *Transport properties of LAO based junctions*

A standard characterization of HTS junctions involves the study of the current-voltage ( $I$ - $V$ ) characteristics of the devices as a function of the temperature, the applied magnetic field and the misorientation angle.

The study as a function of the temperature can give information on the nature of the junctions' barrier, the  $I_C(H)$  pattern is a fingerprint of the junction, from which a large number of information can be derived, as showed in section 2.3.2, especially on the  $d$ -wave effects and microstructure of the barrier. The study as a function of the junction angle is important to assess the directionality of the transport and the possibility to select the transport regime by selecting the junction orientation [11]. Finally, it is useful to evaluate the spread in the junctions parameters and compare these with the data available in the literature for other GB junctions structures.

In Figure 6.1 and Figure 6.2  $I$ - $V$  characteristics of two LAO based samples are shown. For clarity, only few representative junctions are shown for each sample. The  $I$ - $V$ s' often show hysteresis, as in the inset of Figure 6.2a; this is an indication of a low transmissivity

barrier, something desirable for many applications. The values of the critical current  $I_C$ , the critical current density  $J_C$ , the normal resistance  $R_N$ , the  $I_C R_N$  product and the  $R_N A$  product are reported in Table 6-1 for sample #140503 and in Table 6-2 for sample #160505. These products fall in the typical ranges for biepitaxial junctions: average critical current density is for both samples in the range of  $1 \div 3 \times 10^3$  A/cm<sup>2</sup> and the  $I_C R_N$  product is in the range of 1mA.

Junctions from the sample #140503 show, on the average, a lower  $I_C R_N$  value and an higher spread in many parameters, as for example the normal resistance  $R_N$ . Also the critical current density as a function of the misalignment angle (Figure 6.1d) does not always follows the behaviour predicted by the equation (2.2) (see section 2.3.1). These are indication of a disordered structure. The reasons for the lower quality of this sample are not certain. A possible explanation could be found in the fact that the preparation of this sample was delayed, and many months elapsed between the seed layer and the YBCO films deposition. It is likely that, with time, impurities are build on the surface of the CeO<sub>2</sub> film exposed to air, preventing an optimal growth of the YBCO film.

The temperature dependence of the  $I$ - $V$  curve and of the critical current showed in Figure 6.1b and c can be used as a tool to investigate the nature of the barrier in these junctions. In  $S$ - $N$ - $S$  structures,  $I_C(T)$  is expected to have an exponential-like dependence, modulated by the ratio between the coherence length in the normal layer ( $\xi_N$ ) and the barrier thickness  $L$ :

$$I_C(T, L) \approx \frac{2}{e\pi R_N} \frac{|\Delta_0|^2}{k_B T_C} \frac{L}{\xi_N} e^{-L/\xi_N} \quad (6.1)$$

This has been experimentally verified for low-temperature Josephson junctions, as widely discussed in all textbooks and extensive reviews [15, 16]. As regards HTS junctions, in Ref. [87] a collection of many experimental data available in the literature at that time is present. The authors noted an approximately linear temperature dependence of  $I_C$  over a wide temperature range, arguing that the  $S$ - $N$ - $S$  model is not valid for almost all HTS junctions, especially grain boundary junctions. Later, instead, it was found that, in biepitaxial junctions, the behaviour is not too far from classical  $S$ - $N$ - $S$  model [19]. The results of Ref. [19] are confirmed also for LAO junctions. In Figure 6.1c the LAO junctions data are qualitatively compared with the theory developed for  $S$ - $N$ - $S$  junctions and equation (6.1) assuming a ratio  $L/\xi_N$  of 8; the shape of the experimental curve is well reproduced. This confirms the claims of low transparency of the biepitaxial barrier, if compared to other types of GB junctions. As mentioned in section 2.4, a low transmissive barrier is an advantageous feature for electronic applications and an important positive aspect of the transport in biepitaxial structures.

As the magnetic behaviour of the junctions is concerned, Figure 6.2b shows a selection of  $I_C(H)$  patterns from sample #160505. Patterns referring to junctions with different misorientation angles (0, 30° and 65°) where chosen to highlight the changing of the pattern shape with the junctions' angle. It is very interesting to note that anomalous patterns are observed in correspondence of the minimum in  $J_C(\theta)$  or, in other words, in correspondence of those misorientation angles for which the transport direction faces a node of the order parameter of one of the electrodes. The more regular patterns are rather in the lobe versus lobe configuration. When the misorientation angle is such that the  $J_C$  is reduced, indeed, the short junction regime is approached and  $d$ -wave effects become more and more relevant also because of faceting [19]. This example shows that also in LAO junctions the transport properties are strongly influenced by the effects of the  $d$ -wave symmetry of the order parameter.

Furthermore, the patterns' periodicity gives information on the junctions' active width (see following section 6.2.2). In the case of the  $\theta=30^\circ$  junction, the active width is calculated to be in the micron range, whereas the geometrical width is  $5\mu\text{m}$ . This difference is due in part to lateral erosion occurring during ion milling, that damages the external YBCO layers, in part to the possible presence of insulating impurities that reduces the real junction width, as will be explained later in more detail in section 6.2.2. As the  $\theta=65^\circ$  junction is concerned, it can be seen that the pattern periodicity is the same for both the main and the secondary lobes. This happens when the junction's bridge contains more than one active channel, as for example the SQUID geometry [15]. This problem often occurs in micrometric-size junctions.

The microstructure of LAO based junctions is known to be more complex than STO based ones. LAO substrates presents twin boundaries. During the deposition of the YBCO film, they can rearrange and produce defects and cracks in the YBCO. It has also been reported that these boundaries could serve as nucleation points for defects in the YBCO film [88]. In other words, the boundaries represent a defect that propagates vertically in the YBCO layer. The defects induced in the YBCO film replicate the typical "zigzag" structure of the twin boundaries. In contrast to small localized defects, such as the microholes often found in YBCO films grown on STO substrates, the "zigzag" defects can extend also for a few micrometers. This is more detrimental to the transport properties of the junctions. If grown in correspondence of the grain boundary, they can add to the intrinsic faceting of the YBCO film and change in a random way the reciprocal misorientation of the two electrodes' grains.

Given these difficulties, the global good quality of the LAO junctions realized during this work is a very encouraging result in view of the relevant perspectives for experiments in presence of microwaves. However, a greater reproducibility and predictability of the junctions' properties is surely needed. A possible way to reduce the defects could be the use of a LAO substrate in which twinning is suppressed thanks to the addition of dopants such as Sr or torius, but the microwave properties are conserved. Microwave properties of YBCO films grown on  $\text{SrLaAlO}_4$  were indeed found to be comparable to the ones of YBCO grown on LAO [89].

## **6.2. Transport properties of STO based junctions**

STO based biepitaxial junctions have been deeply characterized in the past in a number of publications. The structure of the YBCO and of the seed layer films (both  $\text{CeO}_2$  and  $\text{MgO}$ ) has been extensively studied with x-rays diffractometry [29, 66], the one of the grain boundary with transmission and scanning electron microscopy [27, 63] and the possibility to tune the transport properties with the misalignment angle has been demonstrated [90]. Also, the layout of a superconducting device that could exploit this versatility and the possibility to use different material for the seed layer, has been proposed [27].

Analyzing the behaviour of the critical current density with respect to the misalignment angle, the  $d$ -wave symmetry of the order parameter has been for the first time demonstrated for junctions not inserted in any loop [11]. This experiment showed that in high quality biepitaxial junctions the transport direction is preserved, in spite of the disorder and impurities in the grain boundary.

More recently, these junctions helped in making another, very important, leap forward in the understanding of high temperature superconductivity and macroscopic quantum effects in HTS. For the first time, macroscopic quantum tunnelling and energy level quantization have been measured in an HTS junction [30, 31]. Therefore, despite the presence of nodes in the order parameter, source of quasiparticles, macroscopic coherent behaviours is possible also in HTS junctions, with the right structure and an high quality factor.

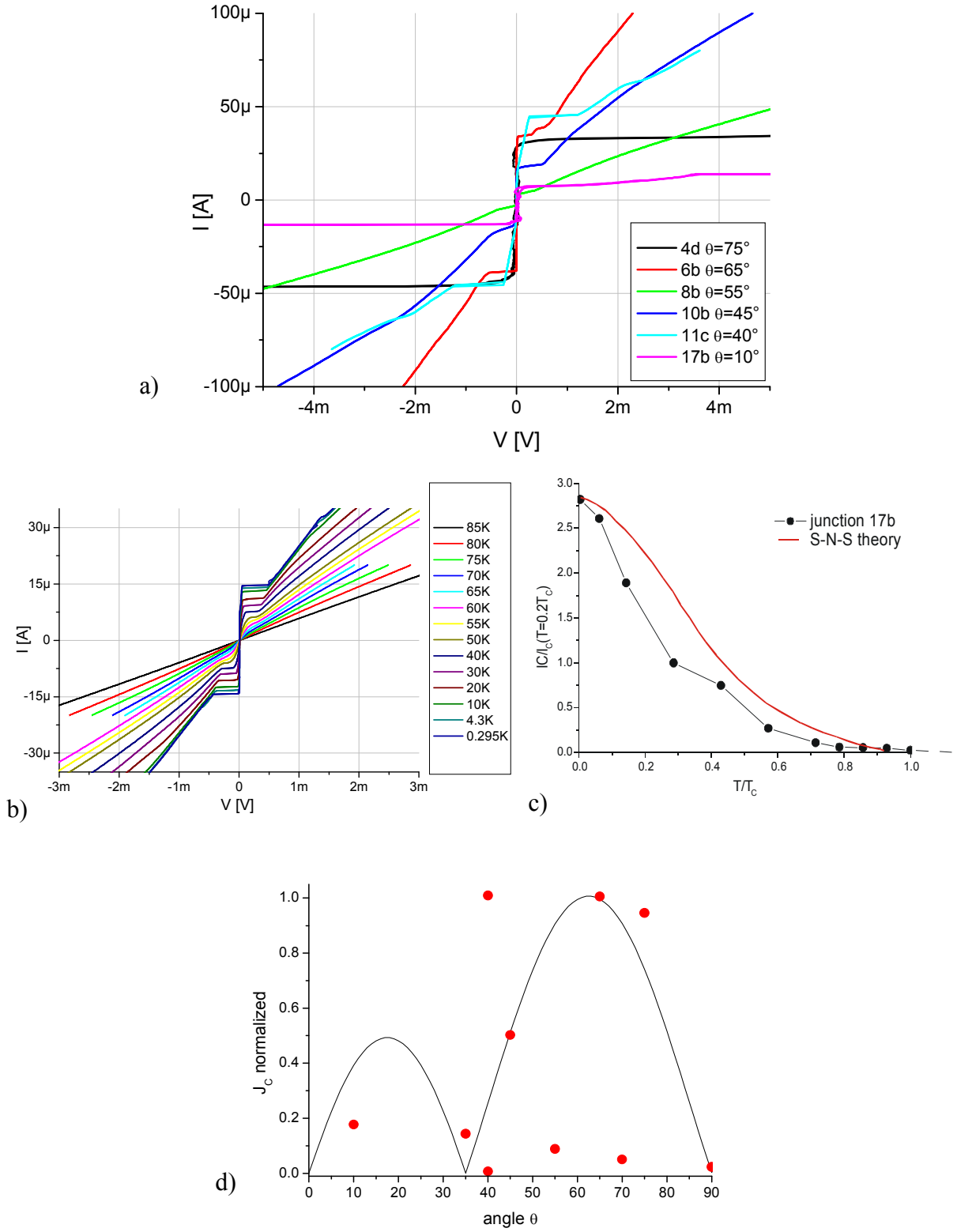


Figure 6.1 Transport properties of LAO based sample #140503:  $I$ - $V$  characteristics of some representative junctions at  $T=0.3\text{K}$ . “a” and “c” junctions are  $2.5\mu\text{m}$  wide, “b” and “d” are  $5\mu\text{m}$  wide (a),  $I$ - $V(T)$  curves of junction 17b ( $\theta=10^\circ$ ) (b) and the extracted  $I_C(T)$  behaviour compared with the S-N-S theory for proximity assisted transport, assuming  $L/\xi_N=8$  (c);  $J_C$  versus misalignment angle  $\theta$  (d). In the plot (d) the  $J_C$  was normalized to the maximum value.

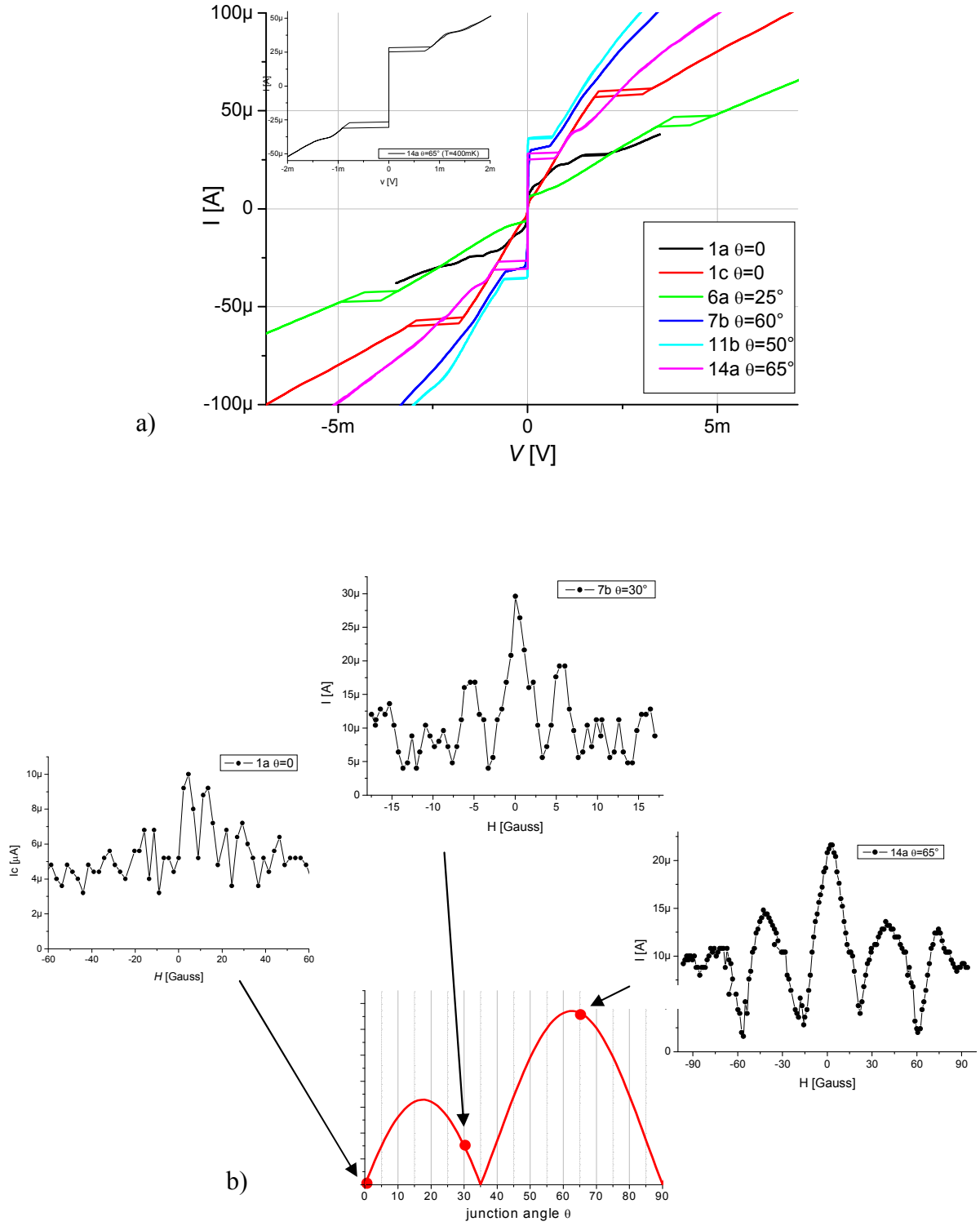


Figure 6.2 Transport properties of LAO based sample #160505:  $I$ - $V$  characteristics of some representative junctions at  $T=0.3K$ , “a” and “c” junctions are  $2.5\mu m$  wide, “b” and “d” are  $5\mu m$  wide (a), magnetic patterns for three different misorientation angles (b).

Sample #140503 a,c=2.5µm		YBCO/CeO <sub>2</sub> /LAO b,d=5.5 µm		YBCO thickness: 180nm		
junction	angle	I <sub>C</sub> (A)	J <sub>C</sub> (A/cm <sup>2</sup> )	R <sub>N</sub> (Ω)	I <sub>C</sub> R <sub>N</sub> (V)	R <sub>N</sub> A (Ωcm <sup>2</sup> )
4d	15°	3.2E-05	3.9E+03	2115	6.7E-02	1.7E-05
5a	20°	7.0E-07	1.9E+02	538	3.7E-04	2.0E-06
6b	25°	3.4E-05	4.1E+03	30	1.0E-03	2.5E-07
8b	35°	3.0E-06	3.6E+02	125	3.7E-04	1.0E-06
10b	45°	1.7E-05	2.1E+03	61	1.0E-03	5.1E-07
11a	50°	1.0E-07	2.7E+01	6540	6.5E-04	2.5E-05
11c	50°	1.4E-05	3.7E+03	65	9.2E-04	2.5E-07
12c	55°	2.0E-06	5.3E+02	24	4.8E-05	9.1E-08
17b	80°	6.0E-06	7.3E+02	6238	3.7E-02	5.1E-05
average				1700	1.2E-02	1.0E-05

Table 6-1 Transport parameters of several junctions from sample #140503. The junctions labelled “a” and “c” are 2.5µm wide, the junctions “b” and “d” 5.5 µm wide

Sample #160505 a,c=2.5µm		YBCO/CeO <sub>2</sub> /LAO b,d=5.5 µm		YBCO thickness: 180nm		
junction	angle	I <sub>C</sub> (A)	J <sub>C</sub> (A/cm <sup>2</sup> )	R <sub>N</sub> (Ω)	I <sub>C</sub> R <sub>N</sub> (V)	R <sub>N</sub> A (Ωcm <sup>2</sup> )
1a	0°	4.0E-06	1.0E+03	118	4.7E-04	4.4E-07
1c	0°	2.0E-06	5.3E+02	197	3.9E-04	7.4E-07
1d	0°	3.4E-05	4.1E+03	143	4.8E-03	1.2E-06
6a	25°	6.5E-06	1.7E+03	124	8.0E-04	4.7E-07
7b	30°	3.0E-05	3.7E+03	119	3.6E-03	9.9E-07
11a	50°	4.5E-06	1.2E+03	104	4.6E-04	3.9E-07
11b	50°	3.6E-05	4.3E+03	50	1.8E-03	4.1E-07
14a	65°	2.8E-05	7.4E+03	55	1.5E-03	2.1E-07
19d	90°	1.0E-05	1.2E+03	23	2.3E-04	1.9E-07
average				88	1.9E-03	5.5E-07

Table 6-2 Transport parameters of several junctions from sample #160505. The junctions labelled “a” and “c” are 2.5µm wide, the junctions “b” and “d” 5.5 µm wide



Although these recent advances in the study of HTS GB junctions opens the way to possible applications to quantum electronics, many issues related to the GB physics remain still obscure and their low reproducibility is still a major obstacle to effective application. During this work, we focused basically on two aspects of STO based biepitaxial junctions: a technological one, the improvement of the fabrication procedure, and a more fundamental one, a better understanding of the transport mechanisms in GBs.

### **6.2.1. Improvements of junctions quality and stability**

The aims of the improvements to the fabrication procedure of the biepitaxial junctions described in detail in the previous chapters were to increase the reproducibility of the junctions and the stability of the GB interface and of the thin film with time. In Figure 6.3 the obtained results are shown.

In the upper panel, the  $J_C(\theta)$  of three STO based samples is shown. The theoretical prediction derived from the Sigrist-Rice formula (see section 2.3.1) is well followed. The fact that so many junctions taken from three different samples realized in different moments all follow this prediction testify the reliability of the fabrication procedure and, most important, the predictability of the junctions' properties.

As regards the stability of the junctions' properties, the same junction with  $\theta=55^\circ$  and nominal width  $w=2.5\mu\text{m}$  from sample #2205, was repeatedly measured to check the degradation due to time and thermal cycling. Some of the  $I$ - $V$ 's are shown in Figure 6.3b. After many months and cool downs, the normal state resistance increased from about  $300\Omega$  to  $500\Omega$ , whereas for the critical current the reduction is negligible ( $\sim 5\%$ ). The degradation of HTS junctions' properties with time is due to the migration of oxygen atoms, which occurs mainly in the GB area, where defects and disorder are present. This issue has also been study with the help of electron beam irradiation shined on the GB, a procedure that enhances the creation of oxygen defects [91]. It was observed that the changes in  $I_C$  and  $R_N$  induced by irradiation are different, suggesting that Cooper pairs and quasiparticle conduction process are governed by different effective barriers. It was also shown that the oxygen exchange induced by irradiation would modify the barrier structure, affecting its dielectric constant and transparency and the superconducting regions close to the interface. Consequently, both  $I_C$  and  $R_N$  would be linked to the dielectric constant. Our results are in good agreement with the observation of a different rate of degradation of the critical current and normal resistance.

Eventually, it is possible to conclude that, after all this time, the junction keeps its main properties and still works remarkably well.

### **6.2.2. GB transport mechanisms**

The difficulties in studying the physics of grain boundaries rise mainly from the interference of the microstructure over the intrinsic transport mechanisms. In section 2.3.3 the interplay between the  $d$ -wave symmetry of the order parameter and the GB microstructure was analysed with particular attention to its effects on the magnetic junctions' behaviour.

The magnetic patterns can indeed be seen as fingerprints of the junctions. A regular, Fraunhofer like, pattern indicates an uniform junction; whereas asymmetric, irregular patterns are generated from the interplay between the  $d$ -wave symmetry and faceting in the GB. Also, the GB can be divided in several superconducting channels if insulating or normal conducting impurities are present; the interference among these channels will cause additional anomalies in the magnetic pattern. Therefore, when regular, Fraunhofer like patterns were measured for some STO based biepitaxial junctions, we realized that the structure of these junctions was particularly uniform and suitable for the study of transport mechanisms in GBs .

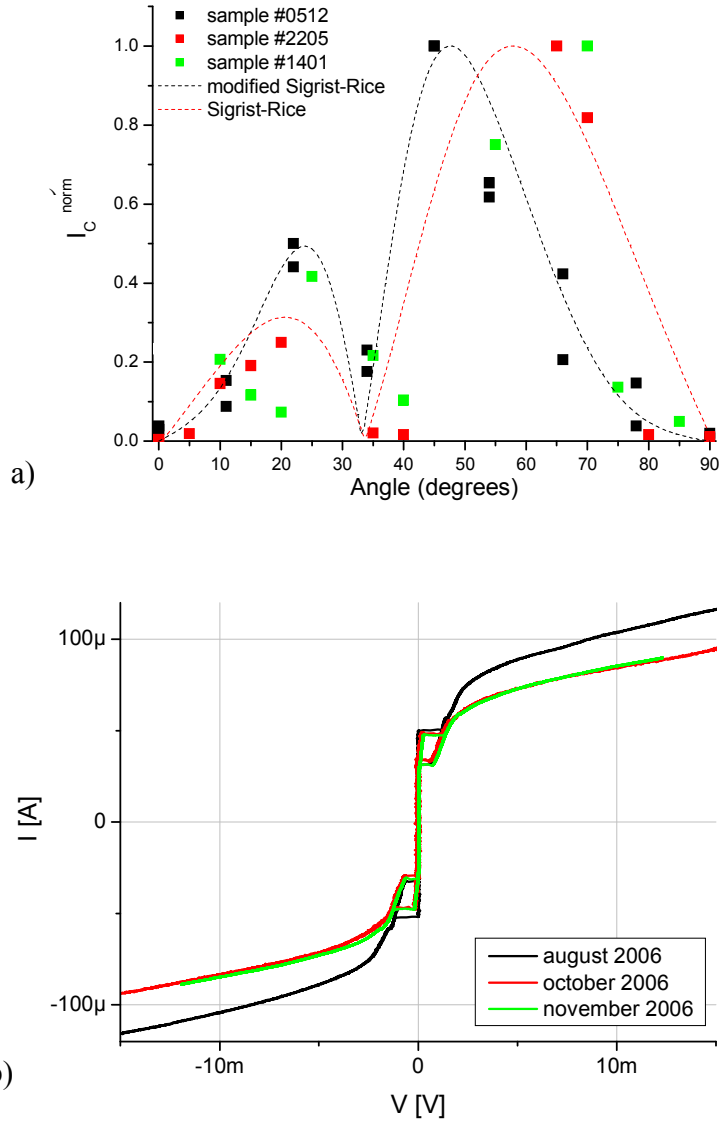


Figure 6.3 Transport properties of STO based biepitaxial junctions. Modulation of the normalized critical current with the junction's angle for three samples (a) and  $I$ - $V$  characteristics of a  $\theta=55^\circ$  junction measured over several months ( $T=0.3\text{K}$ ).

### **GB uniformity**

In a Fraunhofer-like pattern the periodicity, in terms of magnetic field, can give information about the junction's width [15]:

$$\Delta H = \frac{\Phi_0}{L(\lambda_{L1} + \lambda_{L2} + t)} \quad (6.2)$$

where  $\lambda_{L1}$  and  $\lambda_{L2}$  are the London penetration depths of the two YBCO electrodes,  $t$  the film thickness and  $L$  the active junction width. Assuming for YBCO an in-plane London penetration depth of 200nm (since we have to take into account the larger penetration depth of the (103) electrode [30]), the active width of the junction of Figure 6.4a is calculated in the order of 100nm. On the other hand, the nominal (geometrical) width of that junction is 2.5 $\mu\text{m}$ .

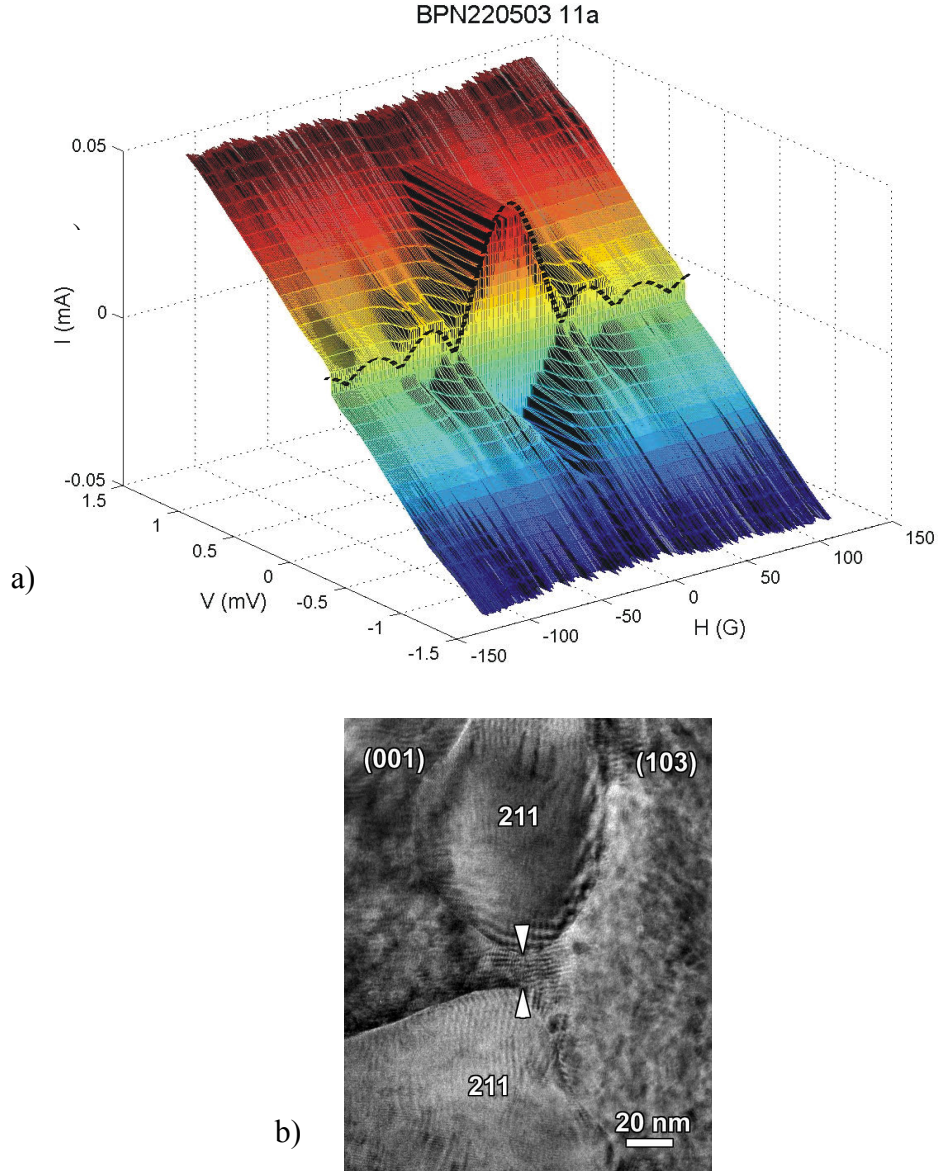


Figure 6.4 (a) Fraunhofer-like  $I_c(H)$  dependence of a STO based biepitaxial junction ( $T=0.3K$ ). The field periodicity point to a single,  $\sim 100nm$  wide channel. Channels of these dimensions are often found in biepitaxial GBs, as showed by planar view transmission electron microscopy (b).

We can suppose that insulating impurities, like the ones showed in the TEM image of Figure 6.4b, obstruct partially the GB channel of this junction, reducing its active width. This assumption is confirmed by the fact channels showed in Figure 6.4b have been often found in biepitaxial junctions, and their width is compatible with the one estimated by the pattern periodicity. The perfect Fraunhofer shape suggests that only one of these channels is active, thus making this junction an almost ideal one and perfect tool to study the transport in ideal GBs.

In order to study the transport in a channel with dimensions of few nanometers, a mesoscopic approach is needed. A complete review of mesoscopic phenomena and of the complex formalism used to describe them goes beyond the scope of this work. In the next section, therefore, only a brief introduction to the mesoscopic phenomenology will be given with the aim to understand better some aspects of the observed phenomena.

## Hints of mesoscopic physics

The ohmic approach to the transport in a conductor connected to two reservoirs is strictly valid when the conductor's dimensions are larger than each of the following lengths:

- the de Broglie wavelength, which is related to the kinetic energy of electrons;
- the electron mean free path, which is the distance that the electron travels before its initial momentum is destroyed;
- the phase-relation length, which is the distance that electron travels before its initial phase is destroyed

In these conditions the common formula for the conductance is valid:  $G = \sigma W / L$  where  $\sigma$  is the material's conductivity,  $W$  and  $L$  the conductors dimensions. When the dimensions of the system are reduced to the nanometer range, the concept of conductance loses its meaning and the decrease in the number of electrons involved in the transport makes it possible to resort directly to the electronic scattering formalism. The mesoscopic regime lies in between the macroscopic and the quantum regime.

In a disordered system the motion of electrons is diffusive, their mean free path  $l_e$  is much smaller than the sample length  $L$ . The electrons move through the sample as nearly plane waves with an amplitude and a phase, covering a random walk colliding with the impurities which sit at random places in the lattice [92]. The collisions can be elastic or inelastic. The inelastic mechanisms, such as thermal fluctuations and phonon collisions, alter the quantum state of the electrons so that they lose their phase memory. As the temperature approaches zero, these processes decrease and inelastic scattering becomes rare [93]. On the contrary, elastic collisions do not destroy the phase information contained in electrons wave function; all the electrons incident in the same state acquire the same phase shift, and the process is reversible (a time-reversed collision would restore the original phase of the wave function). At low temperatures, the time over which conductance electrons maintain their phase coherence  $\tau_\phi$  can exceed the elastic scattering time  $\tau_c$  by several orders of magnitude [94]. In other words, if  $L_\phi$  is the average distance a conduction electron travels during its phase coherent time, then at low enough temperatures, the condition

$$l_e \ll L < L_\phi \quad (6.3)$$

can be verified and the transport in the conductor is diffusive **and** phase coherent. This regime is called mesoscopic regime.

The conductivity is usually defined as an average over travel distances that considerably exceed  $L_\phi$ . In the mesoscopic regime this concept of conductivity loses its meaning since the sample dimensions are smaller than  $L_\phi$ . On the other hand, the number of particles involved in the transport is still too large for the problem to be treated with the electron scattering formalism. Therefore, statistical tools have to be used. A physical property  $X$  of a mesoscopic system is treated as a random variable characterized by its ensemble-averaged value<sup>2</sup>  $\langle X \rangle$  and by its variance  $\langle (\delta X)^2 \rangle$  (where  $\delta X = X - \langle X \rangle$ ).

It is worth remembering that the mesoscopic length scale depends on many parameters, among them the temperature and the purity of a sample, influencing the quantity  $L_\phi$ . Changing the temperature, for example, can move the system inside or outside the mesoscopic regime.

Mesoscopic systems exhibit a peculiar behaviour for some properties which change in an aperiodic fashion and specifically from sample to sample. Among such properties there is the conductance. In a mesoscopic system, the conductance is not a function of the sample

---

<sup>2</sup> The ensemble average is obtained by averaging the value of a particular property, function of the micro-state of a system, over an ensemble of representations.

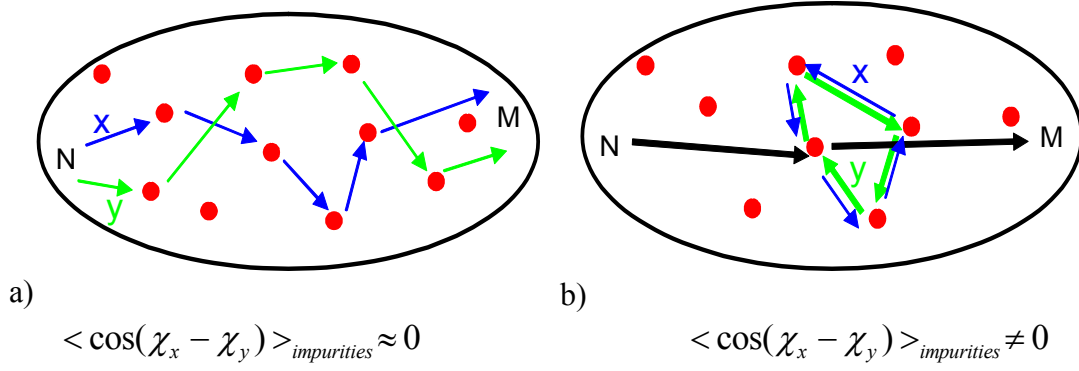


Figure 6.5 propagation of an electron scattered by impurities (red dots). Different trajectories are sketched, “open” trajectories (a) and “closed” trajectories (b).

geometry alone but depends sensitively on the position of each single impurity, thus fluctuates considerably with the impurity configuration. It turns out that the rms amplitude  $\delta G = \sqrt{\langle (G - \langle G \rangle)^2 \rangle}$  of the conductance fluctuations (CF) have a universal value of the order of  $e^2/h$ . It is not hard to understand the origin of the conductance fluctuations. A conduction electron originally located at a given position within the sample spreads out during a time  $t$  over a spherical volume of diameter  $\sqrt{Dt}$  (where  $D$  is the diffusion constant). It can reach every point within this distance covering several random walks set by the scattering centres. In Figure 6.5,  $x$  and  $y$  are two possible electron trajectories between the points  $N$  and  $M$ . The total probability to go from  $N$  to  $M$  is:

$$W = \left| \sum_i A_i \right|^2$$

where  $i$  labels the trajectory and  $A_i$  is the probability amplitude for each trajectory. If, for simplicity, we consider only the two trajectories  $x$  and  $y$ , the total probability will be:

$$|A_x + A_y|^2 = |A_x|^2 + |A_y|^2 + 2|A_x||A_y|\cos(\chi_x - \chi_y) \quad (6.4)$$

where  $\chi_x$  ( $\chi_y$ ) is the phase the electron acquires during the  $x$  ( $y$ ) trajectory. The conductance is calculated by the ensemble average of the contribution from all the trajectories. It is possible to divide the trajectories in two groups: “open” trajectories, as the ones sketched in Figure 6.5a, and “closed” trajectories, sketched in Figure 6.5b. When calculating the ensemble average for the first type of trajectories, the term  $\cos(\chi_x - \chi_y)$  in equation (6.4) vanishes. For the “closed” trajectories, instead, one has  $\langle \cos(\chi_x - \chi_y) \rangle \neq 0$ . The presence of a cosine term leads to the presence of fluctuations in the conductance.

The fluctuations depend on the phase of the trajectories, hence on the particular distribution of the impurities in the sample. Therefore, they are a fingerprint of a specific sample. As regards their amplitude, it has been calculated that, for any size and shape of a metallic sample, the variance of the conductance is in the order of  $e^2/h$  [95, 96], from here the name of *universal* conductance fluctuations.

The involved energy scale  $\varepsilon_c$  is given by the Thouless energy [97]:

$$\varepsilon_c = \frac{\hbar}{\tau_c} = \frac{\hbar D}{L^2}$$

where  $D$  is the diffusion constant of the material,  $L$  the geometrical dimension of the sample,  $\tau_c$  is the diffusion time  $L^2/D$ . The Thouless energy represents the energy interval the electrons have to belong to in order to produce interference.

### ***Universal conductance fluctuations in biepitaxial junctions***

Mesoscopic phenomena have been widely investigated in metallic wires and in tunnel [98] and low temperature Josephson junctions [99]. The use of junctions for this type of experiments makes it possible to systematically examine the conductance fluctuations as a function of electron energy. The bias voltage over the conductors drops almost completely inside the barrier, because the resistance of the junction is much larger than the resistance of the superconducting banks. The junction serves then as an injector of electrons in a specific energy range which can be tuned by the bias voltage.

In the previous section we remarked that the conductance fluctuations depend on the impurities distributions that change from sample to sample. Instead of studying a large number of sample, in the case of Josephson junctions one can study the same sample changing the external conditions, in this case the magnetic field (ergodic hypothesis).

Before the experiments that will be described in this section [100], there was no evidence in the literature of mesoscopic effects, that is of diffusive and coherent transport of the quasi particles, in HTS junctions. The reason should be found in the difficulty in realizing grain boundaries composed of a single channel with sub micrometric dimensions. In the junction whose pattern is showed in Figure 6.4a, instead, a “self protected” (in the sense that no patterning method was used to obtain it), nanometric channel was formed, possibly allowing the approach of the mesoscopic regime.

A preliminary evaluation of length scales tells that, for our channel of  $\sim 100\text{nm}$  width, mesoscopic effects can be observed. These effects arise when the inequality (6.3) holds. The right hand part of the inequality ( $L < L_\phi$ ) is satisfied at low temperatures, the validity of the second part ( $l_e \ll L$ ) is assured by the dimensions of the channel.

We measured  $I$ - $V$  characteristics down to 0.3K and in magnetic field. In these  $I$ - $V$ 's fluctuations of the normal state resistance  $R_N$  field could be distinguished. An example is showed in Figure 6.6a. The fluctuations are one order of magnitude larger than the noise (Figure 6.6b) and, for temperatures lower than 0.9K, their amplitude increases with decreasing the temperature (Figure 6.6c).

In low temperature Josephson junctions,  $R_N$  represents the resistance at a voltage a few times larger than the gap value. This matter is more delicate when dealing with HTS junctions, because of the deviations from the ideal RSJ behaviour. In our case a linear branch typical of the RSJ behaviour starts at  $V=5$  mV (the  $I$ - $V$ 's of this junctions can be seen in Figure 6.3b). In order to investigate these fluctuations, we focused on the voltage range  $V \in [10\text{mV}, 15\text{mV}]$  in which the  $I$ - $V$ 's characteristics were linear and the resistance could reasonably be considered as normal state resistance. Insights on the fluctuations can be gained calculating the ensemble average of the autocorrelation of the conductance fluctuations  $\delta G \equiv G - \bar{G}_N$  (with  $G_N = 1/R_N$ ) over the magnetic field  $H$ :

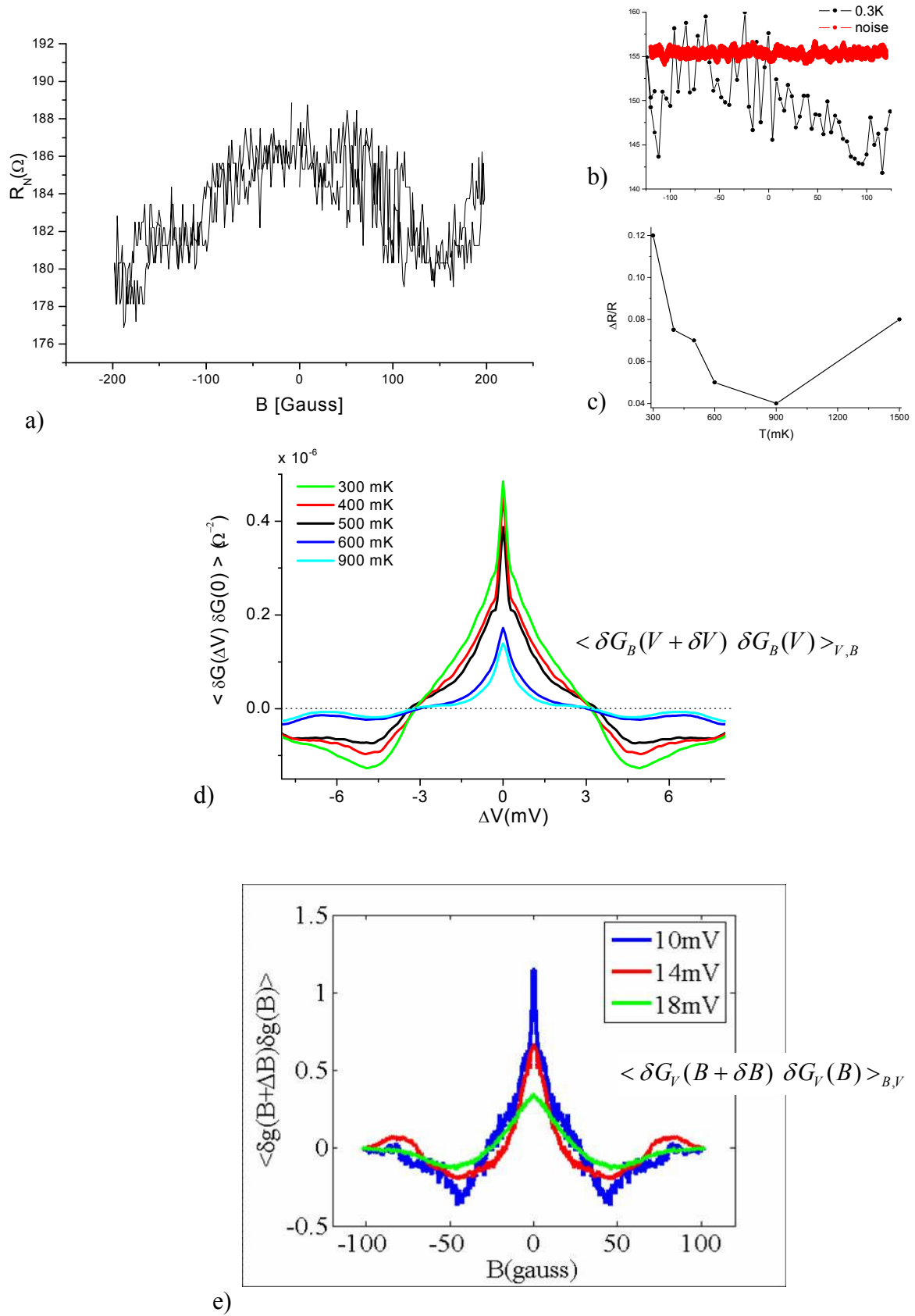


Figure 6.6 In a mesoscopic biepitaxial channel, magnetoconductance fluctuations were measured (a). Their amplitude is one order of magnitude larger than the noise's one (b) and, for temperatures lower than 0.9K, increase with decreasing temperature (c). Correlation functions were measured with respect to the voltage (d) and the magnetic field (e). In the latter case the conductance has been normalized to the quantum conductance.

$$\langle [G(\Delta V) - \overline{G_N}] [G(0) - \overline{G_N}] \rangle = \frac{1}{N_V} \sum_V \left\langle [G(V + \Delta V, H) - \overline{G_N}] [G(V, H) - \overline{G_N}] \right\rangle_H \quad (6.5)$$

where  $N_V$  is the number of small intervals in which the voltage range [10mV, 15mV] is divided. The autocorrelation of equation (6.5) is reported as a function of  $\Delta V$  in Figure 6.6d at different temperatures. In mesoscopic physics, the half width at half maximum of the autocorrelation function versus  $V$  gives important information on the energy scales (Thouless energy) involved in the transport. From Figure 6.6d it can be seen that in this experiment  $\varepsilon_c$  is in the order of 1.5meV. This value is consistent with the value of the Thouless energy  $\varepsilon_c = \hbar / \tau_c = \hbar D / L^2$  resulting from the estimations of  $L$  from the magnetic pattern and structural investigations. Since the inequality  $\tau_\phi > \tau_c$  has to be followed, because of coherent transport, from the value of  $\varepsilon_c$  we can derive a lower bound for the quasiparticles dephasing time:  $\tau_\phi > 1\text{ps}$ .

The autocorrelation function can also be averaged over the voltage and plotted as a function of the magnetic field (Figure 6.6e). In this case, the width at half maximum will give a critical field  $B_c$  that is proportional to  $\Phi_0 / L_\phi^2$ . From the data showed, it is possible to calculate  $L_\phi \approx 1\mu\text{m}$ , thus confirming the applicability of the mesoscopic approach, given  $L = 100\text{nm} \ll L_\phi = 1\mu\text{m}$ .

When compared with results on more traditional systems (see for example Ref. [98]), fluctuations in our sample appear at relatively higher voltages  $k_B T \ll \varepsilon_c < eV < \Delta$ , and this seems to be peculiar of the grain boundary system. This means that the effect is robust with respect to energy broadening due to temperature (it persists up to 1K) but also with respect to the energy relaxation processes induced by the applied voltage. Another interesting feature is the fact that the Thouless energy, the ruling energy scale in mesoscopic transport, is found to be of the same order of magnitude of the product  $I_C R_N$ , connecting the critical current to the transport properties at high voltages, and giving additional consistency to the whole picture.

These results highlight for the first time the wave-like nature of the quasiparticles in an HTS channel. The key to observe such behaviour has been the dimension of the sample. A junction's width in the sub-micron range gives the possibility to enter the mesoscopic regime, where the quasiparticles are coherent over a length  $L_\phi$  and for a time  $\tau_\phi$ . These findings can be of great importance in HTS electronics, since they give an indication on how to decrease the decoherence due to the quasiparticles by decreasing the dimensions of the junctions. Moreover, this is probably just one of the phenomena that may arise or surface when the dimensions of the junctions are reduced.

The experiment just described was carried out with an "accidental" sub-micrometer junction, a junction whose dimensions were determined by insulating impurities. If on one hand the self-protected nature of the channel makes it an ideal structure, on the other makes its realization completely outside our control. The subsequent step, therefore, was to use e-beam lithography to try to fabricate sub-micrometric junctions in a reproducible and controlled way.

### 6.3. STO based sub-micrometric junctions

Junctions with various width and YBCO film thickness were fabricated using electron beam lithography and the carbon mask technique described in chapter 4. The characteristics of the samples are listed in the following table:



<u>Sample#070313A</u>	YBCO thickness: 120nm
junctions width:	0.6 $\mu$ m 1.3 $\mu$ m
<u>Sample#070402</u>	YBCO thickness: 170nm
junctions width:	0.8 $\mu$ m 1.5 $\mu$ m
<u>Sample#070605B</u>	YBCO thickness: 200nm
junctions width:	0.8 $\mu$ m 1.5 $\mu$ m

Different widths and YBCO thicknesses were used in order to have the possibility to investigate different transport regimes. In the extreme case, width 0.6 $\mu$ m and YBCO film thickness 120nm, the junctions do not show Josephson behaviour but rather a tunnel-like one. These junctions gave remarkable results when the conductance curves were analyzed as a function of the misorientation angle, as will be showed in the next paragraph. Here, we will focus on sub-micrometric junctions with Josephson behaviour. The data collected until now serve as a preliminary investigation of the junctions' quality and, eventually, as a guide for a further improvement of the fabrication process. More detailed investigations will be carried out in the next future.

A collection of transport results is showed in Figure 6.7. For clarity, only few  $I$ - $V$ s for each sample are showed. The characteristic of the samples and the main properties values are listed in tables 1-3, 1-4 and 1-5.

From the observation of the plots in Figure 6.7 it is immediate to see that the YBCO film thickness has a great importance on the quality of the junctions and on the transport properties. In the first two samples with thinner films, indeed, we found that only the larger junctions (1.3 and 1.5 $\mu$ m) showed Josephson behaviour and an appreciable Josephson current. The first sample even showed tunnel-like junctions, as we mentioned. In the third sample, fabricated with a thicker YBCO film, also the narrower junctions (0.8 $\mu$ m) showed a very good  $I$ - $V$  curve, clear Josephson behaviour and also remarkable hysteresis. The reason for this behaviour is probably to be found in the capacity of thicker films to "self heal" the loss of oxygen at the GB occurring during the junctions fabrication. A confirmation of this assumption can be found in Ref. [101] where transport properties of bicrystal junctions down to 200nm in width with very thin YBCO films (20-30nm) are shown. The authors show that the as-patterned junctions had poor Josephson properties and in some cases didn't show superconductivity at all. The properties were significantly improved after an ultraviolet light assisted oxygenation process, thus confirming the role of oxygen loss in transport properties of narrow HTS constrictions. In our work, the loss of oxygen was probably compensated for YBCO film thickness greater than 170nm.

The junctions' parameters listed in tables 1-3, 1-4 and 1-5 have been compared in Figure 6.8 with several data available in the literature concerning other types of HTS junctions and micrometric biepitaxial junctions. Also some data from sub-micrometric bicrystal [102] and ramp junctions [103] are included. Despite their reduced size, that makes them more sensitive to process induced damage, the biepitaxial sub-micrometric junctions realized during this work have properties comparable with the other structures, also sub-micrometric, thus confirming the accuracy of the patterning procedure. The difference in the three biepitaxial sub-micrometric samples properties is reflected also in this plot. The data from samples #070313A and #070402 (the ones with thinner YBCO film) have, indeed, higher values of the  $R_N A$  product, thus confirming that their behaviour is shifted towards a tunnel-like one. The

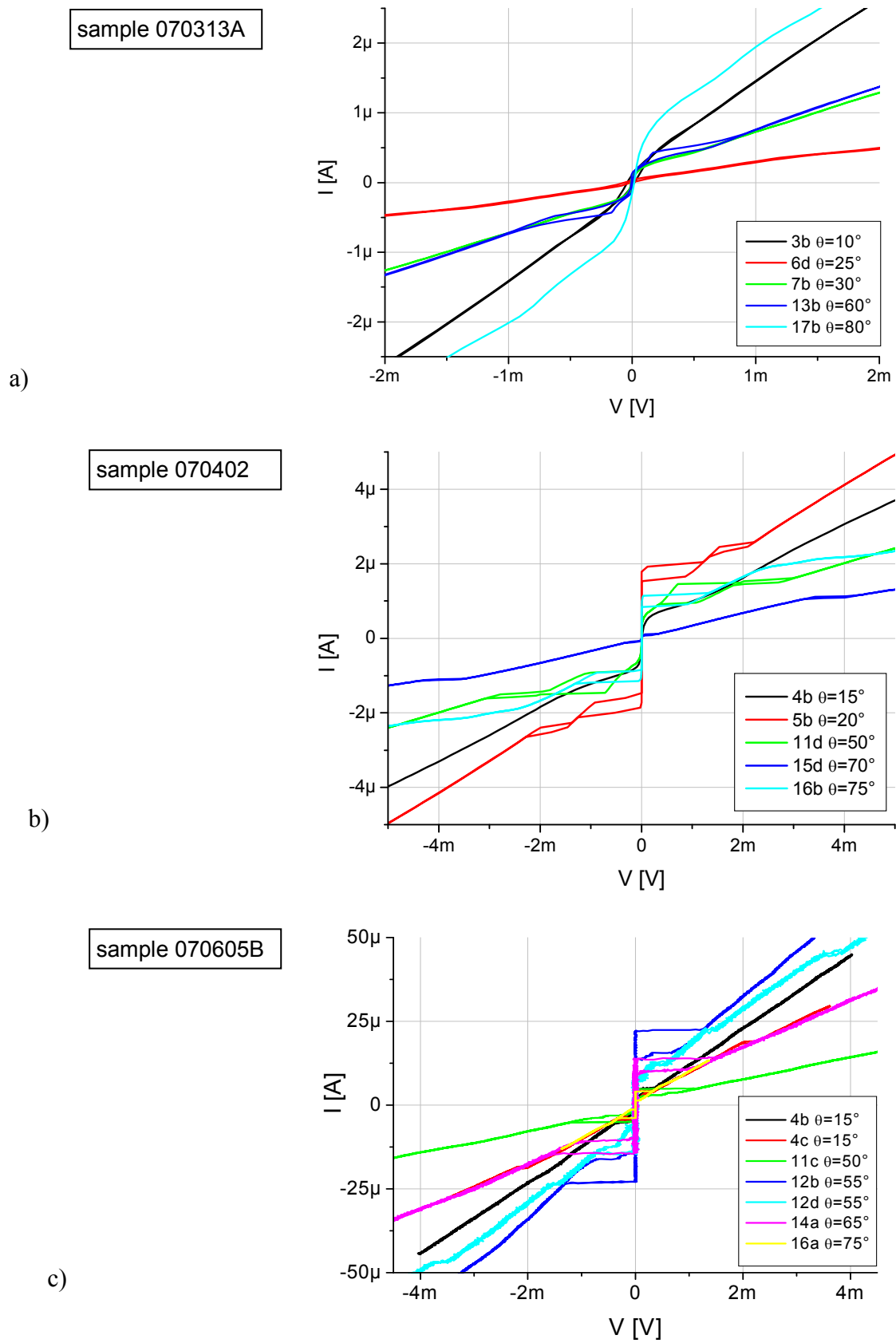


Figure 6.7 I-V characteristics of micrometric and sub-micrometric junctions from three different samples with different YBCO films thickness. All the measurements were taken at 0.3K. The samples and junctions' properties are listed in the following Tables.

Sample #070313A YBCO/CeO <sub>2</sub> /STO b,d=1.3 $\mu$ m YBCO thickness: 120nm						
junction	angle	I <sub>C</sub> (A)	J <sub>C</sub> (A/cm <sup>2</sup> )	R <sub>N</sub> ( $\Omega$ )	I <sub>C</sub> R <sub>N</sub> (V)	R <sub>N</sub> A ( $\Omega$ cm <sup>2</sup> )
3b	10°	1.0E-07	6.4E+01	1390	1.4E-04	2.1E-06
3d	10°	1.1E-07	7.1E+01	7576	8.3E-04	1.1E-05
5b	20°	9.0E-07	5.8E+02	862	7.7E-04	1.3E-06
6d	25°	1.3E-08	8.3E+00	4545	5.9E-05	7.1E-06
7b	30°	2.0E-07	1.3E+02	1961	3.9E-04	3.0E-06
13b	60°	1.8E-07	1.2E+02	1990	3.6E-04	3.1E-06
14b	65°	3.0E-08	1.9E+01	4464	1.3E-04	6.9E-06
17b	80°	8.0E-07	5.1E+02	709	5.6E-04	1.1E-06
19d	90°	7.0E-07	4.5E+02	909	6.3E-04	1.4E-06
average				2660	3.9E-04	4.1E-06

Table 6-3

Sample #070402 YBCO/CeO <sub>2</sub> /STO b,d=1.5 $\mu$ m YBCO thickness: 170nm						
junction	angle	I <sub>C</sub> (A)	J <sub>C</sub> (A/cm <sup>2</sup> )	R <sub>N</sub> ( $\Omega$ )	I <sub>C</sub> R <sub>N</sub> (V)	R <sub>N</sub> A ( $\Omega$ cm <sup>2</sup> )
4b	15°	1.7E-06	7.5E+02	2011	3.5E-03	4.6E-06
5b	20°	1.8E-06	8.0E+02	1104	2.0E-03	2.5E-06
11d	50°	4.0E-07	1.7E+02	4300	1.7E-03	9.8E-06
15d	70°	5.0E-08	2.2E+01	5630	2.8E-04	1.2E-05
16b	75°	1.1E-06	4.8E+02	3122	3.4E-03	7.0E-06
average				3233	2.1E-03	7.1E-06

Table 6-4

Sample #070605B YBCO/CeO <sub>2</sub> /STO a=0.8 $\mu$ m b,d=1.5 $\mu$ m YBCO thickness: 200nm						
junction	angle	I <sub>C</sub> (A)	J <sub>C</sub> (A/cm <sup>2</sup> )	R <sub>N</sub> ( $\Omega$ )	I <sub>C</sub> R <sub>N</sub> (V)	R <sub>N</sub> A ( $\Omega$ cm <sup>2</sup> )
4b	15°	4.7E-06	1.6E+03	94	4.4E-04	2.8E-07
4c	15	4.5E-06	2.8E+03	128	5.8E-04	2.1E-07
11c	50	4.8E-06	3.0E+03	290	1.4E-03	4.7E-07
12b	55°	2.2E-05	7.3E+03	68	1.5E-03	2.1E-07
12d	55°	1.2E-05	4.0E+03	87	1.0E-03	2.6E-07
14a	65°	1.3E-05	8.1E+03	142	1.8E-03	2.3E-07
16a	75°	4.0E-06	2.5E+03	110	4.4E-04	1.8E-07
average				1.3E+02	1.0E-03	2.6E-07

Table 6-5

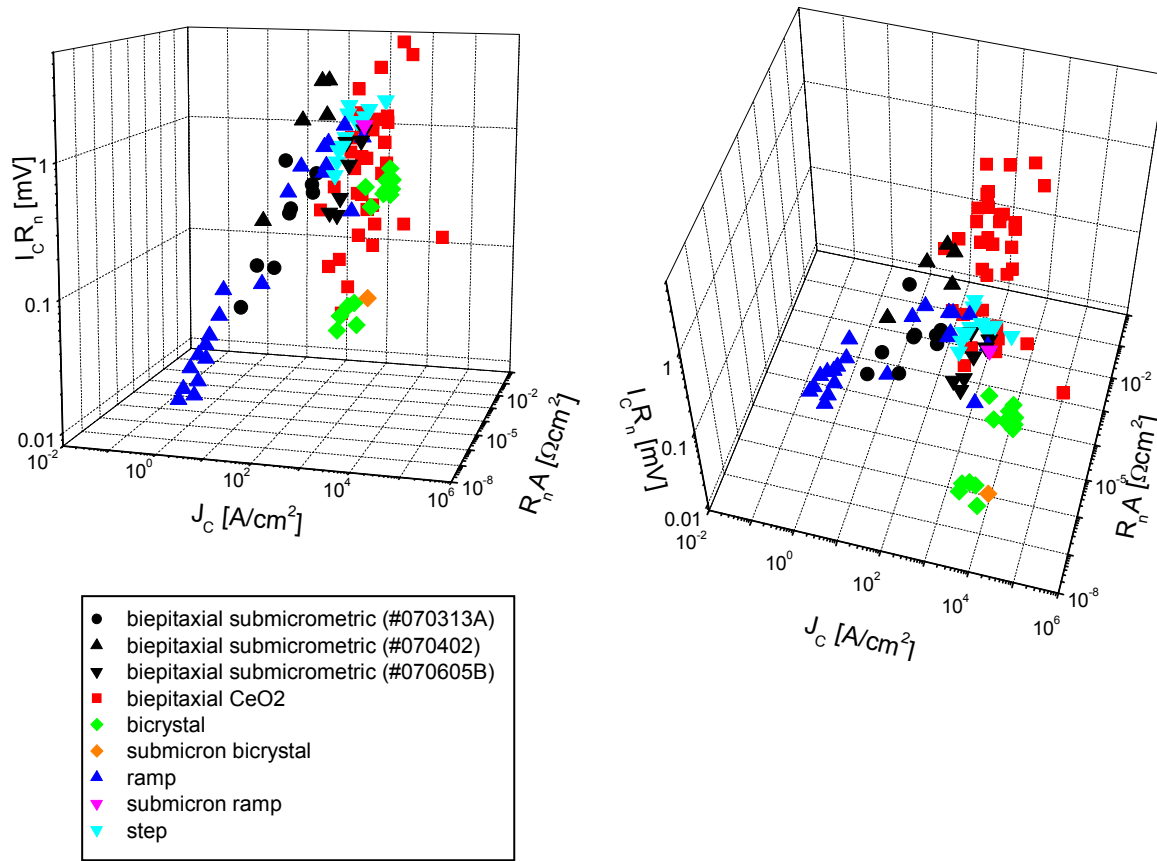


Figure 6.8 Plot of the  $I_C R_N$  versus  $J_C$  and specific resistance  $R_N A$  for different types of junctions. The data are taken from Ref. [19, 24, 30, 90, 102, 103, 40]

third sample #070605B has an higher  $I_C R_N$  product, brought mainly by the higher  $J_C$  values, thus confirming its higher quality.

For these reasons, in the rest of the paragraph we will focus our analysis on the sample with the thickest YBCO film (sample #070506B), as more representative for the transport regime of interest for electronic applications. All the  $I$ - $V$ 's from this sample show a significant hysteresis, calculated as  $(I_c - I_r)/I_c$  (with  $I_r$  the retrapping current). It goes from 22% for junction 17a to 67% for junction 16a, confirming a low transparency barrier and an RCSJ-like behaviour.

As the magnetic characterization of the junctions is concerned, the  $I_C(H)$  plots measured up to now are showed in Figure 6.9. All of them show the maximum of the critical current at zero applied magnetic field and a shape that can be traced back to a Fraunhofer-like pattern.

Unlike large junctions, the deviations from the Fraunhofer behaviour showed in these plots are few and can be easily established:

- In the pattern (b), referring to junction 16a, a double periodicity can be observed. This behaviour is typical of a system composed of two junctions in parallel, the two modulations being originated by the single junctions and the whole loop. Probably, in this junction a microvoid or an impurity nucleated in the middle of the channel, practically dividing it in two parts.
- The pattern in panel (c) shows some features that could be related to the presence of a 2<sup>nd</sup> harmonic component in the current-phase relation (see section 2.3.4). Features similar to the ones highlighted with a circle are, indeed, found also in the theoretical pattern shown

in the panel (d), calculated for a ratio  $\alpha = I_2 / I_1$  of about 1.5. As described in section 2.3.4, the presence of a second harmonic component should be favoured by a lobe versus node configuration of the order parameters of the electrodes. The misalignment angle of the showed junction is  $80^\circ$ , thus very close to this condition.

- The asymmetry and the dip in the main lobe of the junction 14a pattern (Figure 6.9e) can be fit by taking into account the presence of two facets in the GB line. The simulated pattern for a two facets junction is showed in panel (f) [104]; there is a very good qualitative agreement between the two.

From the period of the patterns, it is possible to estimate, using equation (6.2), the width of the junction's active channels. The values calculated are listed in Table 6-6 together with the nominal (geometric) width of the junctions.

junction	panel in Figure 6.9	$\Delta H$	nominal width	active channel width
12b	a	9mT	1.5 $\mu\text{m}$	0.37 $\mu\text{m}$
16a	b	10/30mT	0.8 $\mu\text{m}$	0.3/0.1 $\mu\text{m}$
17a	c	23mT	0.8 $\mu\text{m}$	0.14 $\mu\text{m}$
14a	e	60mT	0.8 $\mu\text{m}$	0.05 $\mu\text{m}$
11c	g	135mT	0.8 $\mu\text{m}$	0.02 $\mu\text{m}$

Table 6-6 active channel width calculated for the patterns showed in Figure 6.9. For junction 16a the double periodicity leads to single junctions 0.1nm wide forming a loop of 0.3nm.

The data available up to now are for sure not enough for a reliable statistic, however it is possible to conclude that the transport in these junctions is likely to take place across one or maximum two channels (as in the case of junction showed in Figure 6.9b). The dimensions of the channels are in the range of a few hundreds of nanometers, making the junctions good candidate for the study of the mesoscopic effects described in the previous paragraph.

It is interesting to note that the dimensions of the nano-channels are always in the same range. This points to a structural reason for their existence. They could be generated, for example, by the fact that the (103) grains have an elongated shape, therefore their dimensions could determine the effective channels width. We plan to confirm this hypothesis studying the magnetic patterns of the junctions with few channels towards the twist and tilt limit, where the coupling between the wide (001) grains and the elongated (103) ones change because of the misalignment angle (see Figure 6.10).

We can conclude that the reduction in the junctions' size makes it easier to identify the effect of the microstructure on the GBs' transport, as the example of Figure 6.9d demonstrates, and eventually of a second harmonic component.

#### 6.4. Spectroscopy of tunnel-like junctions

As it has been introduced in the previous paragraph, the 0.6 $\mu\text{m}$  wide junctions from sample 070313A, realized with a 120nm YBCO film, did not show any Josephson current but a tunnel-like behaviour. Tunnel junctions, in the common *S-I-S* or *S-N-S* configurations, are very useful for fundamental investigations on the physics of superconductors, especially for the study of the superconducting gap and related issues. They are difficult to realize with HTS, given the short coherence length of these materials and the surface disuniformities. Reducing the junction width and the YBCO film thickness, instead, we managed in controllably degrading the biepitaxial GB barrier and reach a tunnel-like behaviour. This result was made possible also by the fact the biepitaxial structure shows, from the start, lower transmissivity if

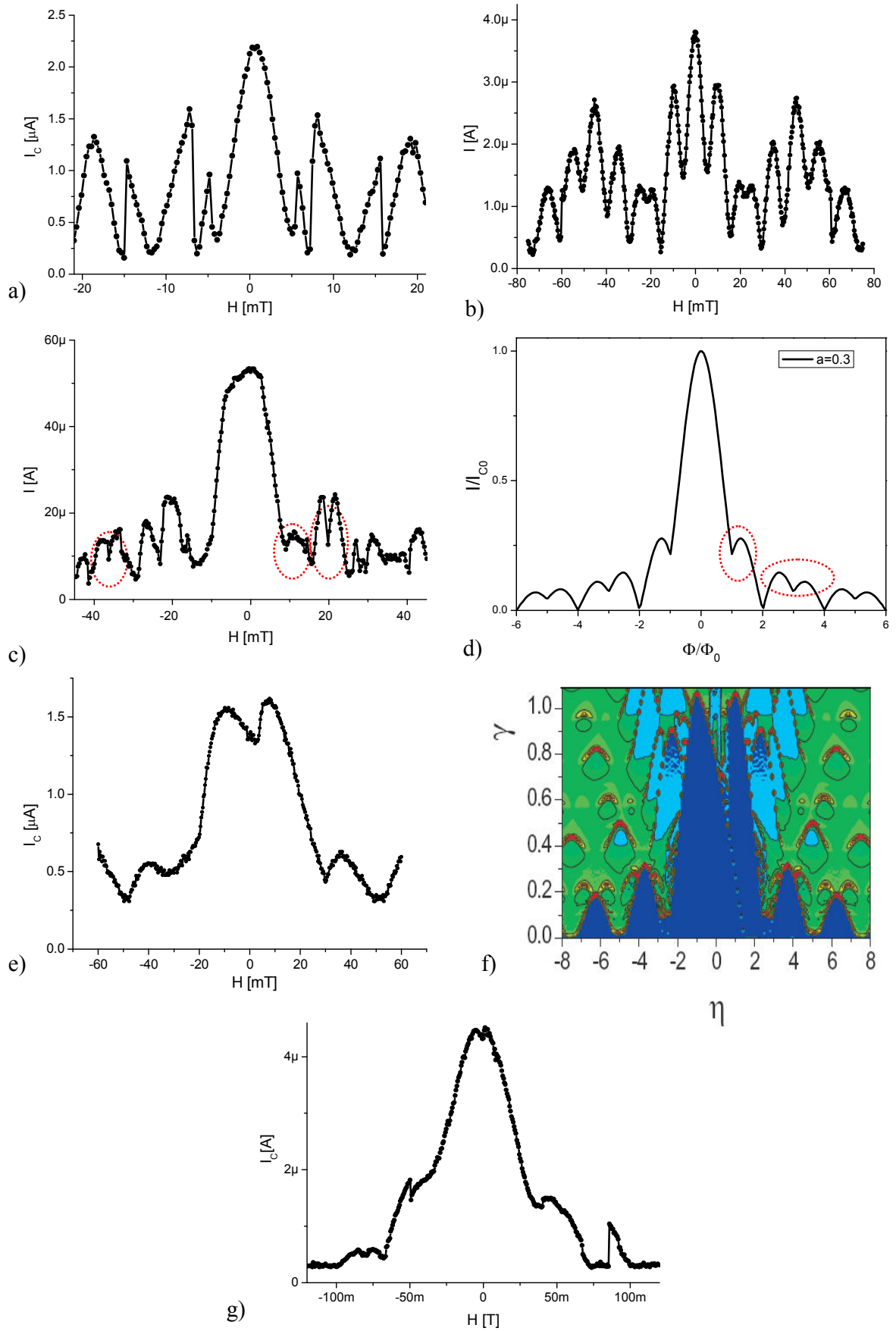


Figure 6.9  $I_C(H)$  patterns of few junctions from sample 070605B: (a)  $\theta=55^\circ$ ; (b)  $\theta=75^\circ$ ; (c)  $\theta=80^\circ$ ; (d) simulated pattern with 2<sup>nd</sup> harmonic component in the CPR ( $a=I_2/I_1=0.3$ ); (e)  $\theta=65^\circ$ ; (f) simulated pattern for a junction with two facets; (g)  $\theta=50^\circ$ . The experimental patterns were measured at  $T=0.3\text{K}$ .

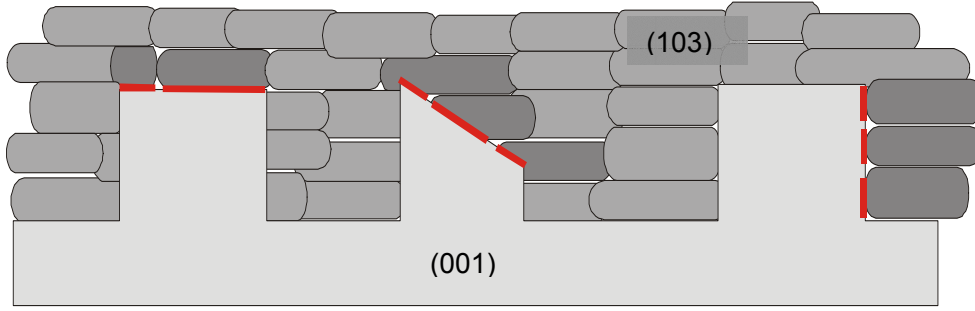


Figure 6.10 Sketch of the possible mechanism influencing the formation of nano-channels in biepitaxial junctions. The channels could be due to the encounter between the (001) large grains and the (103) elongated ones. The contact area between the two grains changes also with the junctions' misalignment angle

compared to other GB structures. Using these tunnel-like junctions, a gap spectroscopy experiment was carried out.

Before describing this experiment, a brief introduction of gap spectroscopy on cuprate superconductors is required.

#### 6.4.1. Overview of gap spectroscopy

Just as for conventional superconductors, it is rare in the high temperature superconductors to have definitive measurements of both the Cooper pair and quasi-particle tunnelling in the same experiment because of their different energy scales. These energy scale differences are even more dramatic for HTS than for conventional superconductors. Therefore, gap experiments are carried out with tunnel junctions.

Tunnelling measurements played an important role in the understanding of conventional superconductors, providing direct evidence for a gap in the density of states of a superconductor, high precision measurements of the size, shape, temperature, and field dependence of this gap and strong evidence for the electron–phonon mechanism. However, tunnelling into the cuprate superconductors is much more complex, and arguably much more interesting, than tunnelling into conventional superconductors [105]. Some of the properties of the cuprate superconductors that make this such a rich topic include unconventional pairing symmetry, pseudogap behaviour, spatial inhomogeneities. Much work has been done to address each of these issues, as described in several reviews written during the years (see for example Ref. [105]).

The connection between the conductance of a tunnel junction and the density of states of the superconducting electrodes was given in section 2.3.2 (equation (2.3)). In terms of tunnelling current, this can be written as [15, 105]:

$$I = \frac{2e}{\hbar} \int [f_1(E) - f_2(E)] \bar{T}(E) dE$$

where  $f_1$  and  $f_2$  are the Fermi functions of the electrodes and  $\bar{T}$  the contacts transparency. It is straightforward to understand from the expression above that in a  $N-I-S$  junction, the tunnel effect allows a direct measurement, through the conductance of the junction, of the density of states in the superconductor, and therefore of the energy gap (Figure 6.11a). The conductance curve  $G(V)$  will reflect also the peculiar properties of the electrodes and the barrier. It is particularly interesting to point out that, in real systems, energy states lower than the gap are

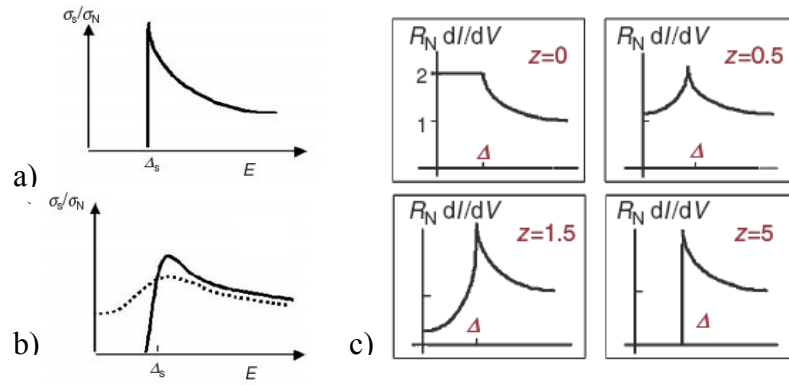


Figure 6.11 Conductance in an ideal N-I-S junction (a) and in the presence of impurities (b). The effect on the conductance curve of the barrier transmissivity (indicated by different value of the parameter  $z$ ) is also shown (c).

made available thanks to the presence of impurities at the barrier and in the  $N$  layer. The result is a smearing of the peak structure corresponding to the gap value  $\Delta/e$ , and a reduction of  $\Delta$ , as indicated schematically in Figure 6.11b. A more detailed description of the barrier effects in gap spectroscopy is due to Blonder, Tinkham, and Klapwijk [106]. They introduced the dimensionless parameter  $z$ , proportional to the potential barrier at the interface, to describe the barrier transparency  $\bar{T} = 1/(1+z^2)$ , allowing a continuous description from a highly transmissive barrier to the tunnel limit. Conductance for a  $S$ - $N$  junction is displayed in Figure 6.11c for different values of the parameter  $z$ . These considerations are especially useful in the case of HTS structures.

One of the few options to realize “pure” tunnel junctions with HTS is represented by scanning tunnelling microscopy (STM), where a tunnel barrier is formed between the superconductor surface and the scanning tip held a few Ångström on top of it. This is a very sensitive and well established technique that can reveal important features of the gap structure. Figure 6.12a and b, for example, show STM tunnelling conductance data into the  $\{110\}$  and  $\{001\}$  faces of an optimally doped YBCO single crystal [107], showing the 2D nature of the gap symmetry. The authors demonstrate that their data could be consistently modelled using a pure  $d_{x^2-y^2}$  pairing symmetry, for tunnelling into various crystalline faces. The maximum gap value in the  $\{001\}$  direction is found to be  $\sim 20$  mV, in agreement with a number of previous studies. On the other hand, STM does not allow for a detailed angular characterization of the gap. This can be achieved only using junctions, as done by Iguchi and co-workers in a series of experiments in which tunnel junctions were realized using the ramp edge technology. An YBCO [108] or LSCO [109] film was deposited on a suitable substrate, covered with an insulating material and patterned to form a ramp. A silver counter-electrode was then deposited and the device was patterned again to define the junctions’ bridges (inset of Figure 6.12c). This technique allows to realize tunnel junctions at any arbitrary angle (inset of Figure 6.12d). Some of the conductance curves measured from these samples are shown in Figure 6.12c and d. For a couple of angles, gap structures are visible in the conductance, as indicated by the arrows. The position of these structures is compatible with  $d$ -wave symmetry of the gap and its maximum value, although also other fine structures are seen. Also, in Figure 6.12d, it is possible to see a peak at the gap voltage for a  $45^\circ$  junction, where the gap should be zero. The reason is that, as often happens in HTS structures, the transport took place through a cone rather than in a single direction.



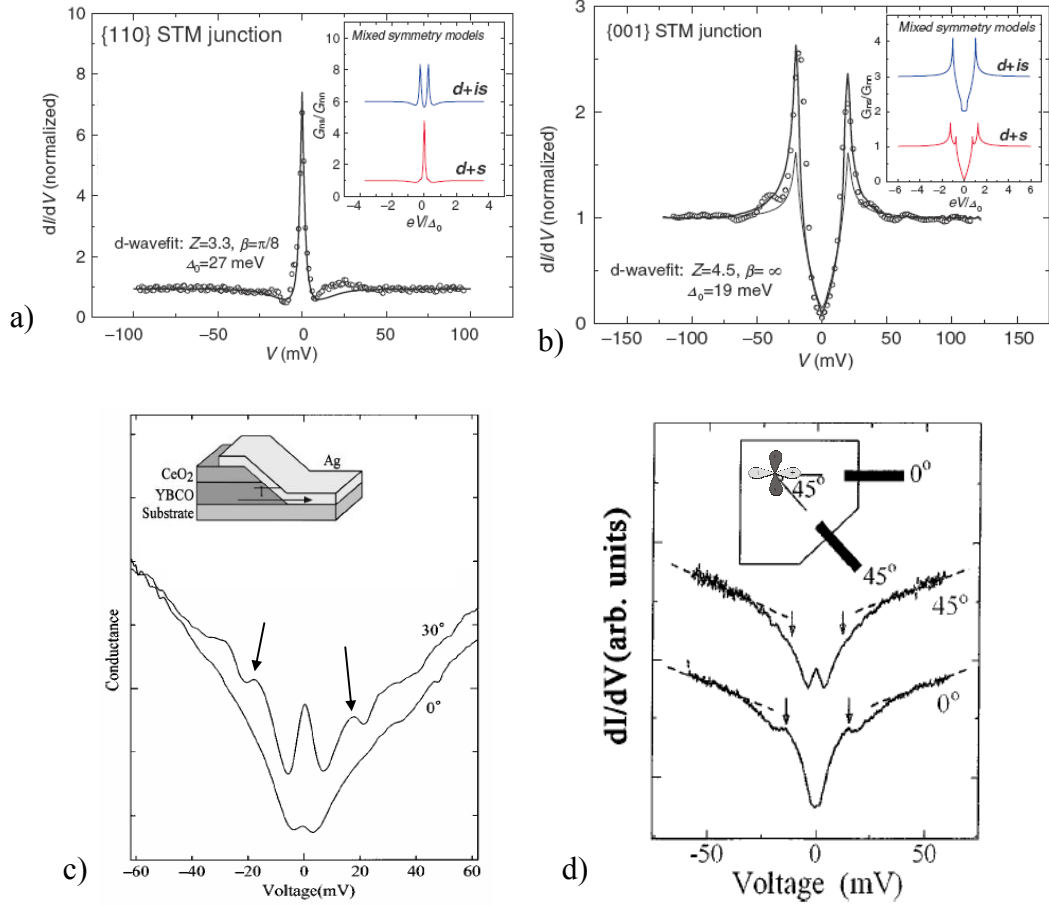


Figure 6.12 Conductance data for: an STM tunnel junction on the {110} (a) and {001} crystal faces (b) of YBCO (the solid lines are fits assuming a  $d_{x^2-y^2}$  pairing symmetry) and for ramp type tunnel junctions realized with YBCO (c) and LSCO (d) (in the insets the structure of the junctions are shown)

#### 6.4.2. Gap spectroscopy using biepitaxial tunnel-like junctions

The results on ramp-type junctions just described are, to our knowledge, the only example present in the literature of gap angular spectroscopy using HTS tunnel junctions. Using tunnel-like biepitaxial junctions, we were able to make tunnelling measurements over a wider range of misorientation angles. Examples of tunnel-like characteristics measured in the biepitaxial sample #070313A are shown in Figure 6.13a and c, next to the conductance curves calculated from them.

A first comment has to be done concerning the marked asymmetry of the curves. This feature is typical of asymmetric barriers (Schottky barrier) [110], where the forward and reverse bias see different potential, as sketched in the inset of Figure 6.13d. The asymmetry, in our case, is given by the presence of an off-axis electrode (the (103) YBCO electrode).

A more interesting feature of the conductance curves is the presence of many peaks and shoulder-like structures. We measured several junctions with different misorientation angles and verified that the position of the peaks changes with the angle. The comparison of the experimental peaks position with what is predicted from the  $d$ -wave symmetry is made complex in this case by the particular biepitaxial structure. It is indeed necessary to calculate which angle the junction's misorientation direction determines for the single electrode's gap, taking into account the (001) orientation plus  $45^\circ$  in plane rotation of one electrode (electrode I) and the (103) orientation of the other (electrode II). Then, gap structures in the conductance curve for a given junction's misorientation angle should be found in correspondence of the sum and of the difference of the gap values of the two electrodes. The light and dark blue

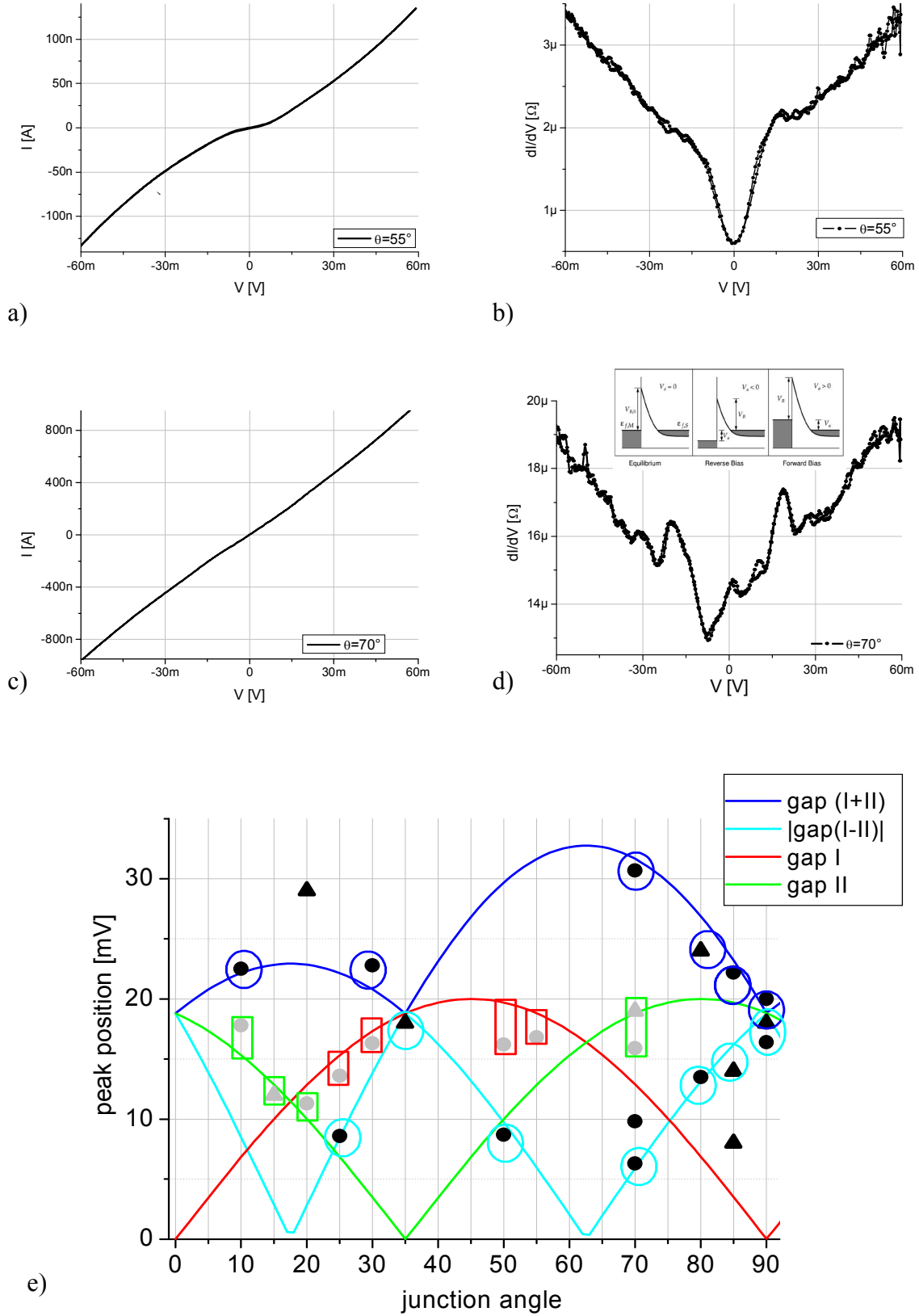


Figure 6.13 Transport measurements on tunnel-like biepitaxial junctions: examples of  $I$ - $V$  curves (a), (c) with respective conductance curves (calculated) (b) and (d). The peaks in the conductance curves change position with the junctions' misorientation angle. These positions are collected in (e) and compared with the gap values calculated for the biepitaxial geometry.

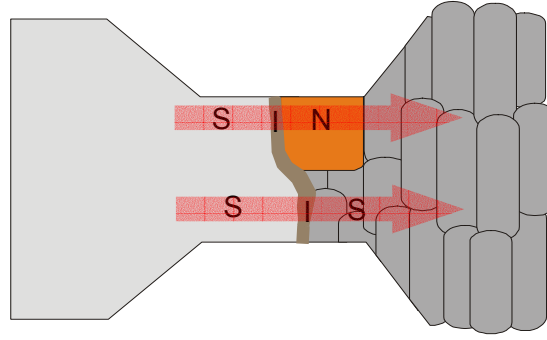


Figure 6.14 Sketch of a tunnel GB channel where a normal conducting impurity determines the presence of both  $S-I-N$  and  $S-I-S$  junctions

solid lines in Figure 6.13e are the result of this calculations. In the same figure, the position of the peaks in the experimental conductance curves are shown in black. Circles have been drawn on the image to facilitate the “assignment” of the experimental peaks to the respective gap curve, taking into account the smearing of the gap peak due to a non-ideal barrier. Also with that assumption, the experimental points follow remarkably well the prediction for the sum and the difference of the electrodes’ gap, therefore we can be confident in affirming that the peaks visible in the conductance curves are effectively related to the gap presence in the superconducting electrodes excitation. Moreover, in some cases two junctions were available for the same misorientation angle ( $\theta=70^\circ$  and  $90^\circ$ ) with perfectly consistent results.

We also detected some peaks that cannot be related to the sum and the difference of the gap. In Figure 6.13e these peaks are showed with grey points. They can be related quite well to the behaviour of the single electrodes gap, showed with red and green solid lines for electrode I and II respectively. In an ideal  $S-I(N)-S$  tunnel junction, only the sum and the difference of the gaps should be detected. The reason for the appearance of the single gaps in our case could be found in the barrier microstructure. Due to normal conducting impurities formation, for example, part of the GB channel could behave as a  $S-I-N$  junction, as sketched in Figure 6.14. In this case, the gap of the  $N$ -facing superconducting electrode should appear in the conductance curve.

The results showed in Figure 6.13 are, to our knowledge, the most comprehensive experiment of gap spectroscopy in HTS GB junctions. This experiment is complementary to the  $J_C$  versus  $\theta$  one described in Ref. [11] and in several parts of this work. All the tunnel junctions, with misorientation angles ranging from  $0$  to  $90^\circ$ , were realized on the same chip, so to ensure the uniformity of the results. This is a further evidence of the possibility to accurately select the transport direction in biepitaxial junctions not only with regards to Josephson properties but also with regards to quasi particles transport. It is also another strong evidence that the transport in biepitaxial structure depends mostly on the  $d$ -wave effects and only in a minimum part on microstructural particular features.

## 7. **Conclusions**

Thanks to their peculiar properties, HTS materials could be implemented to create quantum electronics devices with novel characteristics. In this thesis we highlighted how the symmetry of the HTS order parameter could give rise to effects for which there is no analogue in conventional superconductors based devices. Nevertheless, applications of HTS junctions, included those in the field of quantum electronics, have for a long time been severely limited by a number of different factors, mostly related to the quality of the devices and to the d-wave order parameter symmetry. This scenario somehow changed a few years ago, when macroscopic quantum tunnelling and energy level quantization were actually measured in biepitaxial grain boundary Josephson junctions. These pioneering experiments showed that a proper design allowed to approach transport regimes that seemed for a long time precluded to HTS devices. On one hand, this stimulated novel insights into basic issues of dissipation and coherence in superconducting systems. On the other, these experiments confirmed the need of a deeper understanding of the transport mechanisms in these junctions.

In this thesis we have reported on advances in biepitaxial junctions fabrication procedures. We realized junctions using different techniques, both for the thin films deposition stages and for the patterning ones. Good, even if not definitive, results were obtained extending the biepitaxial technology to different substrates, like the lanthanum alluminate, of interest for microwave applications; a further proof of the flexibility of the biepitaxial design. Many efforts were devoted to the optimization of the whole fabrication process in order to achieve a longer junctions' lifetime, reduce the deterioration of the junctions' properties with the cool-down cycles and improve junctions reproducibility. This was aimed to increase the junctions reliability, a pre-requisite for whatever electronic application. Great part of this work was also dedicated to the challenging purpose of realizing sub-micrometric biepitaxial junctions. The reduction of the junctions size, indeed, can be seen as a powerful tool to get a better understanding of fundamental mechanisms ruling the grain boundary transport and as a key step for high quality, controllable junctions. An example is the study of conductance fluctuations in a "biepitaxial" channel a which size is in the range of 100nm. The study highlighted also how, when reducing the size of the junctions, the decoherence effects due to the quasiparticles, that are one of the main obstacles to macroscopic coherent phenomena, can be greatly reduced. Hence, narrower junctions not only help in the understanding the basis physics, but could also be the answer to the worries connected to decoherence in HTS devices. We reported on the first attempt to realize biepitaxial sub-micrometric junctions carried out in collaboration with Chalmers University of Technology, using a carbon mask technique used there since a few years and suitably improved for the treatment of sensitive materials as YBCO. The results are extremely encouraging: from the transport characterization done up to now, a very clean junctions' structure can be inferred. We also emphasized how, thanks to the lower influence the disorder has on smaller junctions, fundamental effects are more likely to arise and to be pinpointed, even with relatively simple transport measurements.

Finally, we can say that advanced technologies, in particular that one related to nano-scale fabrication, are rapidly leading to high level of control of HTS devices structures. This will, in turn, lead to a better understanding of their properties, in a circle that will probably also open new paths for HTS devices application.

## 8. References

- 
- [1] G. Bednorz, K.A. Muller, *Z. Phys. B.* 64 189 (1986)
  - [2] T. A. Zaleski, T. K. Kopeć, *Physical Review B*, 74, 014504 (2006)
  - [3] J.R. Waldran, *Superconductivity of Metals and Cuprates*, Institute of Physics publishing
  - [4] J. G. Thompson, B. G. Hyde, R. L. Withers, J. S. Anderson, J. D. F. Gerald, J. Bitmead, M. S. Paterson, and A. M. Stewart, *Mater. Res. Bull.* 22, 1715 (1987).
  - [5] R. L. Kurtz, R. Stockbauer, T. E. Madey, D. Mueller, A. Shih, and L. Toth, *Physical Review B*, 36, 7976 (1988).
  - [6] J Bardeen, J.N. Cooper, J.R.Schrieffer; *Physical Review*, 108:1175 (1957)
  - [7] Ginzburg, V. L., and L. G. Landau, *Zh. Eksp. Teor. Fiz.* 20, 1064 (1950).
  - [8] Van Harlingen, D. J; *Reviews of Modern Physics* 67, 515 (1995).
  - [9] Gor'kov, L. P. *Zh. Eksp. Teor. Fiz.* 36, 1918 (1959)
  - [10] Tsuei C.C., Kirtley J.R., *Reviews of Modern Physics*, 72, 969 (2000)
  - [11] F. Lombardi F. Tafuri, F. Ricci, F. Miletto Granozio, G. Testa, E. Sarnelli A. Barone, J. Kirtley and C. Tsuei *Physical Review Letters* 89, 207001 (2002)
  - [12] Kirtley J.R, Tsuei C.C., Ariando A, Verwijs C.J.M, Harkema S. and Hilgenkamp H, *Nature Physics* 2, 190 (2006)
  - [13] Josephson B.D, Possible new effects in superconductive tunneling, *Physics Letters*, 1, 251 (1962)
  - [14] Giaever I, *Physical Review Letters* 4, 464 (1960)
  - [15] Barone A, Paternò G; *Physics and Applications of Josephson Effect*, Wiley & Sons, New York (1982)
  - [16] K.K. Likharev, *Reviews of Modern Physics.* 51-1, 101 (1979)
  - [17] Golubov A A, Kupryanov M Yu and Il'ichev E *Reviews of Modern Physics.* 76 411 (2004)
  - [18] Amin M.H.S., Omelyanchouk A.N., Zagoskin A.M., *Physical Review B* 63, 212502-1 (2001)
  - [19] Tafuri F, Kirtley J.R, *Reports on progress of Physics*, 68 2573 (2005)
  - [20] J. Clarke, A. N. Cleland, M. H. Devoret, D. Esteve, J. M. Martinis, *Science* 239, 992 (1988); J. R. Friedman, V. Patel, W. Chen, S. K. Tolpygo, J. E. Lukens, *Nature* 406, 43 (2000); A. J. Berkley et al., *Science* 300, 1548 (2003); Y. Nakamura, Y. A. Pashkin, J. S. Tsai, *Nature* 398, 786 (1999); D. Vion et al., *Science* 296, 886 (2002); J. M. Martinis, S. Nam, J. Aumentado, C. Urbina, *Physical Review Letters* 89, 117901 (2002); I. Chiorescu, Y. Nakamura, C. J. P. M. Harmans, J. E. Mooij, *Science* 299, 1869 (2003).
  - [21] J. E. Mooij et al., *Science* 285, 1036 (1999).
  - [22] L. B. Ioffe et al., *Nature (London)* 398, 679 (1999); C. C. Tsuei and J. R. Kirtley, *Physica (Amsterdam)* 367C, 1 (2002).
  - [23] Flewitt P.E and Wild R.K, *Grain Boundaries – Their Microstructure and Chemistry*. Wiley, 2001
  - [24] Hilgenkamp H., Mannhart J., *Reviews of Modern Physics* 74, 485 (2002)
  - [25] T. Lindstrom, S. A. Charlebois, A. Ya. Tzalenchuk, Z. Ivanov, M. H. S. Amin, and A.M. Zagoskin, *Physical Review Letters*, 90, 117002 (2003)
  - [26] Char K., Colclough M. S., Garrison S. M., Newman N. and Zaharchuk G. *Applied Physics Letters* 59 733 (1991)
  - [27] Tafuri F., Miletto Granozio F., Carillo F., Di Chiara A., Verbist K. and Van Tendeloo G. *Physical Review. B* 59 11523 (1999)
  - [28] Lombardi F., Tafuri F., Ricci F., Miletto Granozio F., Barone A., Testa G., Sarnelli E., Kirtley J. R. and Tsuei C. C. *Physical Review Letters*, 89 207001 (2002)

- 
- [29] Miletto Granozio F., Scotti di Uccio U., Lombardi F., Ricci F., Bevilacqua F., Ausanio G., Carillo F. and Tafuri F. *Physical Review B* 67 184506 (2003)
  - [30] Bauch T., Lombardi F., Tafuri F., Barone A., Rotoli G., Delsing P and Claeson T 2005 *Physical Review Letters*, 94 87003
  - [31] T. Bauch, T. Lindström, F. Tafuri, G. Rotoli, P. Delsing, T. Claeson, F. Lombardi, *Science* 311 (2006) 57.
  - [32] Smilde H J H, Ariando, Blank D H A, Gerritsma G J, Hilgenkamp H and Rogalla H; *Physical Review Letters*, 88 057004, (2002)
  - [33] Moeckly, B. H., D. K. Lathrop, and R. A. Buhrman, *Physical Review B* 47, 400 (1993)
  - [34] Gross, R., P. Chaudhari, M. Kawasaki, and A. Gupta, *IEEE Trans. Magn.* 27, 3227 (1991); Gross, R., and B. Mayer, *Physica C* 180, 235 (1991).
  - [35] Halbritter, J., *Physical Review B* 46, 14 861 (1992).
  - [36] Sigrist, M., and T. M. Rice, *Journal of Physical Society of Japan*, 61, 4283 (1992)
  - [37] Bardeen J. *Phys. Rev. Lett.* 6 57 (1961)
  - [38] Kashiwaya S. and Tanaka Y. *Reports on Progress in Physics* 63 1641 (2000)
  - [39] Kirtley J R, Moler K A and Scalapino D J; *Physical Review B* 56 886 (1997)
  - [40] Hilgenkamp H, Ariando, Smilde H.J.H, Blank D.H.A, Rijnders G., Rogalla H, Kirtley J.R. and Tsuei C.C; *Nature* 422, 50 (2003)
  - [41] Hilgenkamp, H., J. Mannhart, and B. Mayer, *Physical Review B* 53, 14 586 (1996).
  - [42] Mannhart, J., Hilgenkamp H., Mayer B., Gerber Ch., Kirtley J. R., Moler K. A., and Sigrist M., *Physical Review. Letters* 77, 2782 (1996).
  - [43] Tafuri F., Kirtley J. R., Lombardi F. and Miletto Granozio F., *Physical Review B* 67 174516 (2003)
  - [44] Smilde H. J. H., Ariando, Blank D. H. A., Gerritsma G. J., Hilgenkamp H., and Rogalla H., *Physical Review. Letters* 88, 57004-1 (1996).
  - [45] Il'ichev, E., V. Zakosarenko, R.P.J. IJsselsteijn, H.E. Hoenig, H.-G. Meyer, M.V. Fistul, and P. Muller, *Physical Review B* 59, 11 502 (1999); Il'ichev, E., V. Zakosarenko, R. P. J. IJsselsteijn, V. Schultze, H.-G. Meyer, H. E. Hoenig, V. N. Glyantsev, and A. Golubov, *Applied Physics Letters* 72, 731 (1998); Il'ichev, E., V. Zakosarenko, R. P. J. IJsselsteijn, V. Schultze, H.-G. Meyer, H. E. Hoenig, H. Hilgenkamp, and J. Mannhart, *Physical Review. Letters* 81, 894 (1998)
  - [46] A. Ya. Tzalenchuk, T. Lindstrom, S. A. Charlebois, E. A. Stepantsov, Z. Ivanov, A. M. Zagoskin, *Physical Review B* 68, 100501 (2003)
  - [47] T. Bauch, F. Lombardi, F. Tafuri, A. Barone, G. Rotoli, P. Delsing, and T. Claeson. *Physical Review Letters*, 94, 87003 (2005)
  - [48] Bauch T., Lindstrom T., Tafuri F., Rotoli G., Delsing P., Claeson T., Lombardi F, *Science*, 311, 56 (2003)
  - [49] Ioffe L B, Geshkenbein V B, Feigel'man M V, Fauchere A L and Blatter G *Nature* 398 679 (1999)
  - [50] Blatter G, Geshkenbein V B and Ioffe L B *Physical Review B* 63 174511 (2001)
  - [51] Blais A and Zagoskin A M *Physical Review A* 61 42308 (2000)
  - [52] Makhlin Y, Schon G and Shnirman A *Reviews of Modern Physics* 73 357 (2001)
  - [53] Tsuei C C and Kirtley J R *Physica C* 367 1 (2002)
  - [54] AminMHS, Smirnov A Yu, Zagoskin AM, Lindström T, Charlebois S, Claeson T and Tzalenchuk A Ya; *Physical Review B* 71 064516 (2005)
  - [55] T. Orllepp, Ariando, O. Mielke, C. J. M. Verwijs, K. F. K. Foo, H. Rogalla, F. H. Uhlmann, H. Hilgenkamp, *Science* 312, 1495 (2007)
  - [56] G. Rotoli, T. Bauch, T. Lindstrom, D. Stornaiuolo, F. Tafuri, and F. Lombardi, *Physical Review B* 75, 144501 (2007)
  - [57] D. Stornaiuolo, D. Born, D. Dalena, E. Gambale, G. Rotoli, T. Bauch, A. Tagliacozzo, A.

- 
- Barone, F. Lombardi and F. Tafuri, *IEEE Transactions on Applied Superconductivity*, 17, issue 2 part 1 (2007), 225
- [58] R.W.Simon, C.E.Platt, A.E.Lee,K.P.Daly, M.S.Wire, J.A.Luine, M.Urbaniak, *Applied Physics Letters* 53 (1988) 2677
- [59] Brundle C.R., Evans C.A., Wilson S., *Encyclopaedia of Materials Characterization*, Butterworth-Heinemann Manning publications, 1992
- [60] Ohring M, *The Materials Science of Thin Films*, Academic press, 1992
- [61] F. C. Frank and J. H. van der Menve, *Proceedings of the Royal Society A* 189, 205 (1949).
- [62] G. B. Stringfellow, *Reports on Progress of Physics* 45, 469 (1982).
- [63] U. Scotti di Uccio, F. Miletto Granozio, A. Di Chiara, F. Tafuri, O.I. Lebedev, K. Verbist, G. van Tendeloo, *Physica C* 321, 162 (1999)
- [64] F. Miletto Granozio, U. Scotti di Uccio, F. Lombardi, F. Ricci, F. Bevilacqua, G. Ausanio, F. Carillo, and F. Tafuri, *Physical Review B* 67, 184506 (2003)
- [65] Poelders R., Auer R., Linker G., Smithey R., Schneider R., *Physica C* 247, 309 (1995)
- [66] U. Scotti di Uccio, Lombardi F., F. Miletto Granozio, *Physica C* 323, 51 (1999)
- [67] Tafuri F., F. Miletto Granozio, F. Carillo, A. Di Chiara, K. Verbist G. Van Tendeloo, *Physical Review B*, 59, 11523 (1999)
- [68] Dekkers J.M., Rijnders G., Harkema S., Smilde H.J.H., Hilgenkamp H., Rogalla H., Blank D.H.A., *Applied Physics Letters*, 83, 5199 (2003)
- [69] Xi X.X., Geerk J., Linker G.Q., Li Q., Meyer O., *Applied Physics Letters*, 54 2367 (1989)
- [70] P.R. Willmott, J.R.Huber, *Reviews of Modern Physics*, 72, 315 (2000)
- [71] G. Balestrino, S. Lavanga, P. G. Medaglia, S. Martellucci, A. Paoletti, G. Pasquini, G. Petrocelli, A. Tebano, A. A. Varlamov, L. Maritato, and M. Salvato, *Physical Review B* 62, 9835 (2000);
- [72] Krupke R., Barkay Z., Deutscher G., *Physica C* 289, 146 (1997)
- [73] Krupke R., Barkay Z., Deutscher G., *Physica C* 317, 536 (1999)
- [74] J. C. Nieu, H. Yamasaki, Y. Nakagawa, K. Develos-Bagarinao, M. Murugesan, H. Obara, and Y. Mawatari; *Applied Physics Letters* 86, 192507 (2005)
- [75] M. G. Norton, B. H. Moeckly, C. B. Carter, and R. A. Burhman, *Crystal. Growth* 114, 258, (1991)
- [76] S.A. Campbell, *The Science and Engineering of Microelectronic Fabrication*, Oxford University press (2001)
- [77] Petterson H. *Functional Structures of Interfaces in Biepitaxial YBCO thin Films*, Licentiate Thesis, Chalmers University of Technology, Sweden (2007)
- [78] P. Larsson, B. Nilsson, and Z. G. Ivanov, *Journal of Vacuum Science and Technology*, 18, 25 (2000)
- [79] *Handbook of Microlithography Micromachining and Microfabrication*, ed. P. Rai-Choudhury, SPEI press
- [80] F. Herbstritt, T. Kemen, L. Alff, A. Marx, and R. Gross, *Applied Physics Letters* 78, 955 (2001)
- [81] Zorin, A.B., *Review of Scientific Instruments*, 66, 4296 (1995)
- [82] D. Vion, P. F. Otfila, P. Joyez, D. Esteve, and M. H. Devoret, *Journal of Applied Physics*, 77, 2519 (1995)
- [83] Martinis J., Devoret M.H., Clarke J, *Physical Review B*, 35, 4682 (1987)
- [84] K. Bladh, D. Gunnarsson, E. Hurfeld, S. Devi, C. Kristoffersson, B. Smalander, S. Pehrson, T. Claeson, and P. Delsing, *Review of Scientific Instruments*, 74, 1323 (2003)
- [85] A. Fukushima, A. Sato, A. Iwasa, Y. Nakamura, T. Komatsuzaki, Y. Sakamoto, *IEEE Trans. Instrum. Meas.* 46, 289 (1997)
- [86] F. P. Milliken, J. R Rozen, G. A. Keefe, and R. H. Koch, *Review of Scientific Instruments*,

- 
- 78, 24701 (2007)
- [87] Delin K A and Kleinsasser A W, *Superconductors Science and Technology*, 9 227 (1996)
  - [88] Koren G., Polturak E., *Superconductors Science and Technology*, 15, 1335 (2002)
  - [89] Lee S.Y., Suh J.H., Kwon O.K., Cho J.Y., Park B.H., Lee J.H., Komashko V.A., Kim Y.H., Hahn T.S., Oh B., Kim H.T., Lee H., *Applied Superconductivity*, 6, 809 (1999)
  - [90] F. Tafuri, F. Carillo, F. Lombardi, F. Miletto Granozio, F. Ricci, U. Scotti di Uccio, A. Barone, G. Testa, E. Sarnelli, J. R. Kirtley, *Physical Review B*, 62, 14431 (2000)
  - [91] F. Tafuri, B. Nadgorny, S. Shokhor, M. Gurvitch, F. Lombardi, F. Carillo, A. Di Chiara, E. Sarnelli, *Physical Review B*, 72, 14076 (1998)
  - [92] For a review see *Mesoscopic Phenomena in Solids*, edited by B. L. Altshuler, P. A. Lee, and R. A. Webb, North-Holland, New York, 1991.
  - [93] R. A. Webb and S. Washburn, *Physics Today* 41, 46 (1988)
  - [94] S. Washburn and R. A. Webb, *Reports on Progress in Physics* 55, 1692 (1992)
  - [95] B. L. Altshuler, Pis'ma Zh. Eksp. Teor. Fiz. 41, 530 (1985), *JETP Letters*, 41, 648 (1985)
  - [96] P. A. Lee and A. D. Stone, *Physical Review Letters* 55, 1622 (1985)
  - [97] D. J. Thouless, *Physics Reports*, 13, 3 (1974)
  - [98] A. van Oudenaarden, M. H. Devoret, E. H. Visscher, Yu. V. Nazarov, and J. E. Mooij, *Physical Review Letters* 78, 3539 (1997)
  - [99] Takayanagi, J. Bindslev Hansen, and J. Nitta, *Physical Review Letters* 74, 166 (1995); J. P. Heida, B. J. van Wees, T. M. Klapwijk, and G. Borghs, *Physical Review B* 60, R13135 (1999); P. Dubos, H. Courtois, B. Pannetier, F. K. Wilhelm, A. D. Zaikin, and G. Schön, *Physical Review B* 63, 064502 (2001)
  - [100] A. Tagliacozzo, D. Born, D. Stornaiuolo, E. Gambale, D. Dalena, F. Lombardi, A. Barone, B. L. Altshuler, and F. Tafuri, *Physical Review B*, 75, 12507 (2007)
  - [101] Hersbitt F., Kemen T., Marx A., Gross R., *Journal of Applied Physics*, 91, 5411 (2002)
  - [102] H. Eisner, R. IJsselsteijn, W. Morgenroth, H. Roth and H.-G. Meyer, *Microelectronic Engineering* 41/42, 407 (1998)
  - [103] P. V. Komissinski, B. Hogberg, A. Ya. Tzalenchuk, Z. Ivanov, *Applied Physics Letters*, 88, 1022 (2002)
  - [104] G. Rotoli et al. manuscript
  - [105] J. R. Kirtley and F. Tafuri, Tunnelling Measurements of the Cuprate Superconductors in "Treatise of Superconductivity" edited by Robert Schrieffer, pages 19-85 (Springer Verlag, 2007)
  - [106] G. E. Blonder, M. Tinkham, and T. M. Klapwijk, *Physical Review B* 25, 4515 (1982).
  - [107] J. Y. T. Wei, N. C. Yeh, D. F. Garrigus, and M. Strasik, *Physical Review Letters* 81, 2542 (1998).
  - [108] I. Iguchi, W. Wang, M. Yamazaki, Y. Tanaka, and S. Kashiwaya, *Physical Review B* 62, 6131 (2000)
  - [109] T. Miyake, T. Imaizumi, and I. Iguchi, *Physical Review B*, 68, 214520 (2003)
  - [110] Yizi Xu and J. W. Ekin, *Physical Review B*, 69, 104515 (2004)